HALL ACCELERATION IN A PARTIALLY IONIZED PLASMA

PETER JAMES LOMAS

Imperial College

This thesis is submitted in partial fulfilment of the requirements of the Degree of Doctor of Philosophy in the University of London

October, 1975

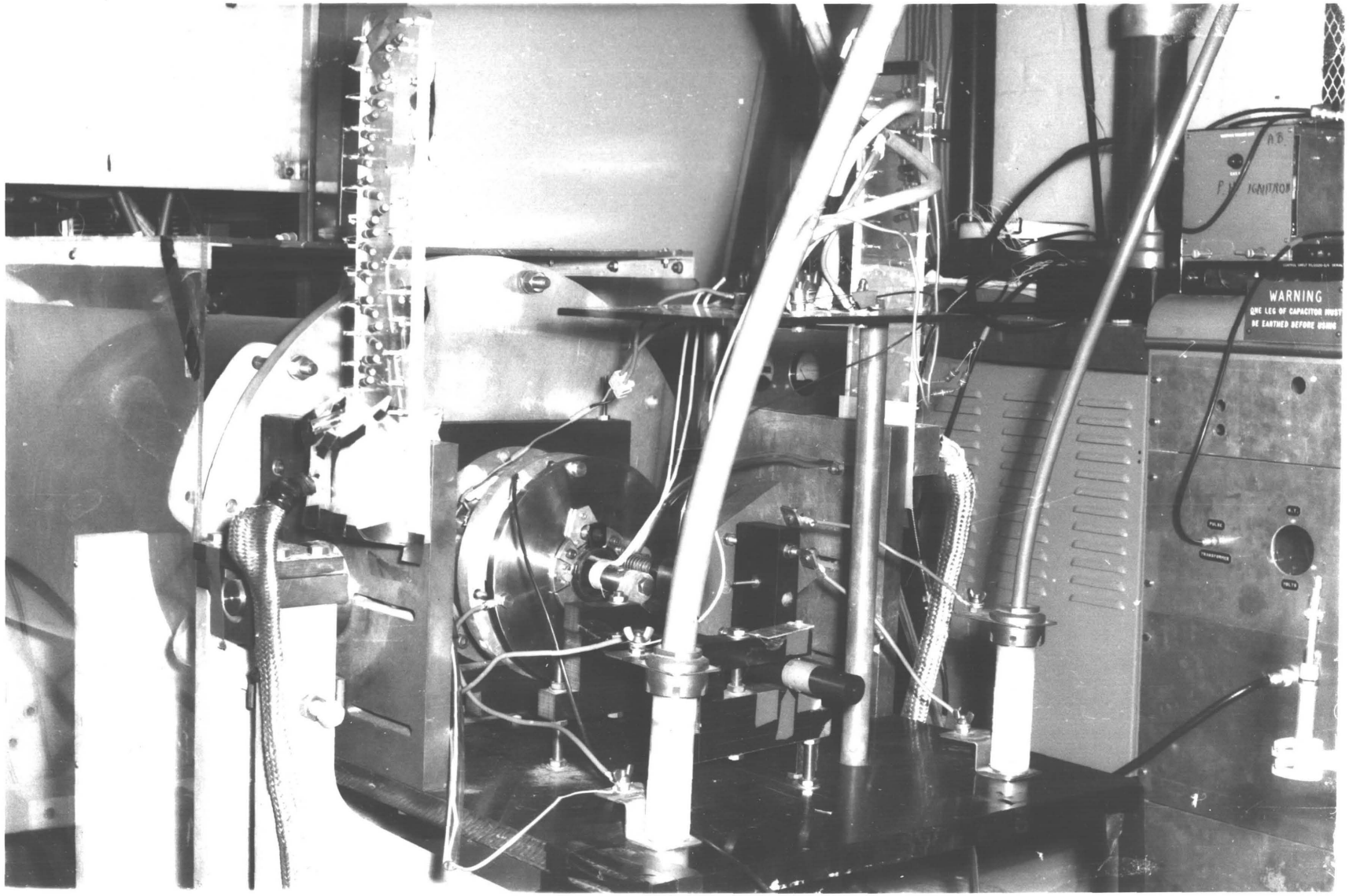

FRONTISPIECE The two stage accelerator in position on the vacuum system.

ACKNOWLEDGEMENTS

It is a pleasure to acknowledge the assistance from many quarters without which this work would not have been possible.

In particular I would like to take this opportunity of thanking Dr H.C. Cole of the Culham Laboratory, for making available experimental facilities and for much encouragement and useful comment. I would also like to thank Mr M.J. Terry, Mr A. Johnson and Mr G.O.R. Naylor for assistance in maintaining the rig during this time.

I am very much indebted to Dr J.D. Kilkenny of Imperial College, who maintained an interest in this work from its earliest stages and who continually supplied constructive criticism. Thanks must also go to Professor M.G. Haines who acted as supervisor.

I thank the S.R.C. for provision of a Studentship and the UKAEA who helped with travelling expenses.

I must also mention the many people from the Imperial College Plasma Group and others who made the catastrophes bearable.

Last, but by no means least, I thank Ina Godwin for carefully typing this manuscript.

Thank you !

C O N T E N T S

C O N T E N T S
(continued)

C O N T E N T S

(continued)

CONTENTS

(continued)

ABSTRACT

Heating and possible thermonuclear ignition of a magnetically confined plasma by means of fast neutral injection is of great current interest. Potentially the Hall accelerator is very attractive for the provision of the energetic beams envisaged, since there is, in principle, no limit to the scale up of existing accelerators. Unfortunately the performance has been disappointing in practice for reasons heretofore obscured by a lack of definitive plasma measurements.

The aim of the experimental work presented in this thesis has been to correct this lack. The measurements show that, though the Hall parameter $\omega\tau$ is large, acceleration is inefficient, particularly in the first stage of the two stage device, and the electron conductivity is greater than the collisional value. The behaviour is shown to be dominated by a fast instability (frequency ~ 5 mc/s), and a slow spoke-like instability (frequency ~ 100 kc/s). Momentum and energy balance are considered.

Because of the significance of the instabilities, these have been studied using the linear theory, and the spoke identified as the electrothermal ionization wave. The limitations of this approach have been overcome by setting up two dimensional time dependent fluid equations, which are solved numerically. The growth of spokes and their effect on plasma acceleration is thus investigated. Trajectory calculations can account for some features such as the large beam divergence, and predicts severe wall losses.

Some proposals are made, by means of which the potential of the Hall accelerator might be more fully realised.

CHAPTER I

INTRODUCTION

1.1 PERSPECTIVE

The performance of magnetic containment systems has improved over the last decade so that high densities, $n_e \sim 1\text{-}5\ 10^{19}\ m^{-3}$, can be confined for long energy replacement times, $\tau_E \sim 5\text{-}20$ ms in the Tokamak configuration (Artsimovich, 1969; Dimock, 1973; TFR Group, 1975). These results are sufficiently encouraging that several large Tokamak devices have been proposed (Kusnetsov, 1975 Review). The criterion $n_e \tau \geqslant 10^{20}\ m^{-3} s$ (Lawson, 1957) required for thermonuclear break-even should be approached in these experiments.

However, it seems unlikely that ignition temperatures will be achieved by Ohmic heating alone, and that heating by the injection of fast neutrals may have a significant role to play (Furth, 1975). Injection is attractive because it is readily controllable, and quiescent, because it can be made to heat ions preferentially and can be fairly efficient (Stix, 1972). Such a system may be envisaged conceptually on the black box level of Fig.1.1. The confinement system, upon which much attention has

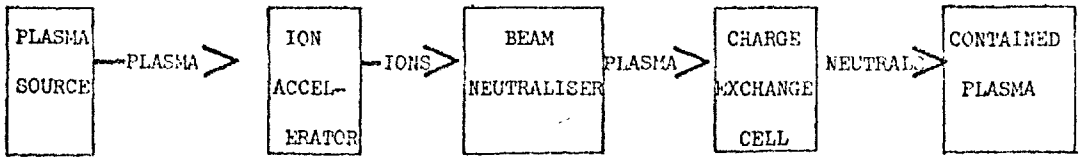

Fig.1.1
A schematic neutral beam injection system

so far been concentrated, may be Tokamak, Stellarator or magnetic mirror, but will not be considered further here. The plasma source provides a copious supply of hydrogen or deuterium plasma to the accelerator which accelerates only ions. The charge on these ions must be neutralised so

that they will propagate into the gas cell. Here charge exchange with a neutral gas produces fast neutrals and slow ions. If these neutrals undergo no ionizing collisions, they will cross the confining fields and enter the hot plasma. The hot electron background ionizes these neutrals, so that they then perform characteristic orbits in the magnetic fields. Those ions on contained orbits surrender their energy to the plasma ions and electrons by Coulomb collisions.

The ionization and thermalization of the fast particles has been treated theoretically (Stix, 1972), and recently injection experiments have demonstrated the feasibility, albeit on a low power input level, of heating a Tokamak plasma by this method (Aldcroft, 1973; Cordey, 1975). The higher injected powers on the new generation of Tokamaks (e.g. PLT and DITE) should give some indication of how far the technique may be extended, and whether large injected powers produce undesirable side effects.

The physics of the charge exchange cell is well known and the extension to deal with thermonuclear power levels has already received attention (Sweetman, 1971).

The conventional approach to the production of the energetic plasma beam has utilised ion acceleration by a space charge diode fed with ions from a duopigatron arc source and neutralised by an electron emitting filament (Stix, 1962; Aldcroft, 1973). A Hall plasma accelerator could replace all three components since it is self ionizing and needs no neutralisation.

A brief discussion of the space charge accelerator is now presented so that the relative merit of it and the Hall accelerator can be compared. The acceleration of ions is identical to electrons in a plane electrode vacuum-tube diode, provided electric fields perpendicular to the current flow are negligible. Then the behaviour follows the classic Child-

Langmuir law for the current:

$$I = \frac{4}{9} \cdot \epsilon \cdot \left(\frac{2Ze}{M}\right)^{\frac{1}{2}} \frac{V^{\frac{3}{2}}A}{d^2} \quad \text{AMP} \qquad \ldots (1.1)$$

where V is the electrode voltage, A is the electrode area, d the electrode separation, M the ion mass and Z the ion charge. Hence for a squat device where $d^2 \sim A$, the current is only 160 mA of H^+ ions for $V = 20$ kV. This limits the power to ~ 3 kW per beam.

This limit is circumvented conventionally either by use of multi-apertures or by sheet beams. However, technical limitations, such as aperture alignment, electrode damage and non-uniform plasma source illumination have limited existing devices to ~ few 10 s amp at 20 kV, i.e. ~ few 100 kW beams. Because of the inherent inefficiencies of the injection process (Stix, 1972; Aldcroft, 1973) some considerable effort will be required in order to achieve the multi-megawatt useful injected power required for the large proposed machines such as JET or TFTR. In addition, the increased neutral energies ~ 1 MeV required for injection into a possible reactor plasma (Sweetman, 1971) will impose additional problems such as the insulation of narrow electrode gaps. For these reasons, it is desirable to examine alternative accelerators.

1.2 SIMPLE HALL ACCELERATOR THEORY

For clarity and easy reference, the simple picture of Hall acceleration put forward by Haines and Kilkenny (Haines, 1961; Kilkenny, 1973) is briefly discussed here. Treatments due to the early space propulsion workers (Hess, 1963) are less physically elegant.

The essential configuration is illustrated in Fig.1.2. An electric field E_z is imposed perpendicular to an applied magnetic field B in the X direction, by means of electrodes at $Z = 0$ and $Z = L$ and of infinite extent in the Y direction. The generalised Ohm law can be

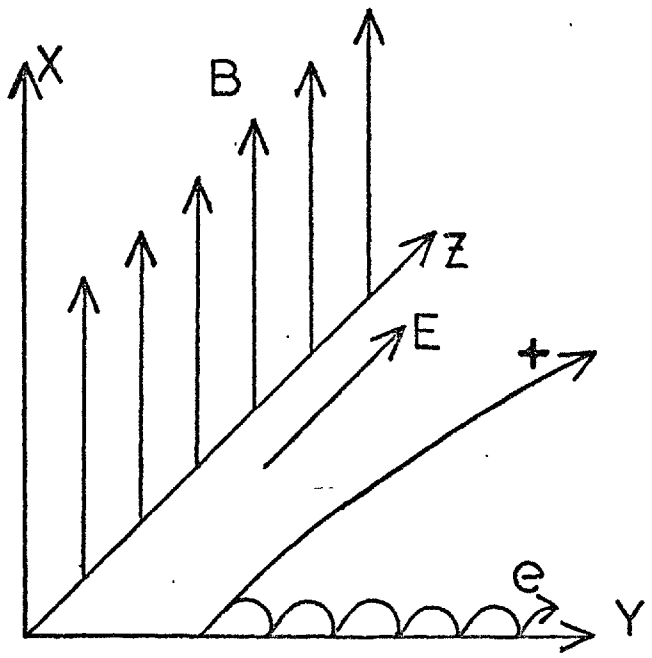

Fig.1.2
The E and B fields for a Hall accelerator

written :

$$\frac{\underline{J}}{\sigma} = \underline{E} + \underline{v} \wedge \underline{B} + \frac{\nabla p}{ne} - \frac{\underline{J} \wedge \underline{B}}{ne} \qquad \ldots (1.2)$$

and applied to the currents in the Y-Z plane. E_y is taken as zero, so that the neglect of ∇p and v_y terms give :

$$\left.\begin{aligned} J_z &= \frac{\sigma}{1+\beta^2}\left(E_z + \beta v_z B\right) \\ J_y &= \frac{\sigma}{1+\beta^2}\left(v_z B - \beta E_z\right) \end{aligned}\right\} \qquad \ldots (1.3)$$

where the dimensionless quantity $\beta = \omega\tau$ is the product of electron gyro-frequency and electron collision time, and is called the Hall parameter. If β is large, i.e. the electrons are collisionless, the two equations simplify to :

$$J_z = \frac{\sigma E_z}{1+\beta^2} + nev_z \quad ; \quad J_y = -\frac{neE_z}{B} . \qquad \ldots (1.4)$$

The first term in the equation for j_z represents the electron conduction current across the field parallel to E_z and the second the ion current. The y-current arises from the transverse E/B drift of electrons and constitutes the Hall current. The interaction of this current with B

produces a force on the plasma according to the equation of motion:

$$M \frac{D}{dt} nv_z = -J_y B = neE_z \ . \qquad \ldots (1.5)$$

Physically this means the plasma ions are freely accelerated by the electric field to give rise to an ion current which contributes to the z-current according to equation (1.4). If β is large, the proportion of electron current to ion current should be small, and the accelerator should therefore be efficient.

This equivalence of fluid and ion orbit model leads to a physical reason for the neglect of v_y: that the ion Larmor radius should be larger than the apparatus length, L, to prevent y motion, i.e.

$$\rho_{Li} \gg L \ . \qquad \ldots (1.6)$$

In order to prevent the fields generated by the Hall current from destroying the applied B field, the condition:

$$\frac{\mu_o ne E_z L}{B^2} \leqslant 1 \qquad \ldots (1.7)$$

must be observed.

Streaming instabilities are likely unless the electron and ion stream velocities are less than the electron thermal velocity, so the following conditions must be met:

$$\frac{E_z}{B} \leqslant \left(\frac{2kT_e}{m_e}\right)^{\frac{1}{2}} \qquad \ldots (1.8)$$

and

$$\frac{eV}{kT_e} \leqslant \frac{M_i}{m_e} \qquad \ldots (1.9)$$

where V is the discharge voltage.

One should note here that there is no ion current versus voltage relation for the Hall accelerator corresponding to equation (1.1) for the space charge device. For the Hall accelerator an appropriate set of equations will include the plasma fluid equations and so the resulting solution for the current in terms of the potential will not in general

give a simple algebraic relationship. However, qualitatively, for a given current, the number of stages may be selected to give the required ion energy. Thus it should be possible to accelerate large currents of ions to any given ion energy.

1.3 THE BACKGROUND OF OTHER WORKERS

The work on Hall accelerated plasma began in the early 1960's, independently in the U.K. and U.S.A. though with widely differing objectives. In the U.S.A. the work was concentrated on plasma space propulsion (Hess, 1963; Lary, 1963; Burlock, 1965; Janes, 1966) and a typical device is illustrated in Fig.1.3(a). Such single stage devices were operated in the gas discharge mode at a few amps at low fields (50–200 Gauss) with low discharge voltages (100 V – 1 kV). In the U.K., at Imperial College, the acceleration effect was first observed in a Z-pinch with a single turn current loop around it. The upstream and downstream plasmas were observed to be different. This led to a detailed treatment of the Hall process as a mechanism for the acceleration of ions in a pinch, and to a proposal for linear and toroidal Polytrons (Haines, 1961) as illustrated in Fig.1.3(b). These devices were intended to improve containment in the picket fence geometry. The regime of operation is very different from the propulsion work (Dangor, 1969). A high density ($n_e \sim 5 \times 10^{20}$ m^{-3}) highly ionized argon plasma carries ~ 20 kA of current across fields ~ 0.3 T. The toroidal electric field is $\sim 10^4$ V/m, but gives ion energies of only a few 10 s eV, when the toroidal voltage drop is ~ 10 kV. There is serious ion loss in distances of the order of the stage length. The plasma loss and energy balance are well documented (Kilkenny, 1973) but the emphasis has been on containment.

The interest in Hall acceleration for injection purposes began with the construction of a two-stage device in the U.S.S.R. (Morozov, 1968) and

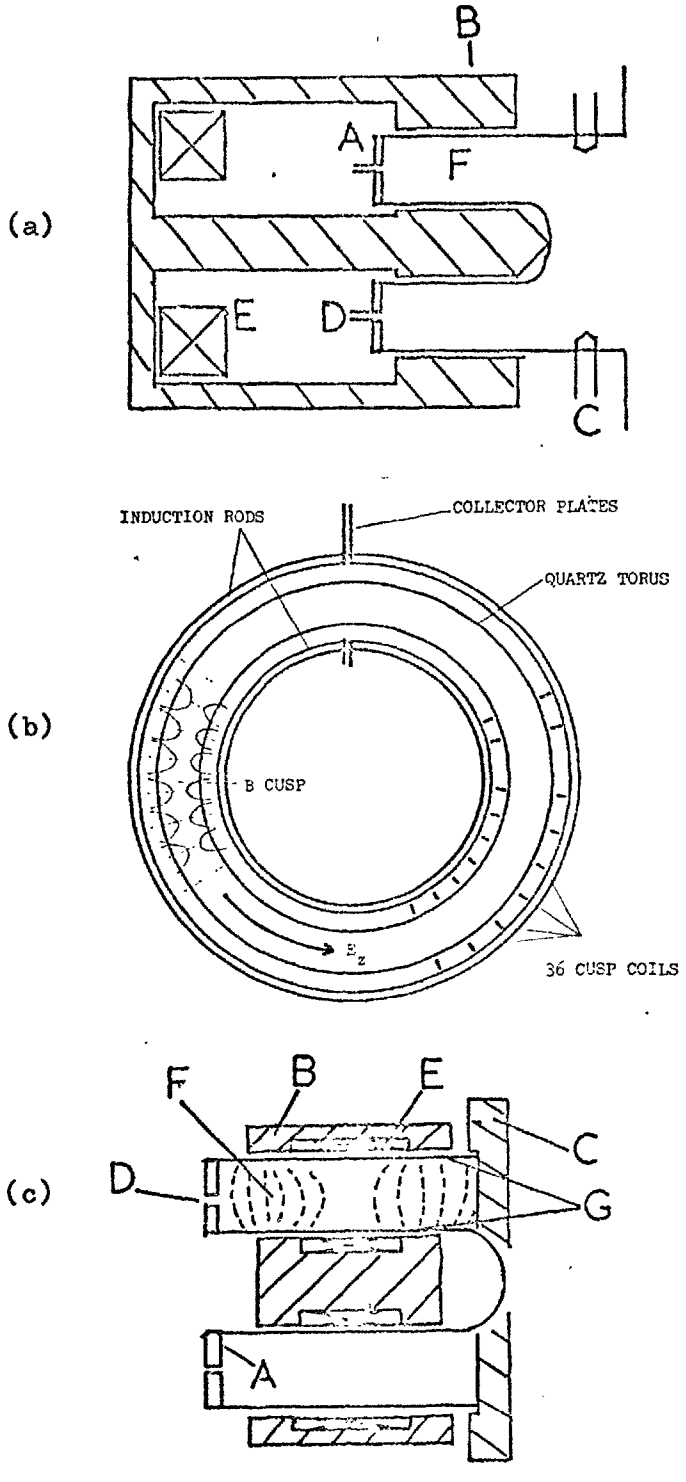

Fig.1.3

(a) Schematic of a single stage space propulsion accelerator showing: A anode, B magnet, C hot cathode, D gas inlet, E field coil and F the plasma region.

(b) The toroidal Hall accelerator - the Polytron.

(c) A two stage injection accelerator showing: A anode, B magnet, C cathode, D gas inlet, E field coils, F the radial field regions, and G the insulating walls.

a similar device at Culham (Cole, 1969). These used iron magnets for a gas breakdown discharge, like the space propulsion devices, but carrying much higher currents ~3kA. Fig.1.3(c) illustrates such a device.

Cole has considered the accelerator as part of a neutral beam system and has therefore aimed at achieving a well collimated beam of ~20 keV hydrogen ions with good efficiency (Cole, 1970; Sweetman, 1971). His designs have included conical devices, C.W. accelerators and multi-stage systems (Cole, 1972,1974). Unfortunately, little effort has been available for plasma diagnosis and measurement.

Morozov, Zubkov and co-workers have also employed several different designs (Zubkov, 1971,1972; Morozov, 1972) but their published work does not indicate what role these might play in injection.

A brief summary is now presented of the results obtained by these two groups. A Hall current has been shown to flow, and a beam of accelerated plasma is observed. Both energy flux distribution and particle energy spectra have been measured for typical exhaust plasmas. The exhaust is characterised by a large divergence, 30-40° half angle. The beam power/input power ratios are low. The voltage-current characteristic for several devices lie on the curve of negative slope illustrated in Fig.1.4. The reason for this is not well understood, but it effectively limits beam currents for the required 20 keV ion energies. The consequence of these three points, beam divergence, power efficiency and V-I characteristic is that Hall accelerators are not, at present, competitive with space charge accelerators (Sweetman, 1971).

Fluctuations and non-uniformities have been observed (Morozov, 1972b, 1973c; Cole, 1970) but no satisfactory explanation has been proposed.

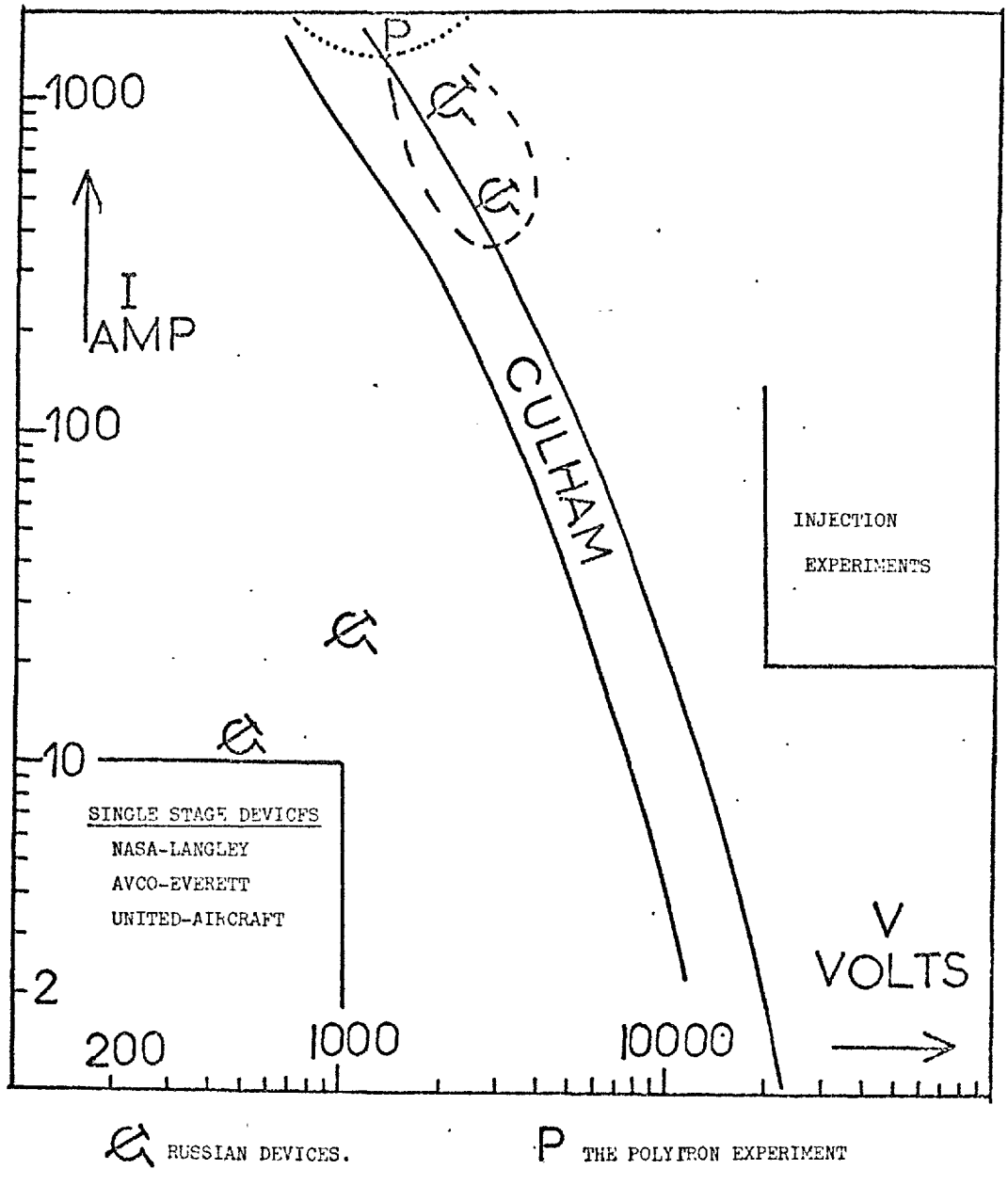

Fig.1.4
Volt-Ampere plot for various Hall accelerators

Until recently (Lomas, 1974; Abramov, 1974; Lomas, 1975) there were no direct measurements on the plasma density and temperature.

Little theoretical work has been published on these accelerators, so, in consequence, it is not clear whether the limitations are inherent in the Hall mechanism, or in the particular approach chosen.

1.4 THE NEW WORK TO BE PRESENTED

As is apparent from section 1.2, the dimensionless parameter $\omega\tau$ is crucial in determining the plasma behaviour. Hall acceleration is most efficient when $\omega\tau$ is large. In a linear Hall accelerator the transition from an electron current at the anode (where both v_z and ion current are small) to an ion current will be determined by $\omega\tau$. Hence it is necessary to measure experimentally n_e and T_e in order to evaluate this parameter. This is the principal object of the experimental programme.

In the light of these measurements, the calculation of ion trajectories allows qualitative judgements to be made concerning the divergence and efficiency problems.

Experimentally, instabilities are shown to dominate the electrical conductivity. Because of the importance of these fluctuations an attempt is made to account for them theoretically by an extension to linear electrothermal theory. The limitations of such an approach are overcome by a time dependent, two dimensional fluid model, which deals with the slow mode. By this means the experiment and theory can be compared in more detail.

Finally, an optimistic note is sounded. The limitations of the Hall accelerator appear to be a consequence of the low degree of ionization and the broad ionization region. Some suggestions are made as to which approaches might prove more rewarding.

CHAPTER II

PRELIMINARY EXPERIMENTS

2.1 PREAMBLE

It is possible to write down numerical expressions for the electron-ion and electron-neutral collision frequencies (Spitzer, 1955; Massey, 1951) in a hydrogen plasma:

$$\nu_{ei} = 4 \times 10^{-11} \times n_e / T_e^{\frac{3}{2}} \ s^{-1} \qquad \ldots (2.1)$$

$$\nu_{eN} = 2 \times 10^{-14} \times N \times T_e^{\frac{1}{2}} \ s^{-1} \qquad \ldots (2.2)$$

It is necessary to determine electron density n_e (m^{-3}), electron temperature T_e (eV), and the neutral density N (m^{-3}) in order to determine the total collision frequency and hence $\omega\tau$.

In the steady state, it is possible to write down a simple electron energy balance of the form:

$$\frac{J^2}{\sigma} = 3\,nkT\left(\nu_{en} + \nu_{ei}\right)\frac{m_e}{m_i} + nNSE_I e + 2.5\,\frac{nk^2T^2}{m_e \nu L^2} .$$

This neglects ion motion and assumes infinite ion thermal capacity. The terms represent Ohmic heating by an electron conduction current density J, energy loss due to collisions with heavy particles, the energy required to sustain ionization at rate $nNS\ m^{-3}s^{-1}$ (E_I is the ionization potential in eV), and the electron thermal conduction loss along the field to a wall at distance L (m). The ionization coefficient for hydrogen, $S = 1.4 \times 10^{-13}\ EXP(-13.6/T)/(T^{\frac{1}{2}})\ m^3 s^{-1}$, is taken from Hinnov (1962). Solutions to this polynomial in n_e and T_e are shown in Fig.2.1 for various current densities. Here N is taken $10^{21}\ m^{-3}$ and $L = 0.02$ m. For the operating range of Cole's accelerators, with currents 20 amp to 3 kA in $\sim 50\ cm^2$, the temperature will lie in the range 0.5 to 2.0 eV over a wide range of densities above $n_e \sim 10^{18} m^{-3}$.

A lower limit can be set on the cathode density from the ion current density J_{iz} assuming an ion energy equal to the voltage drop between

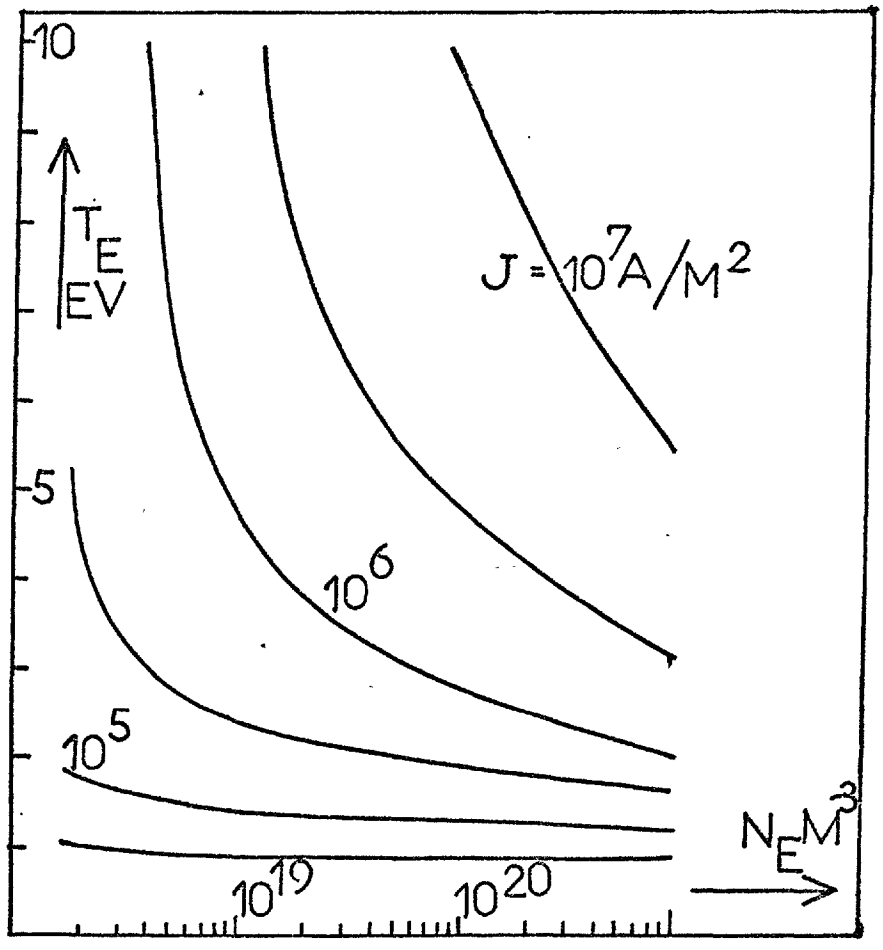

Fig.2.1

Curves for energy balance in $n_e - T_e$ space. The labels are current densities in amp/m^2. $N = 10^{21}\ m^{-3}$, $L = 0.02\,m$

the electrodes, V:

$$n_e = \frac{J_{iz}}{e} \times \left(\frac{M_i}{2eV}\right)^{\frac{1}{2}} \sim 2.0 \times 10^{16} \times I/V^{\frac{1}{2}}\ m^{-3} \qquad \ldots (2.4)$$

where I is the total discharge current, and it has been assumed that ~30% of this is carried by ions (Cole, 1970). This gives $n_e \sim 10^{17}\ m^{-3}$ for $I = 1\,kA$, $V = 1\,kV$. In practice, the density will lie between this value and a limit set by full ionization of the neutral gas filling pressure. For n_e between 10^{17} and $10^{21}\ m^{-3}$ and T_e between 0.5 and 2.0 eV at $B = 0.05\,T$, $\omega\tau$ will lie in the range $1-10^3$ for $N = 10^{21}\ m^{-3}$.

2.2 APPROPRIATE DIAGNOSTICS

Probe and spectroscopic diagnostics for plasmas in this density and temperature range are covered extensively in the literature (e.g. Griem, 1964; Lochte-Holtgreven, 1968), but some of the more important results are listed here.

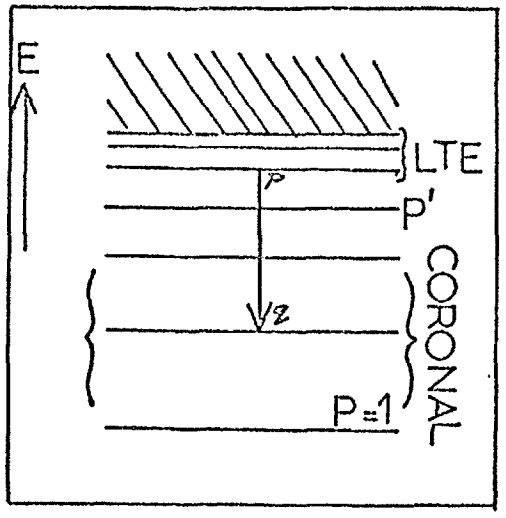

Fig.2.2
Schematic system of Maxwellian free electrons and bound atomic levels

For a hydrogenic state p, in LTE with Maxwellian free electrons (Fig.2.2), the state population is given by:

$$n(p) = n_e^2 p^2 \left(\frac{h^2}{2\pi m_e kT_e}\right)^{\frac{3}{2}} * \exp\left(\frac{E_H}{p^2 kT}\right) \quad \ldots (2.5)$$

where E_H is the ionization potential of the ground state. LTE, local thermodynamic equilibrium, is valid for the upper states of the Balmer transition in hydrogen if:

$$\begin{aligned} n_e &> 10^{20}\, T^{\frac{1}{2}}\ m^{-3} && \text{for } H_\alpha \\ n_e &> 10^{19}\, T^{\frac{1}{2}}\ m^{-3} && \text{for } H_\beta \\ n_e &> 1.5\times 10^{18}\, T^{\frac{1}{2}}\ m^{-3} && \text{for } H_\gamma \end{aligned} \quad \ldots (2.6)$$

This should be a useful density and temperature diagnostic at least for the shorter wavelength transitions. For high densities the Stark breadth of H_β, $\Delta\lambda_s$, will give the density from:

$$n_e = C(n_e, T_e) * (\Delta\lambda_s)^{\frac{3}{2}}\ m^{-3} \quad \ldots (2.7)$$

where $C(n_e, T_e)$ is only a weak function of n_e and T_e for densities of interest. H_α is negligibly Stark broadened compared to H_β, so the Doppler breadth of H_β may be found from the H_α line breadth since:

$$\Delta\lambda_D = \left(\frac{2kT_a\, \ell n\, 2}{M_a C^2}\right)^{\frac{1}{2}} \lambda_o \quad \ldots (2.8)$$

where T_a is the atom temperature, and λ_o the wavelength of the line.

The Langmuir probe, illustrated schematically in Fig.2.3 has voltage-current characteristic:

$$I = i_+ \tanh\left(\frac{eV}{2kT_e}\right) \quad ; \quad i_+ = CAn_e e \left(\frac{kT_e}{M_i}\right)^{\frac{1}{2}} \quad \ldots (2.9)$$

where CA is the effective probe area. This characteristic has a saturation current i_+ and is illustrated in Fig.2.4. The temperature can be obtained from the slope at $V = 0$:

$$\left(\frac{dI}{dV}\right)_{V=0} = \frac{e}{kT_e} \times \frac{i_+}{2}$$

and hence n_e can be obtained from i_+.

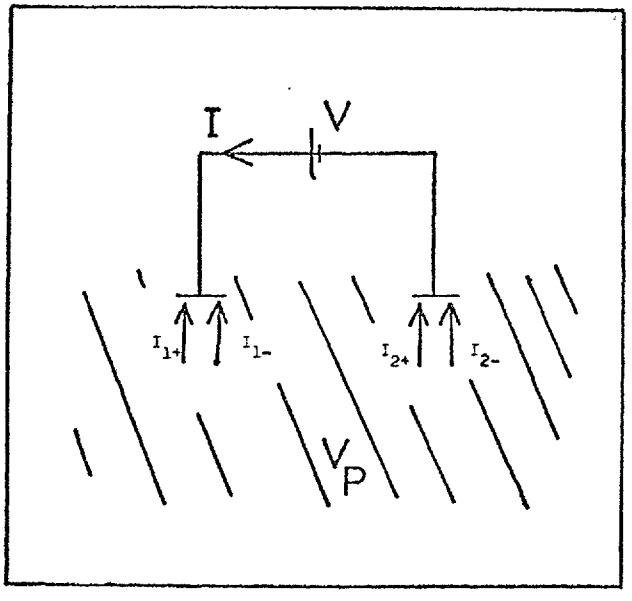

Fig.2.3
Schematic double Langmuir probe. V_p is the plasma potential, V is the bias voltage and i_+ and i_- the ion and electron currents to tips 1 and 2

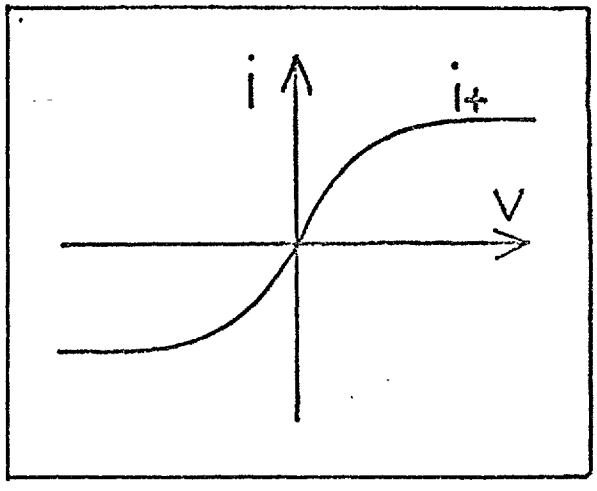

Fig.2.4
Probe V-I characteristic. i_+ is the saturation current

2.3 DESCRIPTION OF ACCELERATOR

Despite the fact, mentioned in Chapter I, that high voltage low current accelerators are of more immediate application to injection experiments, it was thought that a high current (~kA) device would be more straightforward to study experimentally. Relation (2.4) would suggest high densities, where LTE and Stark methods might be applicable. However, features such as the V-I plot of Fig.1.4 suggest the behaviour of Hall accelerators is similar in character over a wide range of operating conditions.

The 3 kA accelerator, vacuum system and capacitor bank at UKAEA/ Euratom Culham Laboratory, were placed at the disposal of the author (c.f. Acknowledgements). This accelerator is shown diagrammatically in Fig.2.5, and is almost identical to that described by Cole (1970). The discharge chamber has an annular cross-section, with transverse magnetic field provided by a soft iron electromagnet in such a way as to give two stages of radial field. The discharge current is supplied by a 200 kJ (880 μF at 20 kV) capacitor bank arranged as a 20 ms delay line. Usually, hydrogen gas is fed in by means of a fast capacitor-driven cone valve, and vacuum provided by 3 * 14 inch oil diffusion pumps. The layout of the rig is shown in Fig.2.6. Optical viewing ports were added through the outer magnet and its winding to give radial access to the plasma. Two Wilson seal type ports were added to the anode assembly to give axial probe and spectroscopic access. A port and adjustable probe holder on the cathode plate of the vacuum system allowed probe access through the cathode aperture. Improvements to reliability entailed the avoidance of internal supporting insulators for the magnet, and the introduction of a seal at the anode end of the plasma wall. The damaging long bank pulse tail was truncated by means of a diverting ignitron when it was realised that little of interest occurred here despite severe wall damage and anode melting.

Cole has already performed extensive work on this device, (Cole, 1970) but with the aim of assessing its suitability as an injector. Almost no plasma measurements have been performed on this device.

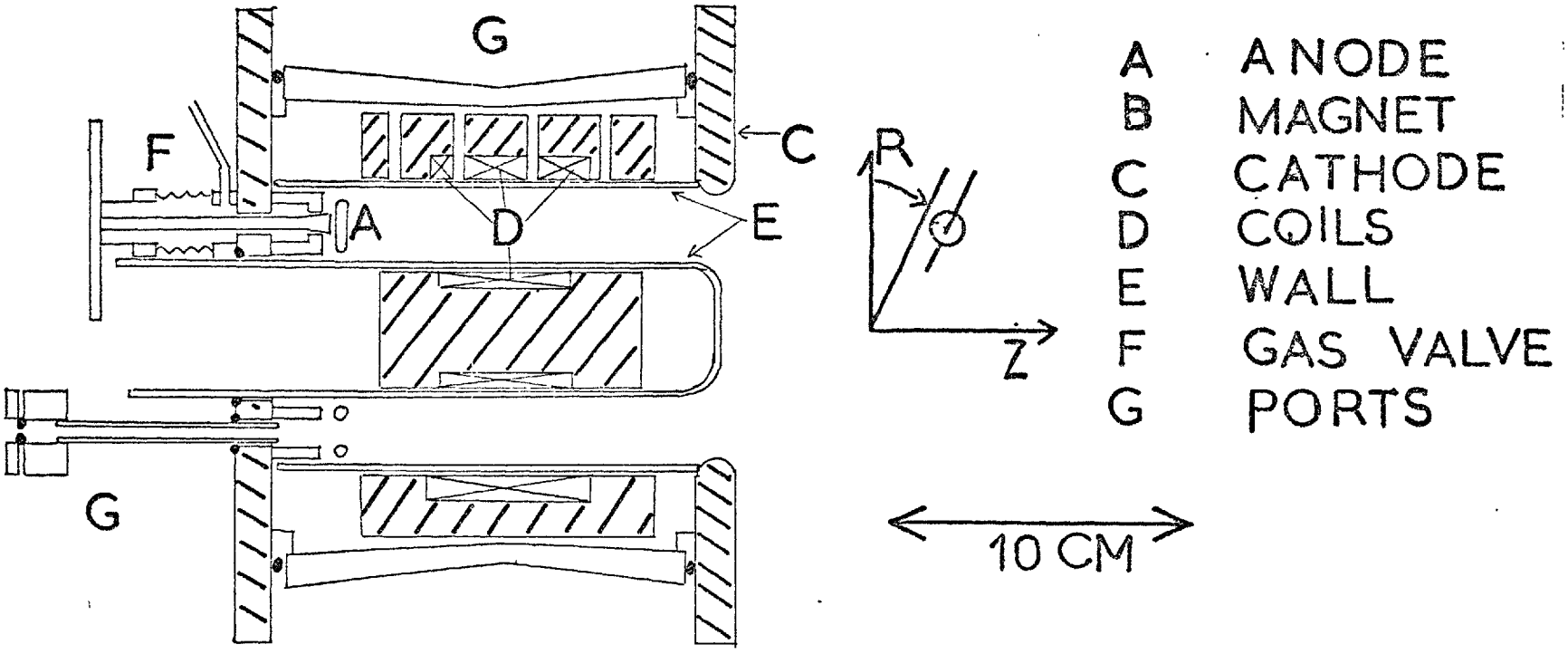

Fig.2.5 The two stage Hall accelerator

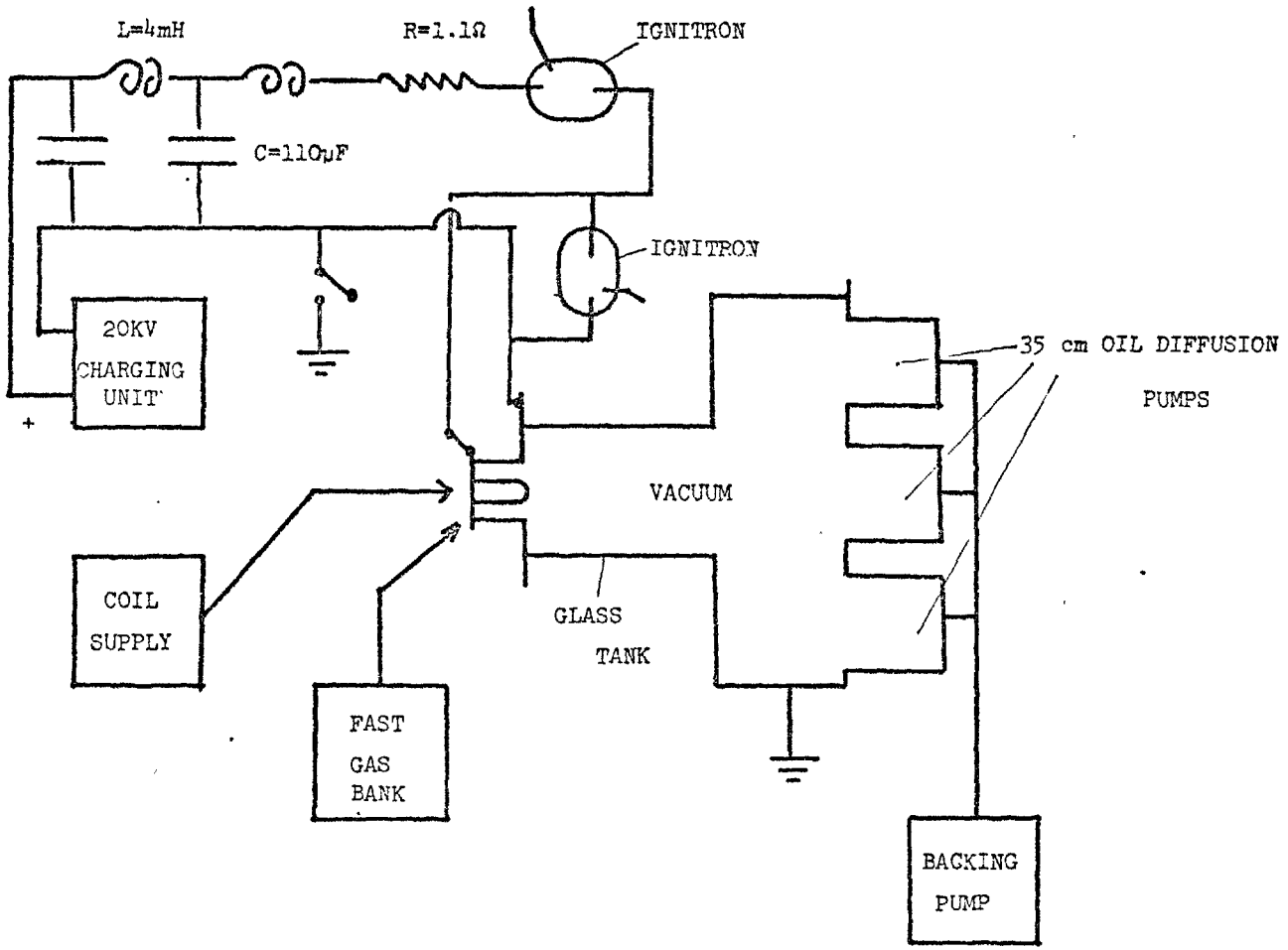

Fig.2.6 Culham accelerator rig

2.4 PRELIMINARY OBSERVATIONS

The first new measurement performed was the observation of the anode plasma using an H_β filter and photomultiplier, using one of the radial viewing ports. Fig.2.7 shows, for a typical discharge, current, voltage and H_β intensity. The current measured by means of an integrating transformer, has the slow rise of ~1ms because of the large (~ 0.3mH) inductors in the bank. The voltage, measured by a differential voltage divider, falls after the initial breakdown giving a minimum after 50 μs. Subsequently the voltage rises rapidly to 1 kV and thereafter continues to rise, but more slowly, until at 600 μs it is above 1.5kV. After this time, the voltage trace becomes highly non-reproducible, but the general trend is downward until after 1 ms, when voltages are ~500–700 volts. The H_β emission is characterised initially by a highly regular signal of period ~8 μs and steadily increasing amplitude. The peak to trough ratio stays at the high value of ~10 or greater for some 10 cycles and then starts to fall until at 100 μs these fluctuations have entirely disappeared. Between 100 μs and 600 μs the signal has a ~5Mc/s modulation superimposed. This can have an amplitude as high as 20% of the low frequency signal, but cannot be Shot noise because of the large signals. After 600 μs the H_β signal becomes non-reproducible, like the voltage trace, and falls to a low value ~10% or less of its peak. The continuum emission is very low for the first 600 μs, but thereafter increases in a highly irregular way to the same level as the H_β signal at these times. The line/100 Å continuum ratio at the peak of H_β is 2–3, which for LTE would suggest T_e from 6–10 eV (Griem, 1964). At later times the ratio is ~0.2, which tends to suggest that the continuum is impurity dominated, because for pure hydrogen, we do not expect line to continuum ratios less than ~1. An influx of impurities would account for the non-reproducibility at these late times.

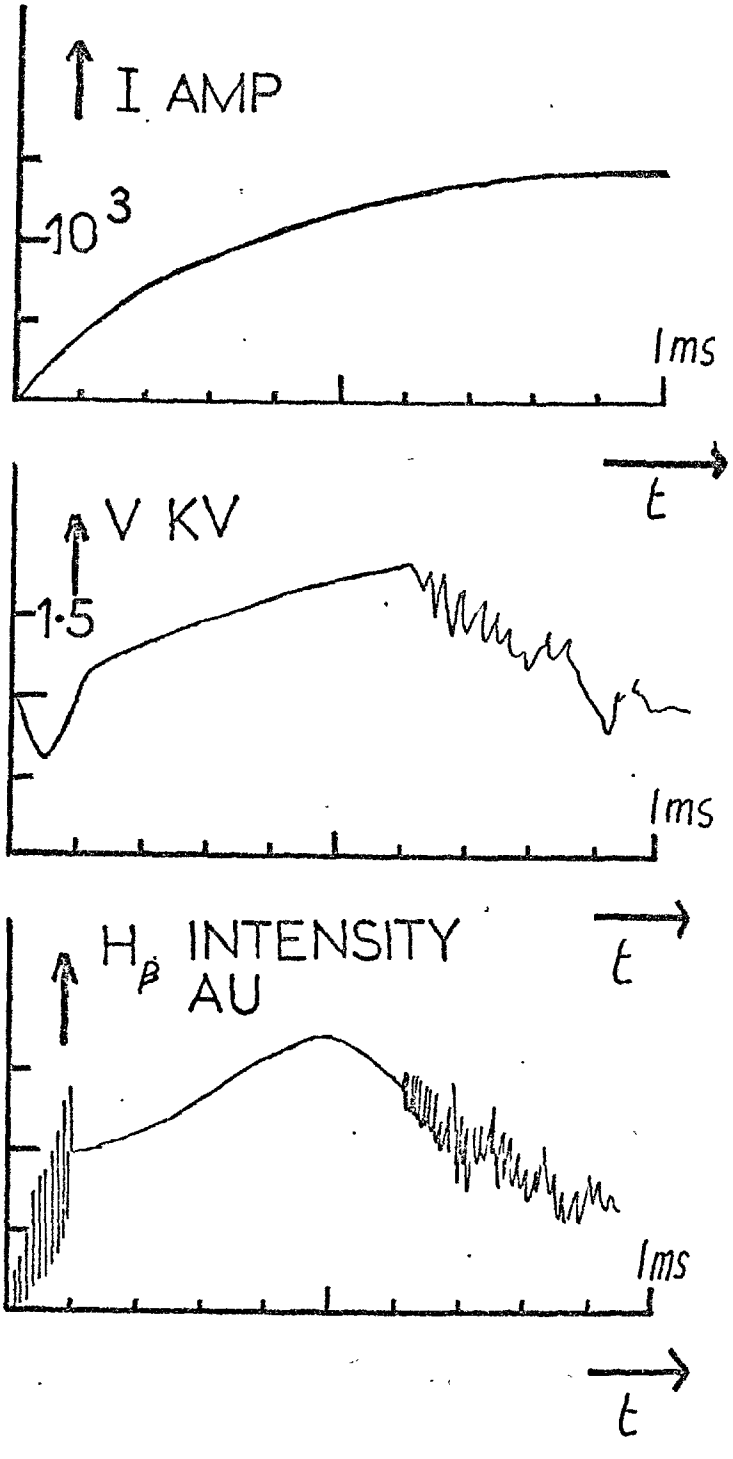

Fig.2.7
Typical discharge characteristics of current, voltage, and H emission as a function of time, t ms

Let us return to the initial periodic emission. The optical port only views a small area of plasma, so the nature of the fluctuation can be examined by the addition of more ports and looking at the relative phase of the emission from various points with two photomultipliers and filters. Azimuthal and axial phase and intensity relationships were measured in this way so as to build up a full two-dimensional picture of the emission as in Fig.2.8. This shows that the channel of emission extends from anode to cathode, but that the feature is most well defined in the first stage, where the emission from the troughs is almost zero. In stage two, it is much less clearly defined, and, at the cathode, only amounts to a small modulation of $\sim 10\%$ on the background level. The whole feature moves azimuthally in the direction of $\underline{E}_z \wedge \underline{B}_r$ for stage one at a velocity of ~ 30 kM/s. At this time we can estimate the E/B electron drift velocity in the azimuthal direction to be ~ 50 kM/s from the voltage traces. Cole (1970), using framing and streak cameras, has detected a periodicity much later in the discharge (at ~ 2 ms, i.e. in the non-reproducible region) which he attributed to a rotating cathode spot. However this is almost certainly the same kind of fluctuation as observed here. Rotating spoke like features are common in other transverse field discharges (Lehnert, review 1971) such as homopolar generators and plasma centrifuges.

2.5 LINE PROFILE MEASUREMENTS

Line profiles should tell us a considerable amount about the plasma, since these should give Stark breadth (giving electron density), Doppler breadth (atom/ion temperature) and Doppler shift (which gives directed atom and ion velocities). The instrument used was a grating spectrometer which, with a 2160 lines/mm grating, had an exit slit dispersion of 5 Å/mm. Unfortunately, due to instrumental defects, it was not possible to obtain an instrument width much better than 0.5 Å, but this should still be able

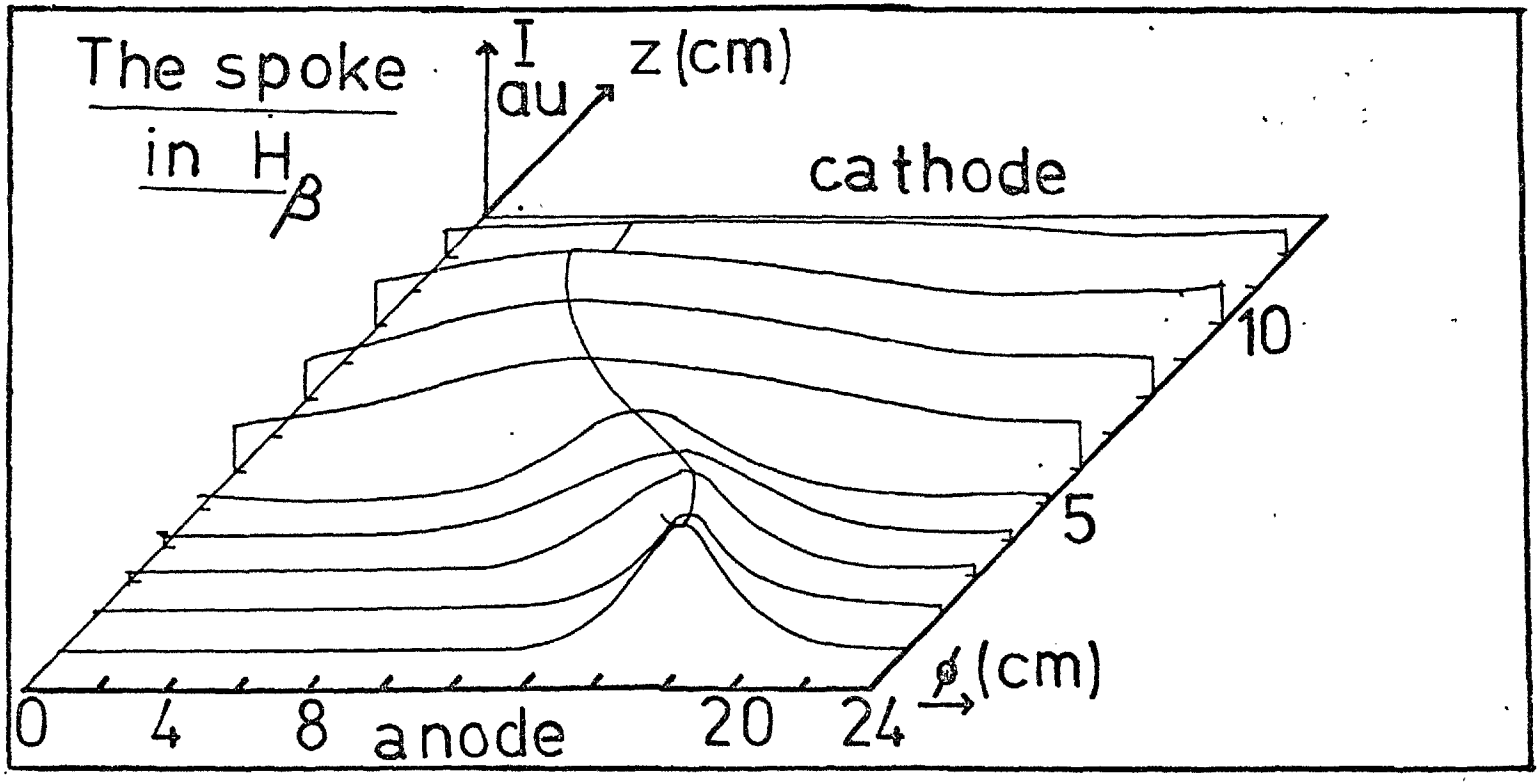

Fig.2.8

The spoke as it appears in H_β light, at 50 μs. The axial (Z) and azimuthal (φ) plane is shown

to resolve Stark breadths of 0.25 Å and electron densities $\geq 5\times10^{19}\,m^{-3}$ using H_β, or densities $\geq 1.4\times10^{19}\,m^{-3}$ using H_δ.

Scanning was done on a shot-to-shot basis, averaging over 3-4 shots to minimise the effect of an $\sim 20\%$ shot-to-shot non-reproducibility. Thus somewhere of the order of 100 shots were required for a typical plasma line scan. However, ~ 500 such shots produced severe wall erosion and crazing, and such a deposit of anode material that the pyrex plasma wall would become $\geq 99\%$ opaque. Thus wall opacity had to be measured and a correction included. This was done, in between shots without destroying the vacuum, by removing the inner magnet and putting a tungsten ribbon lamp inside the inner insulator, which being quartz did not suffer so severe an erosion problem. The ribbon filament was monitored by the P.M. and filter and also by an optical pyrometer. The use of fresh pyrex with each few hundred shots kept this correction, for a single line scan, below 30%. Unfortunately, at this stage it was not realised that truncation of the discharge after $\sim 800\,\mu s$ would remove, almost entirely, the wall damage.

The first Balmer line scans were done near the anode where we expect the highest electron density, and viewing the plasma radially so as to avoid distortion of the line profile by directed motion. The instrument profile was carefully measured at each Balmer line using a hydrogen capilliary discharge which was negligibly broadened. This enables the unfolding of measured line profiles to obtain the true Stark and Doppler broadened plasma profile. Fig.2.9 shows a typical H_β plasma line profile at $200\,\mu s$ and for comparison, the instrument shape. Notice that the profile is strongly asymmetric due to directed motion, but that because the unshifted line centre is not known accurately, we do not know whether this is radially outward or inward. The H_α profile taken at

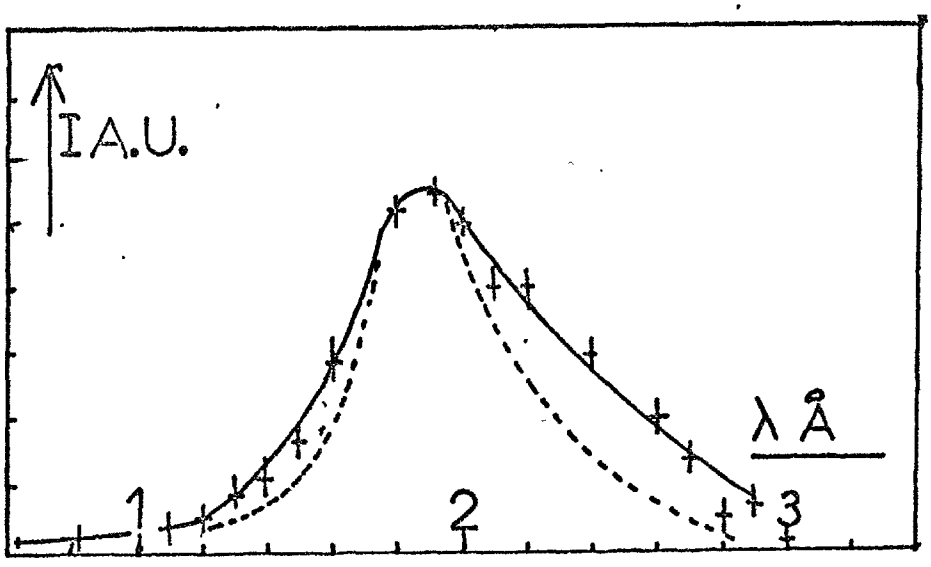

Fig.2.9
H_β line profile at anode at 500 μs. The instrument profile is shown dotted

the same place has the same general shape, but suffers from a worse instrument breadth. This arises because of chromatic aberration in the single element spectrometer lens. The unfolding of the line breadths is performed in Table 2.1, where to a first approximation the Stark breadth of H_α is neglected. The algebraic method used, strictly valid only for a Lorentzian profile, serves to show that the Stark breadth of H_β is small, typically less than 0.25 Å. A more accurate unfolding is unwarranted, since the limitation lies in the shot-to-shot variations. However, the measurement, though null, serves to set an upper limit $n_e < 5\times10^{19}$ m^{-3} on the density.

For an atom-atom collision cross-section $\sigma = 3\times10^{-19}$ m^{-2} (Massey, 1951) and a neutral density $N = 3 \times 10^{21}$ m^{-3}, the mean free path for atoms is small, typically 1 mm. Hence these atoms should be in thermal equilibrium at the Doppler temperature illustrated in Fig.2.10. The shape of this curve seems to follow the discharge current, falling after 400 μs. The non-thermal part of the profile will be due to charge exchange collisions with accelerated ions.

TABLE 2.1

The Unfolding of Stark and Doppler Breadths (in Å)

Time (μs)	$\Delta H_{\alpha M}$	$\Delta H_{\alpha D}$	$\Delta H_{\beta D}$	$\Delta H_{\beta M}$	$\Delta H_{\beta S}$	T_a
100	1.9	0.5	0.37	0.83	-0.14	3.9
200	2.0	0.6	0.44	0.97	-0.07	5.6
300	2.1	0.7	0.52	1.0	-0.12	7.7
400	2.0	0.6	0.44	0.95	-0.04	5.6
500	1.8	0.4	0.3	0.94	0.04	2.5
600	2.0	0.6	0.44	0.85	-0.20	5.6
ERROR	±0.1	±0.15	±0.11	±0.06	±0.25	±3.0

$\Delta H_{\alpha I} = 1.4 \pm 0.05$ Å $\qquad \Delta H_{\beta I} = 0.6 \pm 0.05$ Å

The symbol Δ represents the breadth, and the subscripts M, D, S, I indicate measured, Doppler, Stark and instrument.

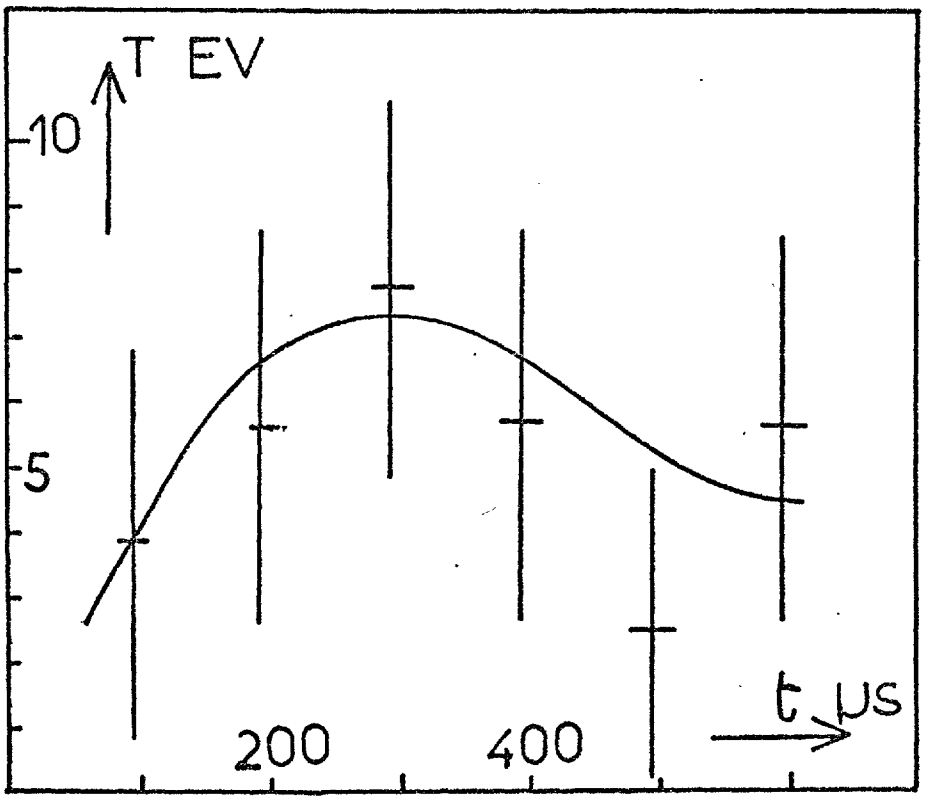

Fig.2.10

The H atom Doppler temperature at the anode against time (t μs)

Notice that the upper limit on n_e is close to the lower limit in equation (2.6) required for LTE to hold for the upper state of H_β, so that the temperature estimates of section 2.4 must be treated with caution. To refine this density limit, we note that the Stark breadth of H_δ is 2.5 times that of H_β. Fig.2.11 gives an experimental scan of H_δ together with a scan on the capilliary source. This last has a substantial continuum, too large for atomic continuum, thought to be H_2 molecular continuum (Massey, 1951). Table 2.2 analyses the breadths, again showing a null Stark breadth and giving a lower limit on density:

$$n_e < 2.5\times10^{19}\ M^{-3} \qquad \ldots (2.9)$$

Hence the upper states of H_α and H_β will not be in LTE. Whereas the low line/100 Å continuum ratio for H_γ and H_δ suggests $T_e \sim 10$ eV, equation (2.5) and the absolute line intensities give $T_e \sim 1.0$ eV. Although the high continuum could be due to impurity, it is likely that H_γ and H_δ are only borderline LTE. Chapter IV deals more comprehensively with spectroscopic diagnosis of the plasma.

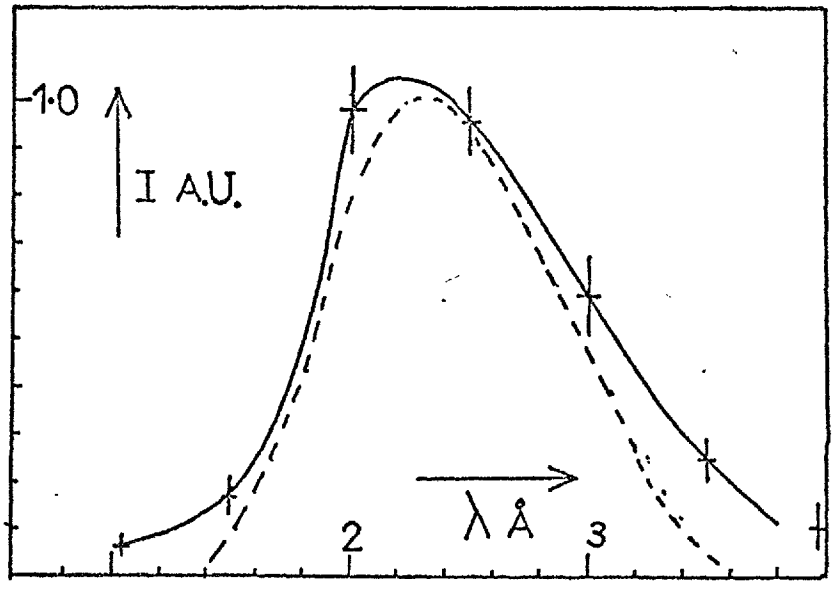

Fig.2.11
H_δ plasma profile at 500μs at the anode.
The instrument shape (λ_{line}) is shown dotted

TABLE 2.2

The Unfolding of H_δ Stark and Doppler Breadths (in Å)

$\Delta H_{\delta I} = 1.3 \pm 0.1$ Å

Time (μs)	$\Delta H_{\delta D}$	$\Delta H_{\delta M}$	$\Delta H_{\delta S}$
100	0.3	1.3	-0.3
200	0.4	1.3	-0.2
300	0.4	1.5	-0.2
400	0.4	1.5	-0.2
600	0.4	1.5	-0.2
ERROR	0.1	0.2	0.4

2.6 H-ATOM DOPPLER SHIFTS

The rate of production of fast neutrals by charge exchange is given by:

$$\frac{dN_f}{dt} = N \sigma n v \qquad \ldots (2.10)$$

where σ is the charge exchange cross section. The ion flux can be estimated from the ion current density. Hence for a 500 amp ion current discharge, the characteristic time for charge exchange is 1 μs. The distance travelled by a thermal atom of Fig.2.10 is only 3 cm in this time, indicating that ions and neutrals should be strongly coupled. Hence atomic line shifts should impart knowledge concerning ion acceleration. The plasma lines of sight for the shift measurements are illustrated in Fig.2.12. These were performed using both single shot and shot-to-shot scans, but the results are similar in either case.

Fig.2.13 shows an axial line of sight measurement taken through the anode port, and, for comparison, the simultaneously measured reference H_α line. Surprisingly, in light of the expected strong coupling, it is found that the line centre is unshifted to within 0.1 Å, corresponding to an H atom directed velocity ≤ 4.5 km/s. If we turn our attention to the line

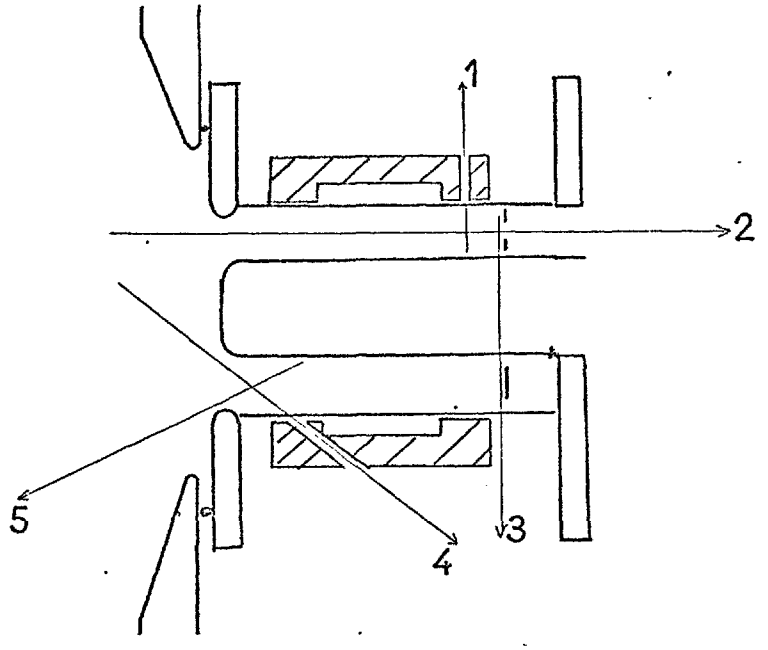

Fig.2.12
Lines of sight for Doppler shift measurements. 1 radial, 2 axial, 3 azimuthal, 4 and 5 oblique in r-z plane

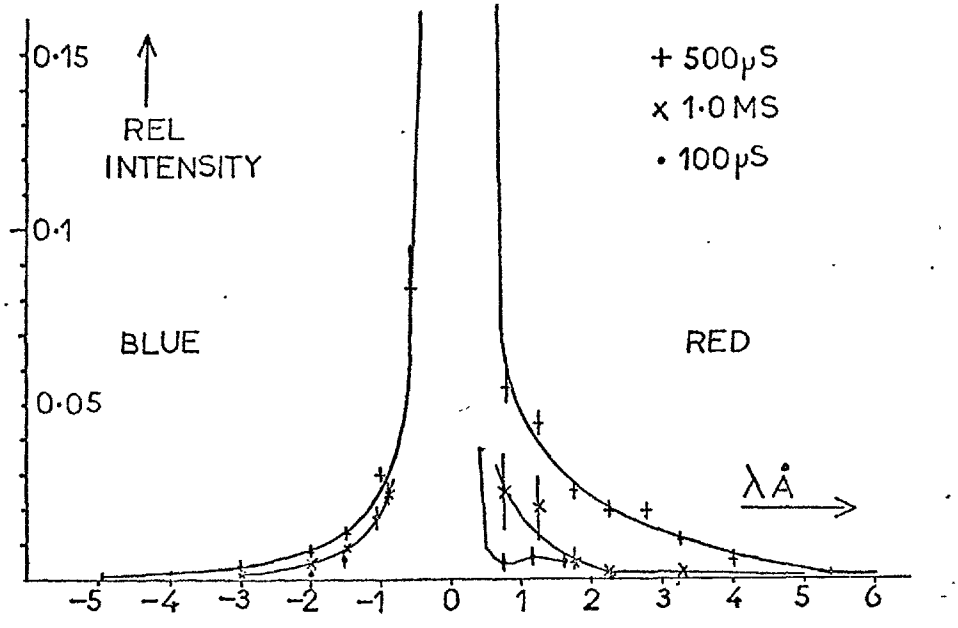

Fig.2.13
The H_α line wings from an axial line of sight profile at 500 μs, normalised to line peak. Also shown are times 100 μs and 1.0 ms, i.e. during the spoke and impurity phases

wings, however, we find that these are time dependent on the red side, which corresponds to motion in the direction of $\underline{E}$. During the middle phase of the discharge (100 - 600 μs) an appreciable red wing is found, of magnitude 2.0 ± 0.3% of the line peak. Since the background continuum is less than 0.1% of the line peak, this wing is clearly a real effect. At these times it is detectable up to shifts of 10 Å. During the initial, spoking phase, the red wing is only 0.5% of peak and extends to only 4 Å, corresponding to 170 eV H atoms. At late times, the wing is somewhat non-reproducible, though still larger than the continuum, being 2 ± 1% at a shift of 2 Å. The disappearance of this wing at a shift of only 4 Å suggests a limit to the mass to charge ratio A/Z for any impurities of 5. It would seem that plasma acceleration is strongest between 100 and 500 μs than either during the spoke or the final impurity phases. Any more quantitive statement will have to await the further diagnostic measurements presented in the next two chapters.

It would be attractive to attribute the observed wing to fast second stage neutrals, and the unshifted component to the slow neutrals in an ionizing first stage. Measurement shows that $\sim 1/3$ of the plasma emission is due to the second stage, whereas the wing is $\sim 1/5$ of the total H_α intensity. Since light collection to the spectrometer uses a lens which focuses the slit image at the anode, and since the cone of acceptance intercepts the walls in the second stage, it is found that the weighting is such that $\sim 1/5$ of the collected light does indeed come from stage two.

In order to check this, measurements were performed on light collected from the second stage alone. It was found that a fibre bundle inside a quartz tube has an acceptance angle of $\sim 10^\circ$ and therefore this could be inserted into the plasma from behind the anode to collect only light from stage two and the exhaust. Angling of the probe tip could ensure that only light from stage two was collected. Measurements performed

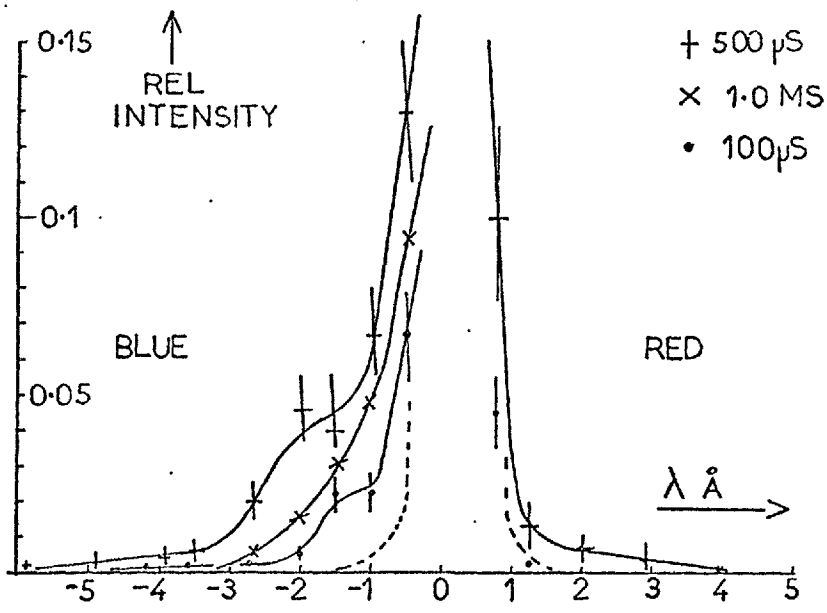

Fig.2.14

The H_α wings from a second stage line of sight profile, taken along line 5 of Fig.2.12. Several times are normalised to the line peak. The reference line is dotted

in this way still gave a strong unshifted component with a red wing ~ few percent of the peak. However because of uncertainty that the probe might seriously disturb the plasma, the second stage line profile was measured along the lines of sight labelled 4 and 5 in Fig.2.12. As can be seen in Fig.2.14, no shift of the central component is detectable, so that the picture of second stage fast neutrals is untenable. Again all the interest lies in the line wings. Because of the direction of the line of sight, the blue wing here corresponds to motion away from the anode. However, the red wing has an appreciable magnitude between 400 and 600 μs , suggesting some ions have a motion which is radially inward, which could be due to an inward radial electric field here. This red feature is not seen in either the initial spoke phase or in the final impurity phase of the discharge.

2.7 LINE PROFILE MEASUREMENTS IN HELIUM

The measurements in the preceding section suffer in interpretation, since the coupling between the radiating atoms and the accelerated ions unexpectedly does not appear to be strong. More information can be obtained about the ion motion if we operate in any other gas but hydrogen

where the atomic ions still radiate. Helium was chosen because its mass is not too different from hydrogen and because it has strong ion lines in the visible spectrum, at 4686 Å and 6560 Å.

The voltage and current traces are broadly similar to those for hydrogen, and the discharge can be subdivided into the same three regimes of initial spoke, main phase and impurity phase. Initial measurements were performed at 6560 Å because shifts would be larger and because it is conveniently close to H_α for this to act as a reference. However it was found that the plasma emission was completely swamped by H_α emission. This hydrogen emission, thought to come from outgassing of the walls and electrodes, was not significantly reduced by firing clean-up shots.

Attention was then transferred to the 4686 Å line, but this suffered from the lack of a convenient reference. Due to spectrometer drive non-linearity in this region, the two adjacent Cd lamp lines at 4678 and 4800 Å were not sufficient to locate the plasma line centre to better than 1-2 Å. Accordingly a capilliary tube flash lamp was constructed. It was found that too high a current gave a uniform continuum and no lines, and that lower current gave a low intensity and didn't excite the ionized helium lines (He II lines). A current pulse of 200 amp for $\sim 1\,\mu s$ for a filling pressure of 100 mT was found to give a He II 4686 Å line sufficiently stronger than the continuum for accurate determination of the line centre. This reference line was found to be appreciably Stark broadened. Fig.2.15 shows the plasma and flash lamp profiles at 400 μs for an axial line of sight. The observed Doppler shift of only 0.8 ± 0.2 Å corresponds to ion energies 50 ± 20 eV at this time. A similar shift is seen during the impurity phase.

This result is, at first glance, surprising, since one might expect shifts due to ions accelerated through the full potential difference of ~ 1 kV. However, a measurement of the emission as a function of

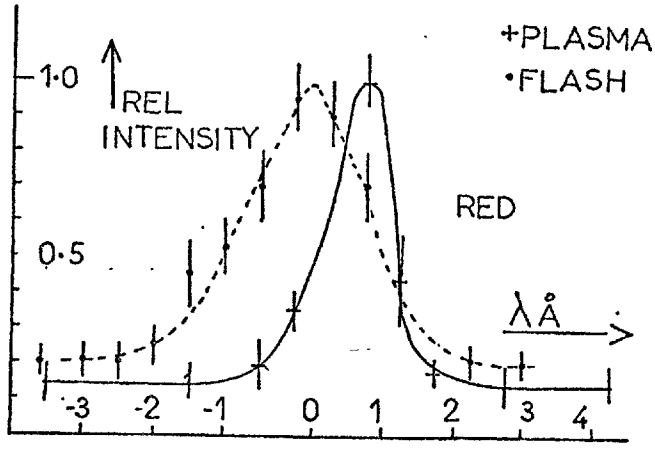

Fig.2.15
The axial line of sight Doppler profile of the helium ion line He II 4686 Å at time 400 μs

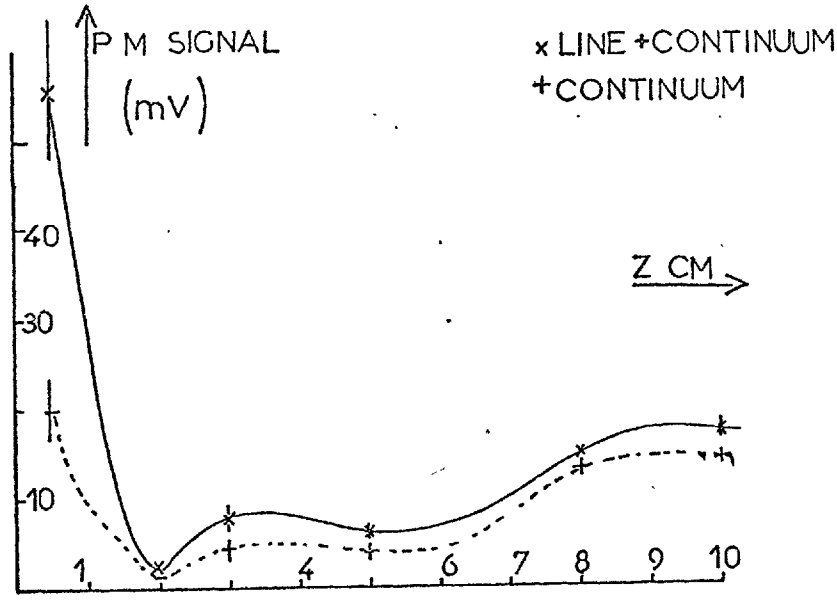

Fig.2.16
The He II 4686 Å line emission in a 5 Å band as a function of distance from anode at 400μs. The continuum is also shown

axial position, Fig.2.16, shows that the axial line of sight average is strongly weighted towards the region within ~ 2 cm of the anode. In addition, the continuum gets relatively more important close to the cathode, again reducing the visibility of any shifted line from the second stage. The voltage drop from anode to ~ 2 cm away is measured elsewhere in this thesis to be 400 ± 50 V, so clearly the ions are not being freely accelerated from the anode, across this region. For $T_e \sim$ few eV and $n_e \sim 10^{19}$ m^{-3}, the ionization time of an He^+ ion is certainly > 1 μs which is greater than the lifetime of a freely accelerated ion in this region. This is evidence for a short mean free path for ion collisions with neutrals in a high density region near the anode.

A scan of the He II 4686 Å emission from the second stage was taken by observing the second stage plasma through the cathode aperture. The results in Fig.2.17 show a line peak corresponding to ~ 50 eV ions as in stage one, but here there is a feature of magnitude $\sim 60\%$ of peak which extends ~ 6 Å from the unshifted line position. However, this shift corresponds to a 2.6 keV He^+ ion whereas the discharge voltage is only 1.3 kV. Such an energy could conceivably come from the recombination, at the cathode, of an He^{2+} ion which has traversed the full anode-cathode distance.

In order to try and confirm this point, a line scan was performed using two different magnetic field strengths on alternate shots. This gives the different voltages of 1.3 kV and 1.0 kV used for the profiles in Fig.2.17. However, the extent of the wing does not fall from that expected for 2.6 keV He^{2+} ions to 2.0 keV ions. Rather for the lower field, the wing extends to that expected on the basis of 1.0 keV He^+ ions. The magnetic field change was effected by switching out the windings on the outer magnet, which will also change the shape of the field lines. It could well be that this change determines whether He^{2+} or He^+ ions are accelerated.

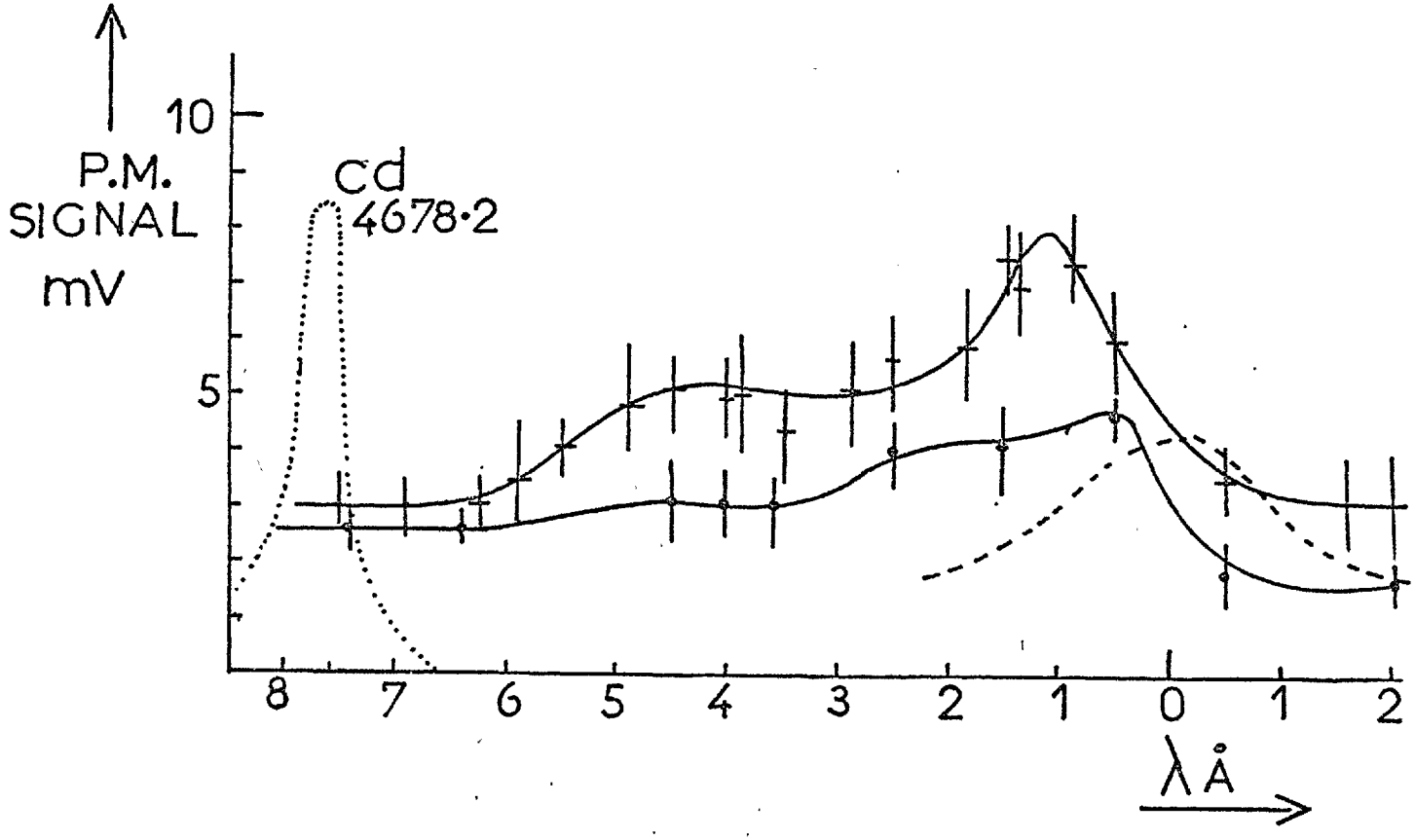

Fig.2.17

The He II 4686 Å line profile in the second stage. + both magnet coils (1.3 kV)
• inner coils only (1.0 kV) .... Cd 4678 Å ---- He flash tube

2.8 CONCLUSIONS

The results in this chapter serve to classify the discharge into spoke, main and impurity phases. Though spoke effects have been observed in earlier low current single stage accelerators, these are not clearly defined. The demonstration that the effect persists into the second stage of a two stage device is rather surprising since $\underline{J} \wedge \underline{B}$ forces, being in opposite directions in the two stages, might be expected to cause disruption.

That the main discharge phase is the optimum accelerating regime is demonstrated by the Doppler profile measurements. These suggest the existence of an ion collision dominated region near the anode. Elsewhere, though, ions and neutrals are only weakly coupled. The helium operation suggests that both ions He^+ and He^{2+} are important and the broad spectrum of ion energies is in accord with the ion-energy measurements of Cole (1970).

The null Stark breadths serve to put an upper limit on the electron density, $n_e \leq 2.5 \times 10^{19}\ m^{-3}$, with the consequence that LTE methods of plasma diagnosis become in appropriate.

CHAPTER III

PROBE MEASUREMENTS ON THE PLASMA

3.1 THE NEED FOR PROBE MEASUREMENT

As is shown in Chapter II, LTE is not valid for the visible hydrogen lines, so that simple spectroscopic diagnosis is not appropriate. For these low densities, microwave measurement is not suitable either, and hence there is no choice but to use electrical probe techniques, being careful the meantime to check for possible plasma disturbance.

3.2 ELECTRIC FIELD MEASUREMENT

The form of the axial electric field is important in determining ion trajectories, as will be shown in a later chapter. The single point probe used consisted of a tungsten tip of area ~ 1 mm sheathed in a small diameter ceramic tube. This was supported by a 5 mm diameter quartz tube which passed through a sliding seal behind the anode. The plasma floating potential was measured relative to the anode, which itself floated relative to earth, by means of a matched pair of voltage dividers. The probe voltage will be close to floating if the probe current $\ll$ saturation current. This condition is well satisfied. The probe floating potential, V_f, only differs from true plasma potential, V_{pl}, by the voltage required to bias off thermal electrons (Lochte-Holtgreven, 1968) so :

$$V_{pl} = V_f + \frac{kT}{2} \cdot \ell n \frac{2M_i}{m_e} \qquad \ldots (3.1)$$

This is negligible, for small T_e, in comparison with the large plasma voltages. Fig.3.1(1) shows the electric field as a function of axial position at a distance 4 cm from the axis of symmetry. This is averaged over the period of the fluctuations. Fig.3.1(2) shows B_r for comparison. Note the different form of E in the two stages. Most of the first-stage voltage is dropped across the first ~ 2 cm from the anode, and thereafter the field is low in this stage. During the spoke (at time 50 μs),

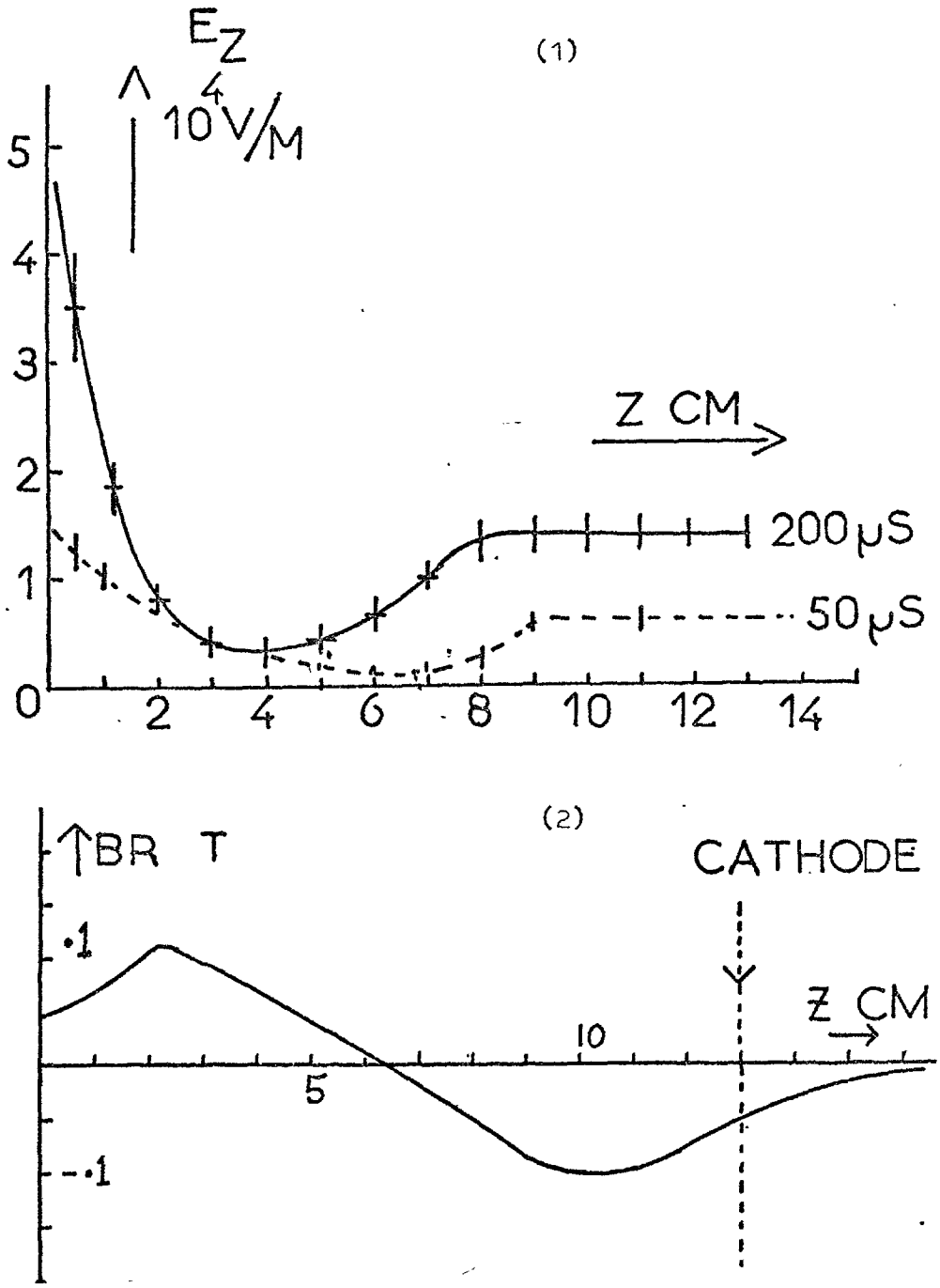

Fig.3.1

(1) The electric field as a function of distance Z(cm) from anode at times 50μs and 200μs .

(2) Shows the applied magnetic field on the same scale.

$E_z = 0$ when $B_r = 0$, but at 200 μs, E_z is already beginning to rise to its second stage value before the B_r due to the magnets changes sign. The Hall currents in the two stages produce a radial B between the stages, but it would take Hall currents in each stage of ~1 kA to shift the reversal point by 1 cm. In the second stage E saturates during both spoke and main phase, so that it is independent of the spatial variation of B.

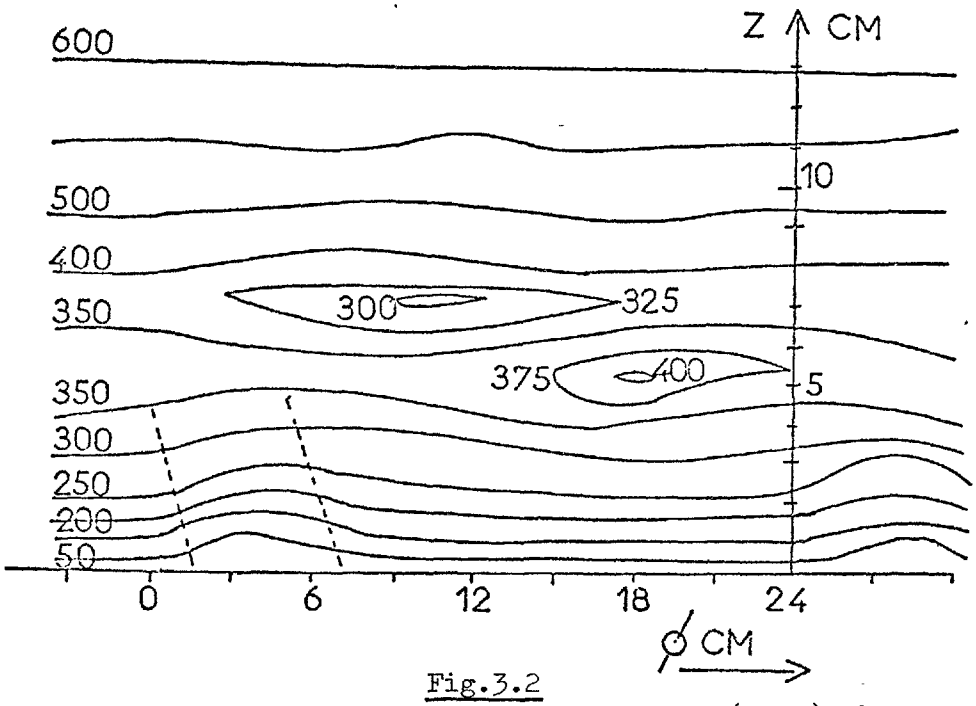

Fig.3.2
The equipotentials in the axial-azimuthal (z--φ) plane during the spoke phase at 50μs. The labels signify the potential in volts relative to the anode

Figure 3.2 shows the distortion of the equipotentials in the axial-azimuthal plane during the spoke. The peak E_θ corresponds to peak light emission, so if this is in phase with a density peak also, there is a net $E_\theta \wedge B_r$ driven electron current contributing to the discharge current.

These results give the ion Larmor diameter $2\rho_{Li} = 2E/(B\omega)$ in the range 1-10 cm depending upon position. Thus condition 1.9 is not well satisfied, since the stage length L = 6 cm. This is discussed further in Chapter VI.

3.3 PROBE MEASUREMENTS DURING THE SPOKE PHASE

3.3.1 Double Langmuir Probe Measurements in the Spoke

In order to measure probe current characteristics, the probe and measuring circuit must be allowed to float. However, the plasma potential may be as much as 1.5 kV relative to earth, so it is not practical to allow the oscilloscopes to float. In addition, there is a potential fluctuation of ~100 V amplitude at ~5 Mc/s, requiring a transformer common mode rejection of better than 1 in 10^3 in order to detect a probe current of 10 mA in a 50 Ω terminated cable. Transformers have a narrow frequency response, typically 100 ns to 10 μs for ferrite cores, whereas times of interest are in the range 100 ns to 10 ms. These problems were overcome by use of light emitting diode (LED) measuring circuits, which were a refinement of circuits used by other workers (Chaqui, 1974) for voltage measurement. The circuit used is shown in Fig.3.3. The LED is biased into the linear region of its V-I characteristic by means of the bias battery B_1. The probe bias is held constant at that set by the battery B_2 by means of the electrolytic capacitors C. The network R_1, R_2 is chosen to keep the diode current to a safe value, and yet giving an effective impedance of 100 Ω to match the twin coax cable. The light emission from the LED depends linearly on probe current to within ~ few percent when suitably biased, and is monitored by a photomultiplier at earth potential. This technique facilitated

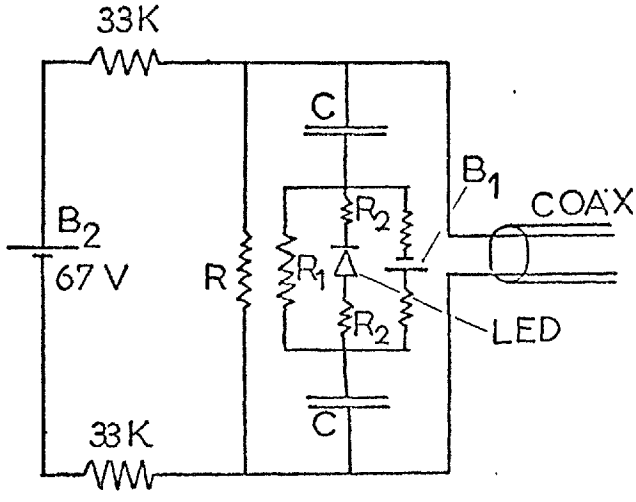

Fig.3.3
LED probe current measuring circuit. The probe bias is applied to the large capacitor C by battery B_2 and voltage divider. The LED is forward biased by means of B_1. The network R_1, R_2 matches the impedance to that of the coax cable.

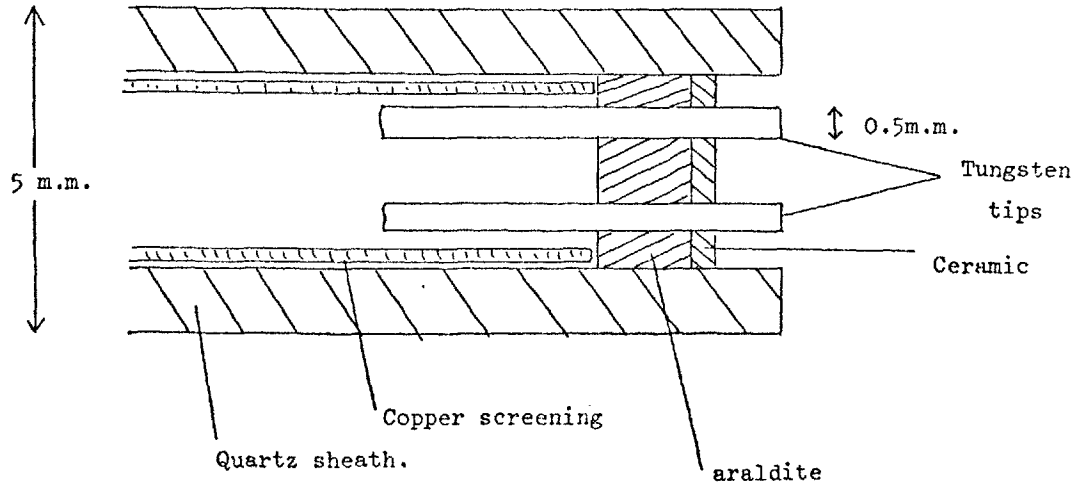

Fig.3.4
The construction of the double Langmuir probe

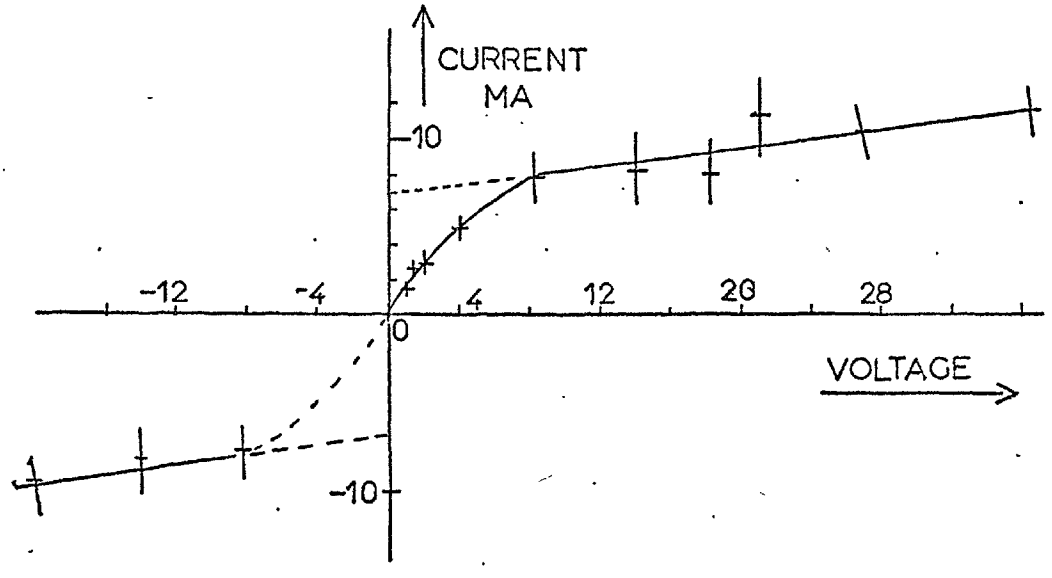

Fig.3.5
The Langmuir probe characteristic 2 cm from anode at 50μs

the measurement of probe currents down to ~1 mA with excellent time response from 100 ns to 2 ms. The common mode rejection is better than 1 in 5000.

The double probe used is illustrated in Fig.3.4. It was found that though protruding tips gave a larger probe area and hence a larger signal, the lifetime was much shorter than for the design shown, where the tips are shielded by the quartz envelope. Even so, the probe only lasts ~30 shots, just sufficient to plot one V-I characteristic such as that shown in Fig.3.5. This characteristic is taken 2 cm from the anode at the peak of the light emission during the spoke phase. Using the results quoted in section 2.2 we obtain:

$$T_e = 2.5 \pm 0.5\ \text{eV}$$
$$n_e = 1.1 \pm 0.2 \times 10^{19}\ \text{m}^{-3} \qquad H^+ \text{ plasma} \qquad \ldots (3.2)$$
$$n_e = 1.5 \pm 0.2 \times 10^{19}\ \text{m}^{-3} \qquad H_2^+ \text{ plasma}$$
$$\text{at time } 100\ \mu\text{s}$$

Besides the uncertainty in ion species, the impurity contribution is unknown. The effective probe area was taken to be that of the plane surfaces, but this is not precise. Thus it is estimated that these density figures are only accurate to 50%.

However, we may still make useful predictions. For a neutral density $\sim 3 \times 10^{21}\ \text{m}^{-3}$ (i.e. 100 mT) electron ion and electron neutral collisions are of roughly equal importance, giving a total electron collision frequency $\nu \simeq 3 \times 10^8\ \text{s}^{-1}$. Thus for B = 0.1 T, $\omega\tau \sim 50$.

3.3.2 The Magnetic Probe in the Spoke

A magnetic probe was used to estimate the current distribution during the spoke phase. This probe consisted of a 50 turn 1 mm diameter coil of turns-area 0.41 ± 0.05 turn-cm^2, and mounted transversely in a quartz sheath. Electrostatic screening was provided by Aqua-Dag high

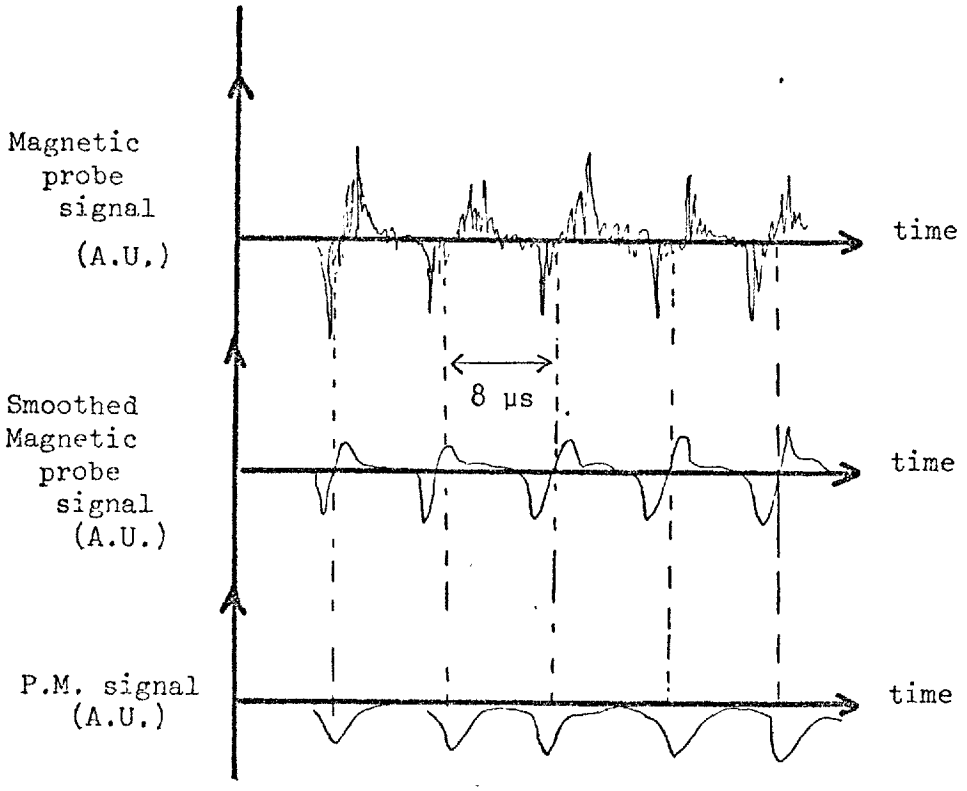

Fig.3.6
Magnetic probe signals; (1) unintegrated; (2) 0.5 μs time constant. For comparison, (3) shows the broad band light emission

conductivity coating. With a terminated probe lead, the sensitivity is uniform down to time 20 ns.

Up to 100 μs, the spoke structure is clearly visible as seen in Fig.3.6 for the alignment of the search coil along $\underline{\theta}$. Superimposed is a high frequency (5 Mc/s) structure. The signal is also shown when this structure is integrated with a time constant of 0.5 μs.

Since the radial and azimuthal dimensions of the spoke are similar (Fig.3.7) the peak B_θ seen at the probe is given by:

$$B_\theta = \frac{\mu_o I}{2\pi r} = 1.6 \times 10^{-5} I \text{ Tesla} \qquad \ldots (3.3)$$

where I is the current carried by the spoke. Integration of the probe signal over one complete cycle gives the amplitude of $B_\theta \sim 0.003 \pm 0.0005$ T. Hence the spoke carries 200 ± 40 amps, i.e. the total discharge current at these times.

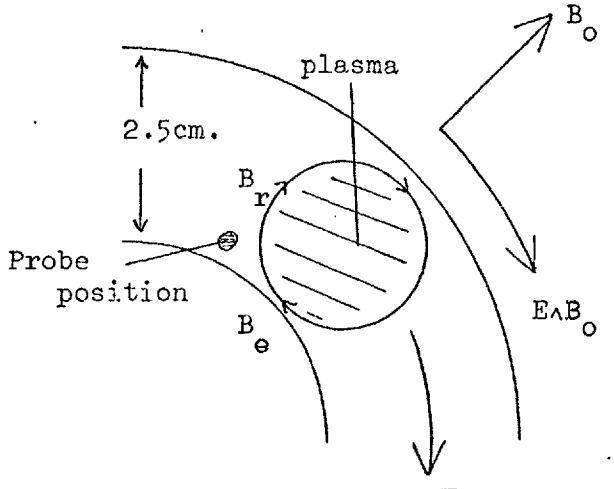

Fig.3.7
The magnetic field associated with the axial streamer (spoke)

The fine structure seen on the probe signals suggests that this current carrying channel is divided into 5–10 smaller filaments of dimensions ~ few mm . That this structure is real, and not a spurious effect such as LC ringing in the probe, can be seen by operation in a heavy gas such as argon. Here the spoke effect is observed also, but with a smaller azimuthal velocity, ~ 8 km/s . The irregular structure is still observed, but with the correspondingly lower period of 1 μs .

3.4 MECHANISM FOR CURRENT FLOW IN THE SPOKE

The electron collisional conduction current can be estimated using equation (1.4), and the experimentally determined $E_z \sim 5 \times 10^3$ V/m. The high value of $\omega\tau$ makes this very small ~ 2.0 ± 0.5 amp. The high $\omega\tau$ does not give the expected efficient acceleration, since, as measured in section 3.5.4 the ion current is only 4 ± 1 amp.

Since there is no current flow ($\leq$ 10 amp) in the spoke troughs, this suggests that the spoke is characterised by a density variation peaking close to the light emission. If this is the case, there will be a net axial $E_\theta \wedge B_r$ drift of electrons in the spoke. Using Fig.3.2 and

result (3.2), this E∧B driven current can be estimated to be 45 ± 25 amp

Large electric fields E_θ are observed to arise associated with the spoke structure. It is plausible that $E_\theta \wedge B_r$ driven currents associated with these fields give rise to the remaining 100 amp of current. However, in the absence of evidence for an E/n_e phase relationship, a more precise account is not possible.

3.5 THE CURRENT CARRIED BY THE IONS

3.5.1 The Ion Probe

Cole (1970) has already used a multi-grid probe to measure the ion current and ion energy distribution in the exhaust of the accelerator. However, such probes are unduly large (~ 10 cm dia.) and employ fragile grid electrodes. The probe measurements already mentioned show that the erosion problem is too severe to contemplate the use of a small gridded probe inside the accelerator itself. But, we can obtain useful information concerning the ion flux from the simple plane probe illustrated in Fig.3.8, where the expected ion flux is normal to the probe surface. If the ion directed energy is greater than typical sheath voltages, i.e. $E_i \gg eT_e$ then the ion current to each probe tip is : $J_+ = nev$, where v is the ion velocity. for any probe bias. The electron current is still, of course, bias dependent. At large bias voltages, one tip moves closer in potential to the plasma and the other becomes more negative relative to the plasma. Eventually no electrons reach the negative tip, so that the probe current is given by the ion flux. To maintain the condition of no net current flow, the other probe tip emits an electron current $i_e = 2i_+$. At low voltages the characteristic is given by the number of electrons with sufficient

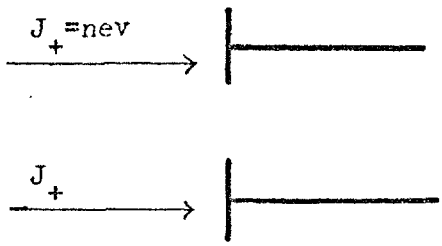

Fig.3.8
Schematic ion probe

energy to surmount the sheath barrier, and so we may obtain T_e as in section 2.2 from $dI/dV_{v=o} = ei_+/(2kT_e)$.

The quartz probes used in earlier sections were found to be too fragile for satisfactory use over many shots, so a new probe design was developed. Ceramic was chosen for its better refractory performance (Lochte-Holtgreven, 1968) and a probe constructed as shown in Fig.3.9.

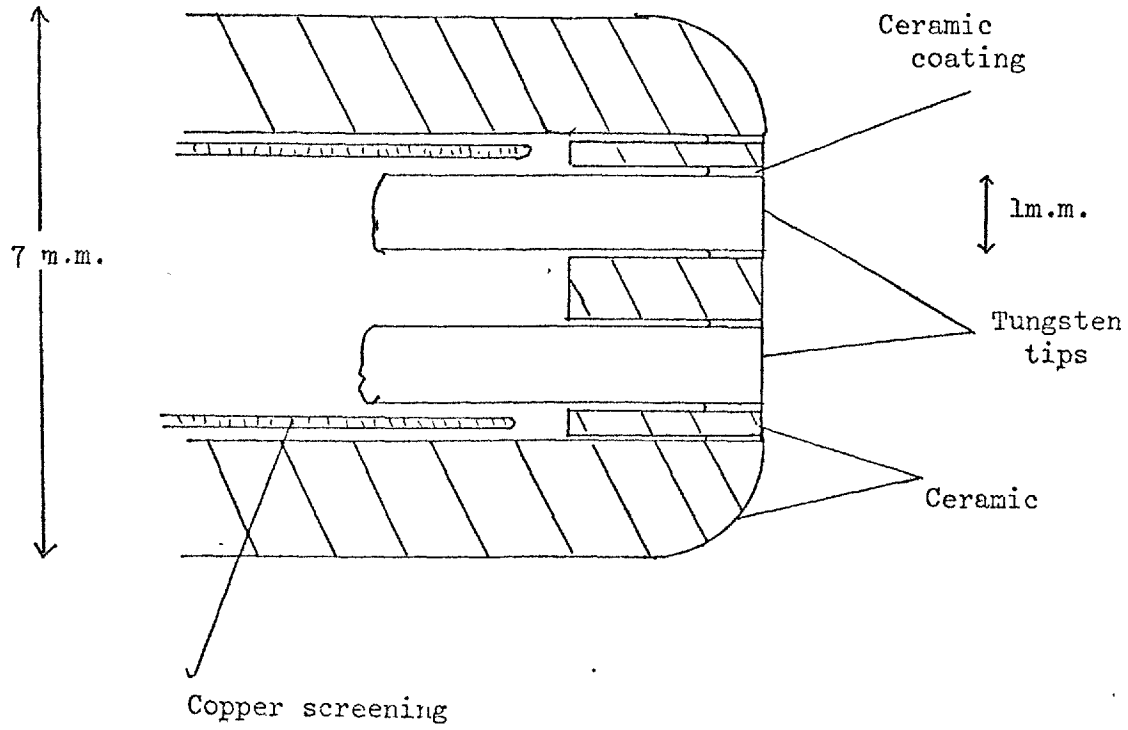

Fig.3.9
Construction of a robust ceramic ion probe

The probe tips were made flush with the ceramic so that the area of the probe is well defined. Gaps in the ceramic were plugged with many layers of ceramic coating. It was found essential to radius the end of the ceramic tube to prevent flaking and splitting during the discharge. The probe was mounted so as to access the discharge via the cathode aperture and to face the accelerated plasma. In practice most damage occurred on the side of the probe, where it intercepted the Hall currents. Serious blistering and erosion would occur after 50-100 shots, but only surface damage which could be ground away. Surprisingly the probe tip would suffer almost no damage.

As with the Langmuir probe, currents were measured using the LED optical transformer.

3.5.2 Measurements in the Plasma Exhaust

First measurements with the ion probe were made in the exhaust where erosion problems are expected to be less severe. A typical probe characteristic is shown in Fig.3.10, in this case at the cathode aperture at 500 μs. From the slope at zero current, the electron temperature is estimated to be $T_e = 3.1 \pm 0.2$ eV, and doesn't vary significantly in time up to 500 μs. Such characteristics were measured and temperature estimates made at several points in the exhaust, and the temperature always found to be close to 3 eV. This temperature was thought to be characteristic of a recombining plasma, where there is no Ohmic input.

The saturation current was measured in detail as a function of position, to build up the picture of ion current density shown in Fig.3.11 at 500 μs into the discharge. These clearly illustrate the divergence of the ion beam already studied calorimetrically by other workers (Cole, 1970). The edge of the beam has a cone half angle as large as 45°, seen on the axial ion flux, whereas Cole obtains the lower value of 30° from the calorimeter. However the discrepancy is not entirely unexpected, for three reasons. First, a calorimetric measurement is weighted towards the higher velocity ions which, because of their larger Larmor radius, will be less strongly divergent. Secondly, Cole uses a beam tank of only 15 cm in diameter, whereas here a tank of 50 cm is used. The smaller tank will naturally limit the beam divergence. Thirdly, the impurity dominated phase will be characterised by a lower divergence, but the calorimetric time average will include this phase also.

Integration of these current densities over the cross-section of the beam gives total ion flux $I_{ion} = 360 \pm 30$ amp at 500 μs when the

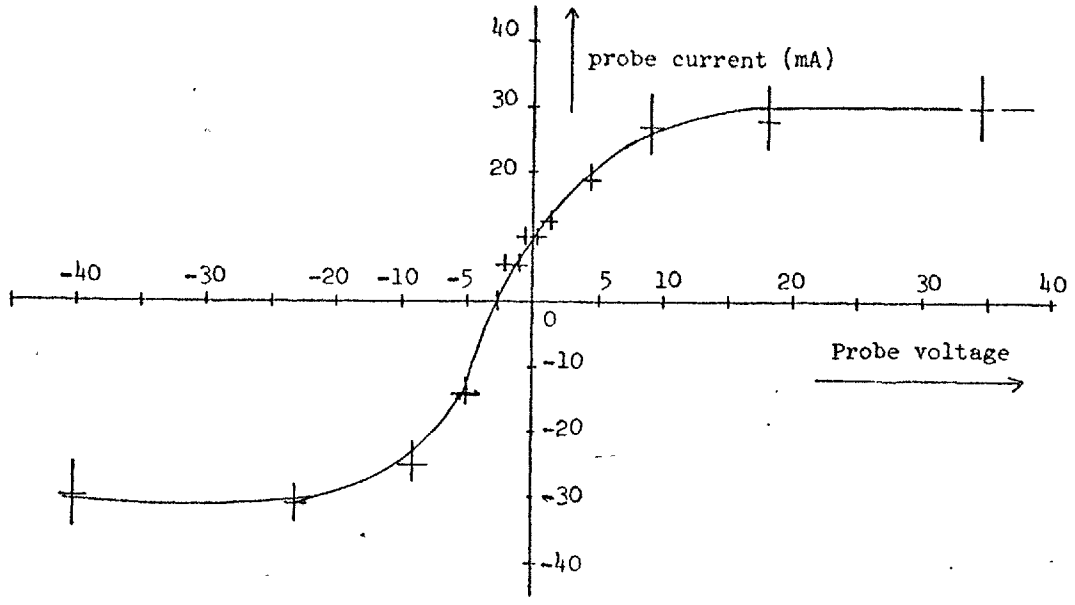

Fig.3.10
Ion probe characteristic in exhaust plasma near cathode

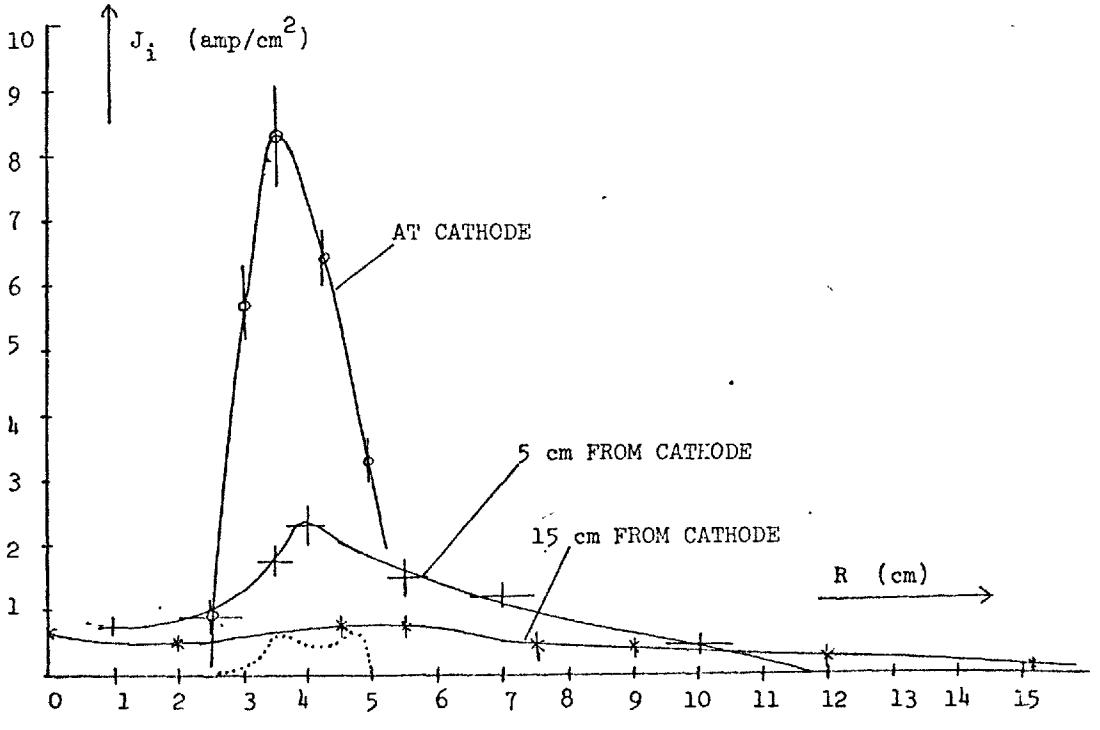

Fig.3.11
Ion current density as a function of radius in the exhaust at 500 μs.
The values during the spoke are shown dotted for comparison

discharge current is 1200 amp. The efficiency in terms of ion to total current is only ~30%.

The exhaust potential is low, up to 40 ± 10V. Since T_e is uniform, there is no need to correct for the difference between floating and plasma potential. The low potential, compared to the discharge voltage, demonstrates that the beam is well neutral, and that no space charge fields significantly retard the exhaust ions.

The ion current during the spoke is 30 ± 5 amp when the total discharge current is 150 amp. Ions carry ~20% of the current, which is a smaller fraction than in the main discharge phase. This shows that acceleration is less efficient during the spoke, but not catastrophically so.

3.5.3 Measurements Inside the Accelerator

The measurements are important in that they supply information concerning the build-up and geometry of the ion flux, giving a spatially resolved picture of Hall acceleration. Full probe characteristics were taken at 2 cm intervals, and having located the saturation current plateau, the profile of ion flux across the channel was measured. Looking at the main phase of the discharge first, Fig.3.12 shows a typical ion probe characteristic, in this case 2 cm from the anode at time 500 μs. This is averaged over the fast fluctuation. The current plateau is fairly well defined, but at larger probe bias (15 - 25V) a sudden rise in current is seen. This is probably due to arcing between the probe electrodes because of the large electric field (~20 kV/M) between them.

Figure 3.13 shows the radial dependence of ion current density as a function of position at 500 μs. Notice that the first stage ion current flows within ~1 cm of the outer plasma wall. This might explain the severe wall erosion found here. In the second stage, the ion current

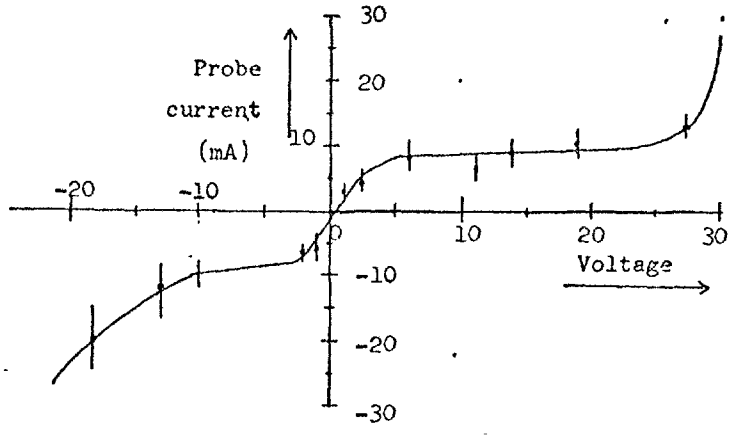

Fig.3.12

A typical ion probe characteristic, in this case at 2 cm from the anode and at 50 μs

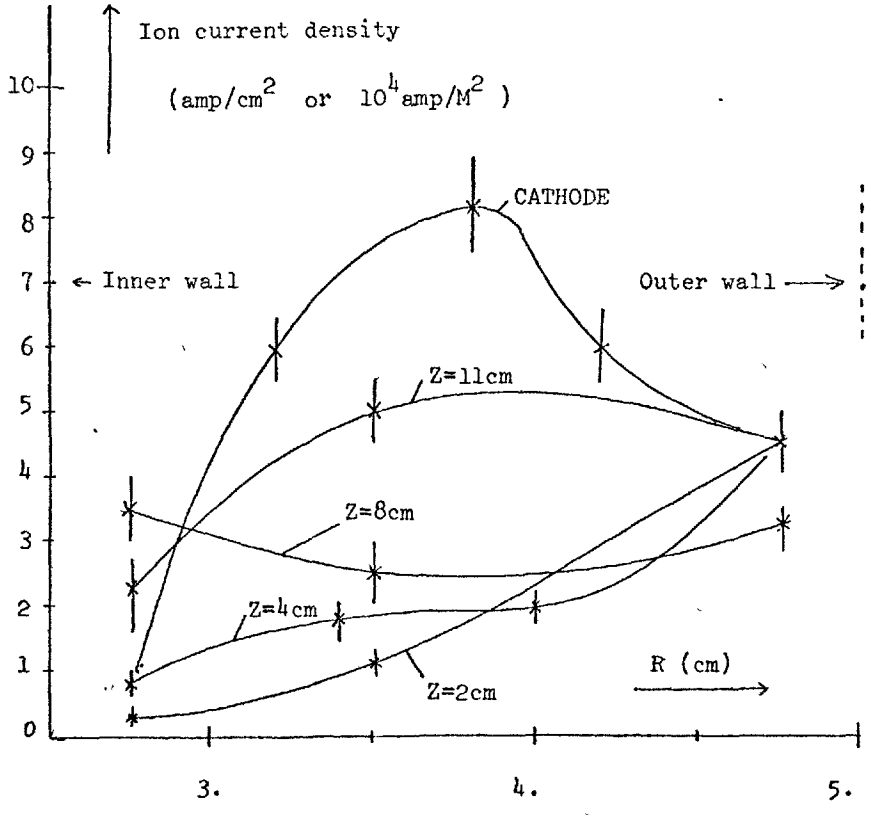

Fig.3.13

Ion current density as a function of radial position (R) inside accelerator at 500 μs. Each curve is labelled by distance from anode in cm (Z)

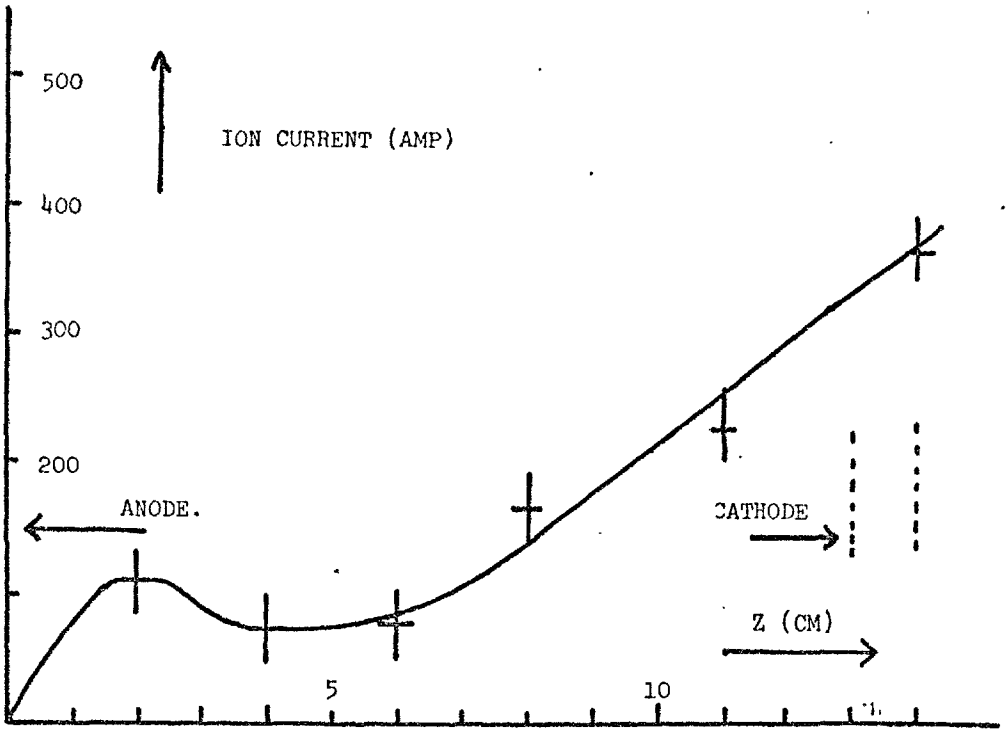

Fig.3.14

The axial dependence of the total ion current at 500 μs

peaks in the centre of the annulus. This occurs at larger r nearer the cathode, consistent with the large beam divergence. Integration of these radial profiles gives the axial dependence of the total ion current in Fig.3.14. There is a large gradient of flux close to the anode and in the second stage, but no growth in flux between 2 and 6 cm from the anode. Examination of Fig.3.1 shows that this plateau corresponds to the minimum in the electric field. Neglecting radial fluxes, the gradient of ion flux is a measure of ionization. In Chapter IV, these results are compared with the ionization rate obtained spectroscopically.

The results differ significantly from those of Zubkov (1971), where in a larger device operating at lower current, the ion flux rises to a plateau of $\sim\frac{1}{2}$ the discharge current within $\sim\frac{1}{3}$ of the first stage. No further increase is observed in the second stage. The slow growth of flux observed in this thesis could be a serious limitation on operation at high current densities. This point is dealt with in Chapter VI.

3.5.4 Ion Current During the Spoke

On the ion current signal, the spoke appears as a modulation of the faster ~5 Mc/s fluctuation. If these modulations are indeed streamers moving along with the spoke, then the size of each is 5-10 mm which is much larger than the probe size, so that no difficulty in interpretation should arise. In stage one, the spoke carries a peak ion current density of $4 \pm 1 \times 10^3$ A/m^2, giving a total ion current of only 4 amp. In stage two, the current density of ions is similar, but uniform, giving a total ion current 30 ± 5 amp. These correspond to 4% and 20% of the total discharge current, compared with 7% and 30% for stages one and two at 500 μs.

3.5.5 Ion Current in the Impurity Phase

The final phase of the discharge after 500 μs is treated separately here because of the marked difference in the character of the plasma as described in Chapter II. The ion probe results are different also — the amplitude of the high frequency fluctuation is much reduced, but the ion current becomes much more non-reproducible from one shot to the next. However it is still possible to obtain well saturated ion probe characteristics.

Figures 3.15, 3.16 and 3.17 summarize the results of measurements at these times, and show the spatial distributions of the ion current density in the accelerating plasma, and in the exhaust and the axial dependence of the total ion current. These results differ in several important respects from those in the earlier discharge phase. The ion flux in the first stage does not hug the wall, but, within the error bars, is fairly uniform across the channel. This results in a steadier increase in ion flux over this stage, and no plateau is seen. The electric field is more uniform also, and there is no difference between first and second stage. However, at the cathode aperture, the total ion current is similar to that

in the earlier phase, despite the fact that the total discharge current has increased from 1 kA to 1.5 kA. Consequently the ion current carrying efficiency is slightly worse at 20%. The divergence of the exhaust is similar to earlier times, and is not increased by a lower discharge voltage. This suggests that either the ions are created nearer the anode, so that their energies are similar, or that the mean ion mass has increased.

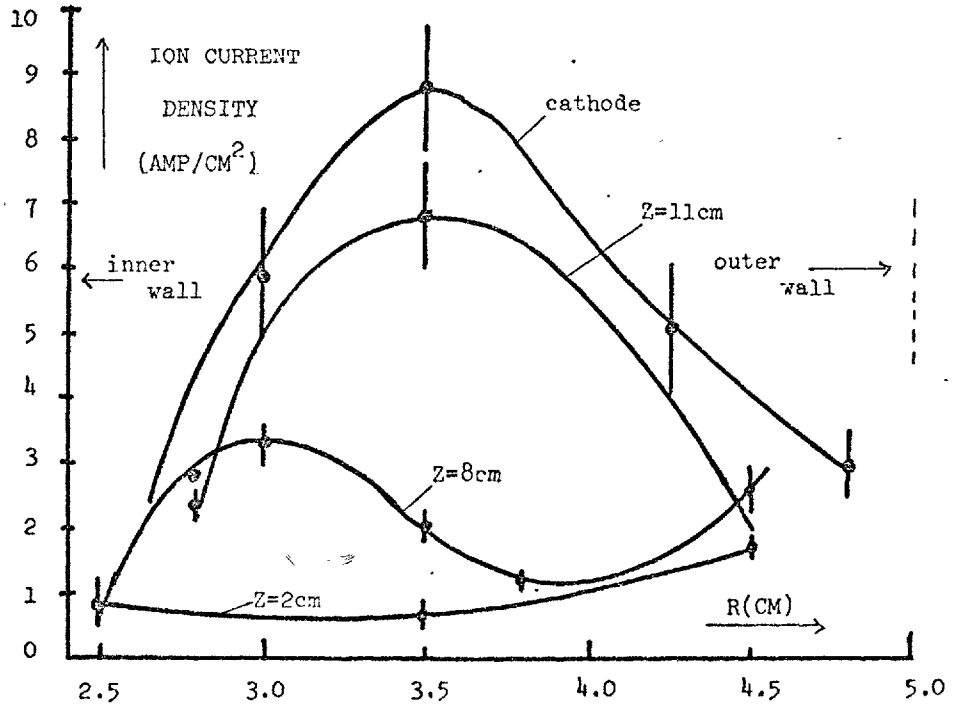

Fig.3.15
Distribution of ion current density as a function of radial position (R) for various distances (Z) from the anode at 1 ms

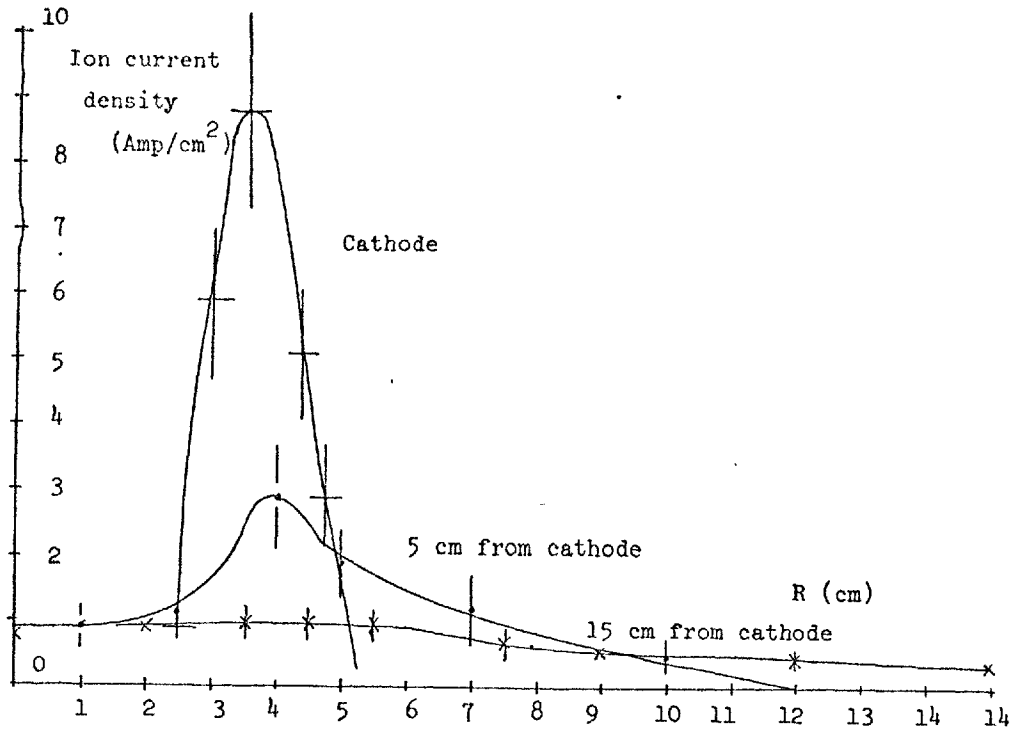

Fig.3.16

Ion current density as a function of radius (R) in the exhaust at 1.0 m.s at the cathode. 5 cm from cathode and 15 cm from cathode

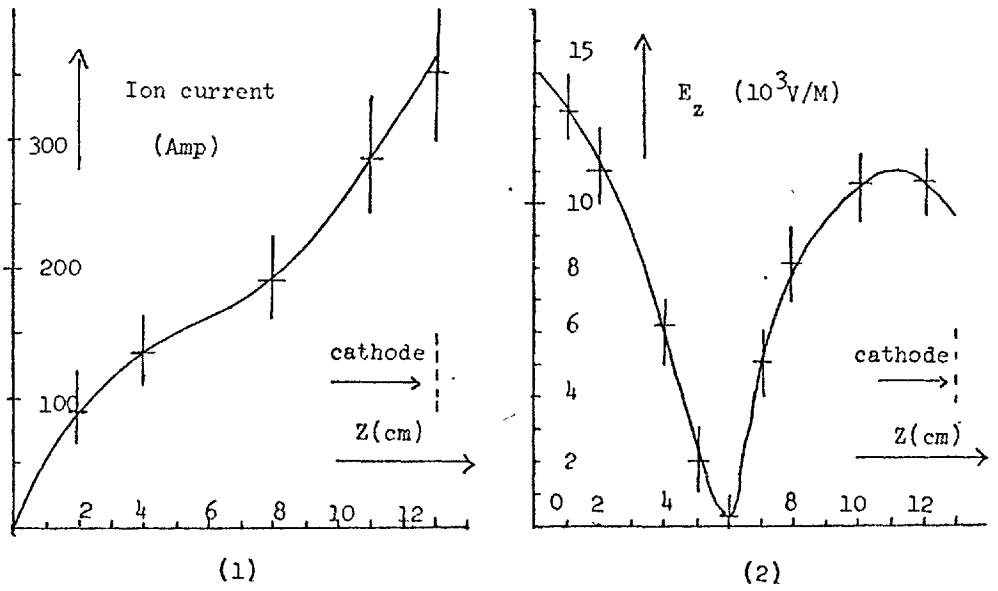

Fig.3.17

(1) The build-up of total ion current and (2) the axial electric field (E_z) as a function of distance from anode (Z) at 1.0 ms, during the impurity phase

3.6 SPATIALLY RESOLVED ELECTRON TEMPERATURE

Care in plotting the ion probe characteristic at low values of bias voltage enables an estimate to be made of the electron temperature, as mentioned previously. Fig.3.18 shows the values of T_e obtained at various times in the discharge. Accuracy is greatest in the main phase: at early times the signals are too small, and at late times, too non-reproducible, for a good determination of T_e. In the main phase, first stage, second stage and exhaust are characterised by three different temperatures: 2 ± 1 eV, 6 ± 1 eV and 3 ± 0.5 eV. The low values are reminiscent of the plateau of Fig.2.1, i.e. high plasma density or low current density. The higher value in stage two suggests a lower n_e off this plateau. These temperatures are roughly time independent from 200 μs in the main phase to 1 ms in the impurity phase. The results for the spoke are different, a temperature of 2 ± 1 eV applying throughout the accelerator, suggesting a roughly uniform electron density. The behaviour late in the impurity phase suggests n_e is once more somewhat uniform.

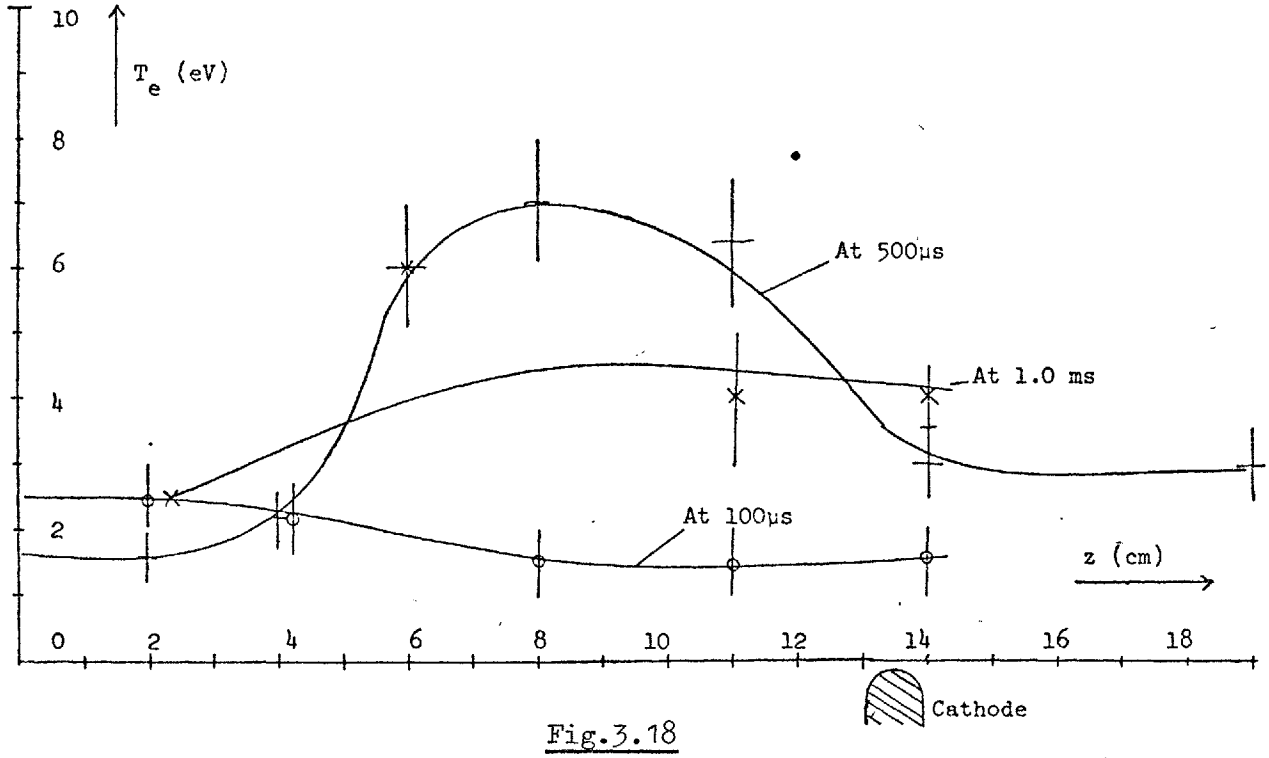

Fig.3.18

The electron temperature as a function of distance from anode (Z) at times: 100 μs, during the spoke phase; 500 μs, in the main accelerating phase and at 1.0 ms, during the impurity phase

3.7 THE ROGOWSKI PROBE MEASUREMENT OF HALL CURRENT

Previous measurements of Hall current have used a conventional magnetic probe to sense the axial magnetic field due to the current (Cole, 1970), and calibrated with a uniform current distribution in a coil. The Rogowski loop, which effectively measures $\int B.d\ell$ round a loop, gives the total current independently of its distribution. The construction of the probe is shown in Fig.3.19. It was made by winding the fine gauge wire evenly on a former of 16 SWG enamelled wire, then after insulating with Mylar tape a layer of Al foil was wrapped around to serve as electrostatic screening. The wire former was then bent into a rectangular loop and many layers of ceramic coating painted on to give protection from the plasma.

Such a probe is considerably less robust than conventional ceramic ones and it was found necessary to use very short discharge pulses to prolong the probe lifetime. No detectable plasma perturbation would occur for times less than 250 μs, but thereafter the discharge characteristics were completely altered. Fig.3.20 shows the Hall current measured in the second stage, as a function of time, after smoothing out the high and low frequency periodicities. This shows that the Hall current only starts to rise towards the end of the spoking phase. This is presumably because little Hall current can flow in the low density regions of the spoke. The Hall current rises to 260 ± 50 amp at 250 μs but values at later times confirm disruption due to the probe.

At these times, measurements in stage one detected no Hall current down to the electrostatic pick-up level given by ~ 50 amp. This is further evidence for the differing behaviour of the two stages.

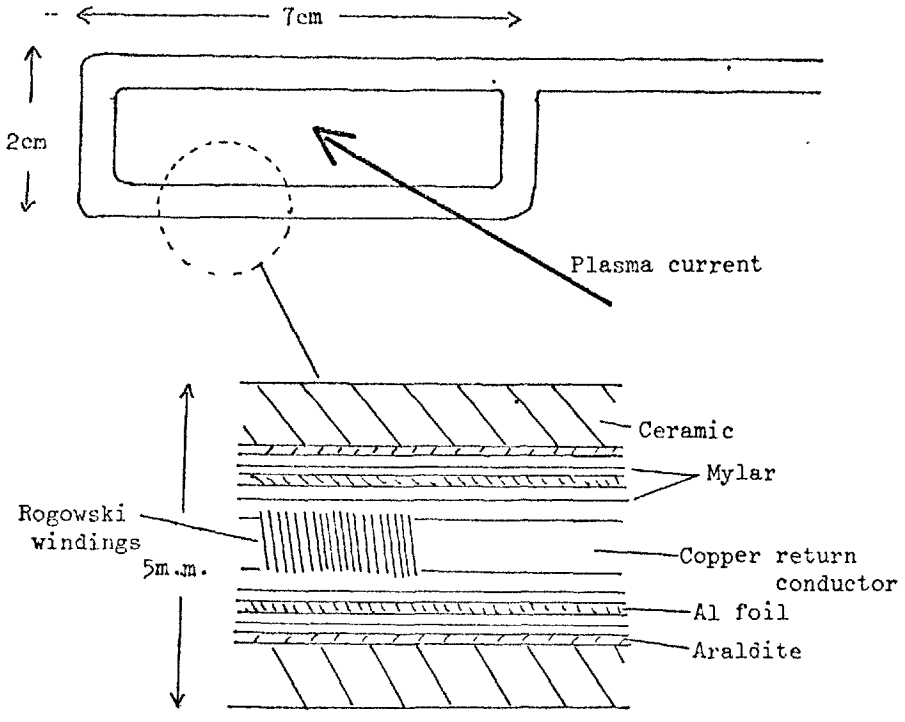

Fig.3.19
The construction of the Rogowski probe for measurement of Hall currents

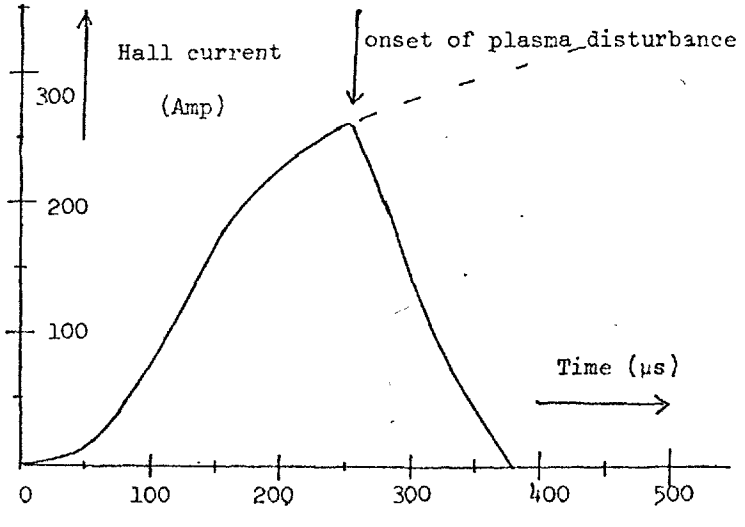

Fig.3.20
The second stage Hall current as a function of time

3.8 DOUBLE ELECTRIC FIELD PROBE MEASUREMENTS

The electric field measurements presented in section 3.2 suffer from poor time resolution (only $\sim 1\ \mu s$), and in addition, plasma non-reproducibility makes local electric field measurements with a single probe difficult. Using a double probe and a biased LED voltage measuring system similar to Fig.3.3 but without the probe bias network, a time resolution of 20 ns, and a common mode rejection of 10^4 can be obtained, and plasma voltages as low as 0.2V measured. With such a system it is possible to measure radial and azimuthal fields in the accelerated plasma.

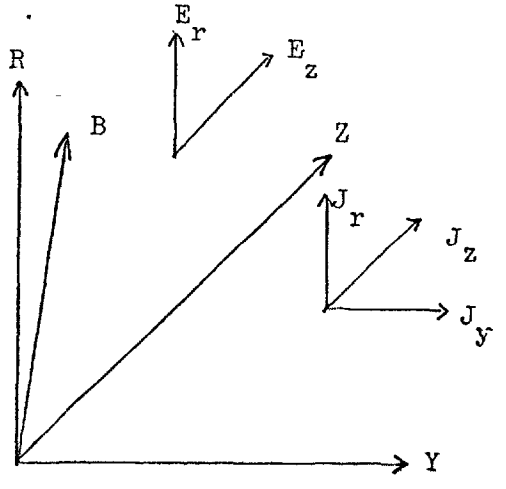

Fig.3.21
The reason for E_r. The magnetic field B lies in the R-Z plane

It is simple to show that a radial electric field is to be expected everywhere where B is not purely radial. Let us consider a field with components B_r, B_z, E_z and E_r in the r-z plane of Fig.3.21, then we can write the three components of the generalised Ohms law:

$$\begin{aligned} J_z &= \sigma E_z^* + J_y \beta_r \\ J_r &= \sigma E_r^* - J_y \beta_z \\ J_y &= \sigma E_y^* + J_r \beta_z - J_z \beta_r \end{aligned} \qquad \ldots (3.4)$$

where $\underline{\beta} = \sigma \underline{B}/(ne) = \underline{\omega\tau}$, and $E^* = \underline{E} + \underline{v} \wedge \underline{B} + \nabla p/(ne)$.

For a narrow discharge chamber with insulating walls then $J_r = 0$. If we assume Y symmetry we can solve the equations (3.4) to obtain

$$E_r = - v_y B_z - \frac{\nabla_r p}{ne} + \frac{\beta_z}{1+\beta_r^2}\left[-\beta_r\left(E_z - v_y B_r + \frac{\nabla_z p}{ne}\right) + v_z B_r - v_r B_z\right] \ldots (3.5)$$

If we assume $\underline{v}$ to be small, and neglect pressure gradients, then for large $\omega\tau$,

$$E_r = -\left(\frac{\beta_z}{\beta_r} E_z\right) = -\left(\frac{B_z}{B_r}\right) E_z .$$

In other words $\underline{E}$ is perpendicular to $\underline{B}$, and the magnetic field lines are equipotentials. This result is self evident, in that, for a high conductivity plasma the resistive electric field due to current flow parallel to $\underline{B}$ is small.

However, the $\underline{J}_y \wedge \underline{B}$ force, being perpendicular to $\underline{B}$, would drive the plasma into the wall. A steady state solution would then require a radial pressure gradient to prevent this, so that:

$$\frac{mnv_y^2}{r} + J_y B_z - \nabla_r p = 0 \qquad \ldots (3.6)$$

where Y is assumed to be the azimuthal direction, and the centrifugal term therefore added. Together with (3.4) and $J_r = 0$, this gives:

$$E_r = - v_y B_z - \frac{mv_y^2}{er} \qquad \ldots (3.7)$$

for which E_r is not perpendicular to B. Obviously more detailed calculation would be required to find E_r in practice, but it might be useful to consider these as two limiting cases. The former might hold mid-way between the walls where the condition $v_r = 0$ does not hold so strictly, and the latter near the wall when plasma accumulation has occurred.

In view of the importance of E_r in determining ion trajectories as will become apparent in a later chapter, it was thought worthwhile to measure this experimentally. Fig.3.22 shows the values of E_r averaged over the fast fluctuations, and compares them with the E_r estimated from the experimental E_z knowing the vacuum magnetic field. Agreement is close where B_r is large, but in the regions of strong axial magnetic field the approximation strongly overestimates E_r. In the second stage

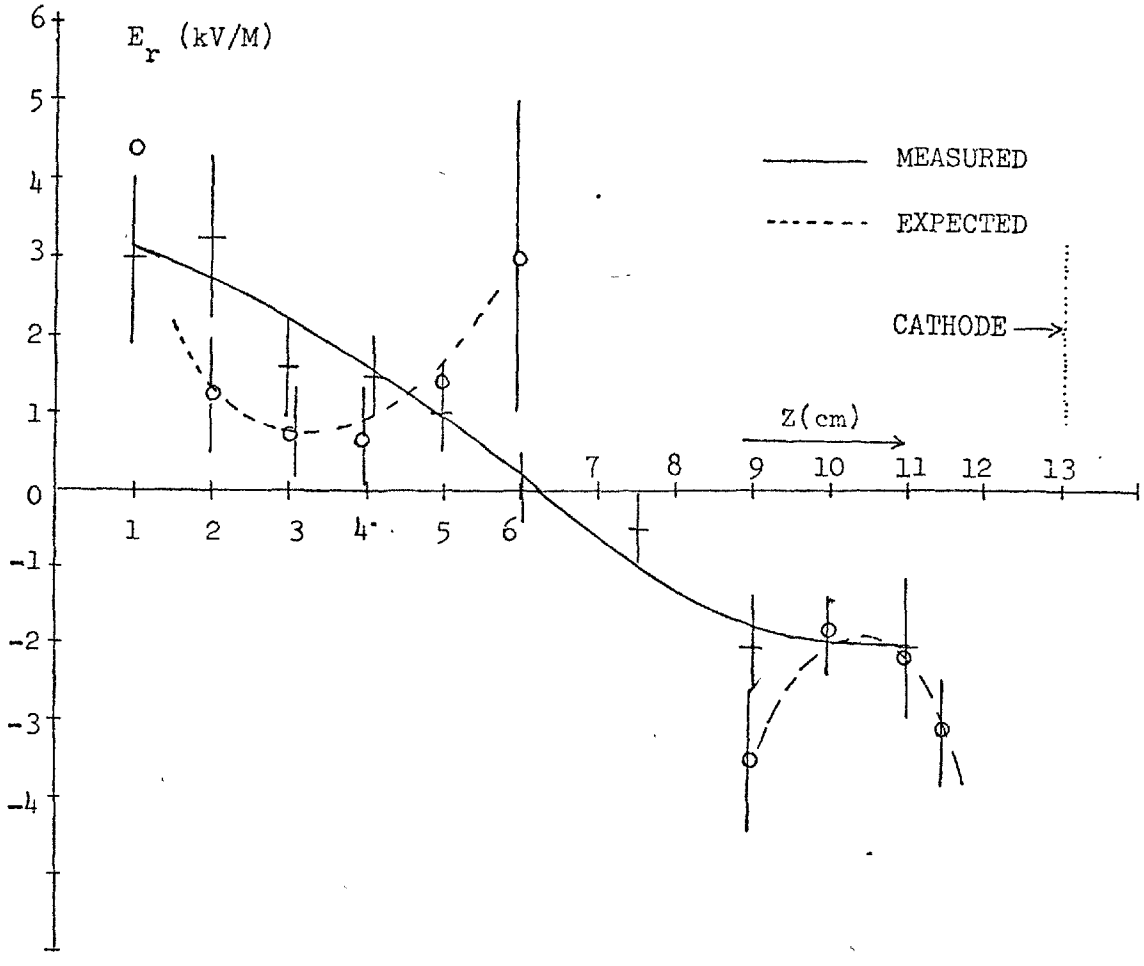

Fig.3.22

The radial electric field (E_r) as measured by double probe is compared to that predicted by the field-line equipotential equivalence. The time is 500 μs.

the agreement is poor, but one might expect this since the plasma flow velocities should be larger.

3.9 SUMMARY OF THE WORK PRESENTED IN CHAPTER III

The results for the spoke in this chapter show that whilst this feature carries almost the whole discharge current, the contribution from ion current and electron collisional conduction current is small. About half the current can be accounted for in terms of the $\underline{E}_\theta \wedge \underline{B}/B^2$ driven electron current associated with the coarse structure, and the remaining being due to the fine structure. The Hall current is small during the spoke phase ($\sim$ few amp) which accounts for the low ion current at these times.

The behaviour of the ion current in the main phase is qualitatively very different from that reported for low current density accelerators (Zubkov, 1971). In particular the plateau of ion current in the first stage followed by a strong increase in the second stage is new. The electric field and Hall current also show how different is the behaviour in the two stages. Only the second stage accelerates effectively. These differences can be understood, qualitatively at least, in terms of the ion trajectory effects discussed in Chapter VI.

CHAPTER IV

DETERMINATION OF PLASMA DENSITY SPECTROSCOPICALLY

4.1 COLLISIONAL RADIATIVE THEORY OF HYDROGENIC STATE POPULATIONS

The optical measurements presented in Chapter II show that the plasma electron density is too low for L T E to be applicable to the population of the Balmer lines. However, several authors have solved the appropriate set of rate equations for hydrogen to predict the steady state level populations for a uniform plasma of known electron density n_e, electron temperature T_e and atomic neutral density N (McWhirter and Hearn, 1963; Johnson and Hinnov, 1973). These show that the state population of a level of principal quantum number p can be written:

$$n(p) = r_o(p)\ n_E(p) + r_1(p)\ n(1)p^2 \exp\frac{E_I}{kT}\left(\frac{1}{p^2} - 1\right) - \tau(p)\ \frac{dn(1)}{dt}\ p^2 \exp\frac{E_I}{kT}\left(\frac{1}{p^2} - 1\right) \quad \ldots (4.1)$$

where n_E is the Saha equilibrium state population, $n(1)$ is the ground state population, E_I is the ground state ionization potential, $r_o(p)$ and $r_1(p)$ are dimensionless coefficients, and $\tau(p)$ is a characteristic time. The first term represents the Saha-like population, and for high electron densities, satisfying conditions similar to (2.6), $r_o(p)$ is close to 1. The second term represents the coupling to the ground state. For example, for a transition optically thick to Lyman radiation, the population relative to ground will be given by the Boltzmann factor so that $r_1(p) \simeq 1$. However, for an optically thin transition, the term gives the balance between collisional excitation from ground and radiative decay. In this case $r_1(p)$ has some dependence, though weak, on n_e and T_e. The last term in (4.1) describes the perturbation of the population due to an influx of ground state neutrals. This is significant if the timescale for the influx is shorter than $\tau(p)$.

The three parameters r_o, r_1 and τ are tabulated (Johnson and Hinnov 1973) for a wide range of n_e and T_e for the two cases of plasma optically thick and thin to Lyman series radiation.

An estimate of the ground state neutral influx rate in the Hall accelerator can be made from:

$$\frac{dn(1)}{dt} = \frac{n(1)V_{th}A}{V}$$

where A is the cross-section of the accelerator, V the volume and V_{th} the thermal velocity of neutrals. Neglecting molecules, $n(1) = N$, giving an influx timesecale $t \sim 10^{-4}$ s. But $\tau \sim 10^{-10}$ for $n_e = 10^{19}$ m^{-3}, $T_e = 2.5$ eV, so that the last term in (4.1) may be neglected.

For conditions $n_e = 10^{19}$ m^{-3}, $T_o = 2.0$ eV, the tables show that Saha-like, and ground state excitation terms are comparable for $p = 6$ and $n(1) = 10^{18}$ m^{-3}. This value of $n(1)$ falls sharply with increasing T_e decreasing n_e or decreasing principal quantum number, p. Since the initial filling pressure gives $n(1) \simeq 10^{21}$ m^{-3} ground state excitation will dominate unless ionization is very nearly complete.

Figure 4.1 plots the relative populations

$$\frac{n(p)}{n(1)} = r_1(p)\, p^2 \exp\left[\frac{13.6}{kT}\left(\frac{1}{p^2} - 1\right)\right],$$

assuming the second term of equation (4.1) dominates, against n_e for $p = 3$ to 6 at $T_e = 3$ eV. In the region $10^{17} \leqslant n_e \leqslant 10^{19}$ m^{-3}, these relative populations $n(3) : n(4) : n(5) : n(6)$ are sufficiently strongly dependent upon n_e to serve as a density diagnostic, provided T_e is known. The neutral density can be estimated from the absolute value of the state populations, again if T_e is known.

If both excited state populations and ionization are determined by electronic collisions with ground atoms, there exists a simple relationship between line emission and ionization rate which is only weakly

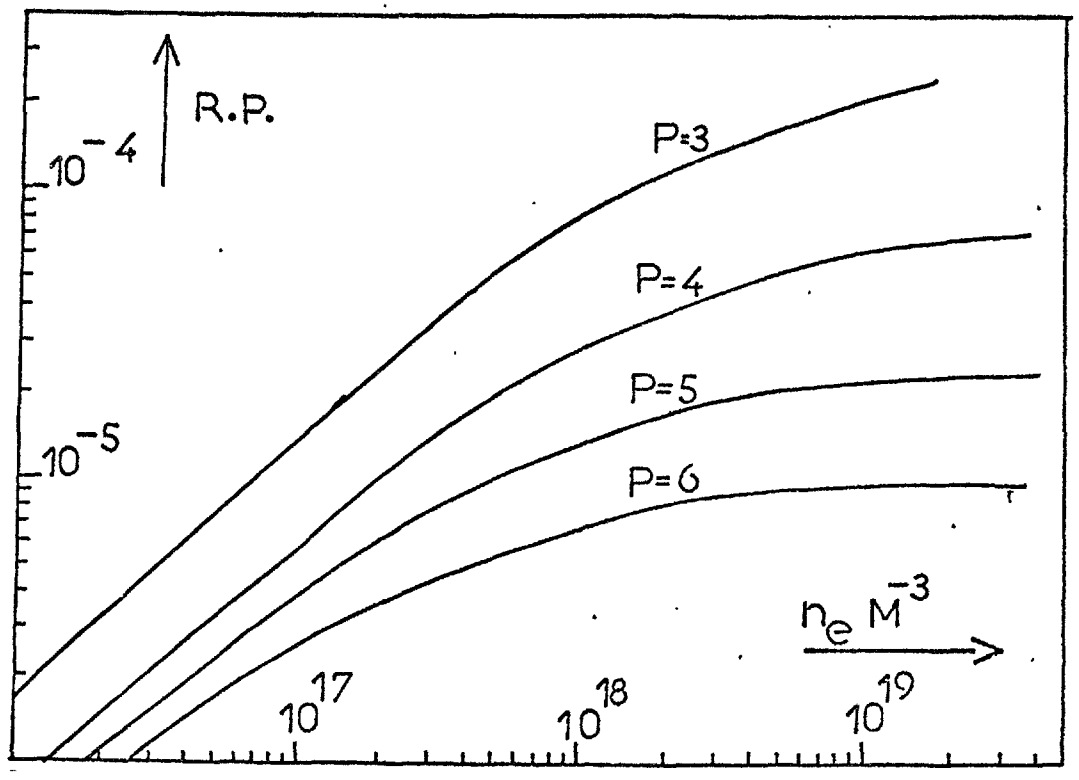

Fig.4.1

Relative hydrogen state populations $n(p)/n(1)$ at $T_e = 3$ eV
p indexes the principal quantum number of state

dependent upon n_e and T_e (Johnson and Hinnov, 1973). Using the second term of equation (4.1) to substitute the ionization rate of section 2.1, we obtain:

$$\frac{dn_e}{dt} = n_e NS \simeq n_e n(1) S = \frac{n_e S}{r_1(p)\, p^2 \exp \frac{E_I}{kt}\left(\frac{1}{p^2} - 1\right)} n(p)$$

$$= \eta\left(n_e, T_e\right) n(p) \ .$$

The strong exponential in S cancels, so that the n_e and T_e dependence of η arises from $n_e/r_1(p)$. For transitions optically thin to Lyman, η is almost constant over a wide range of n_e and T_e. For the case of plasma optically thick to Lyman radiation the situation is less ideal, and η, as shown in Fig.4.2, has some temperature and density dependence. However, if n_e and T_e are approximately known, the ionization rate can be determined fairly accurately from the absolute value of the line emission.

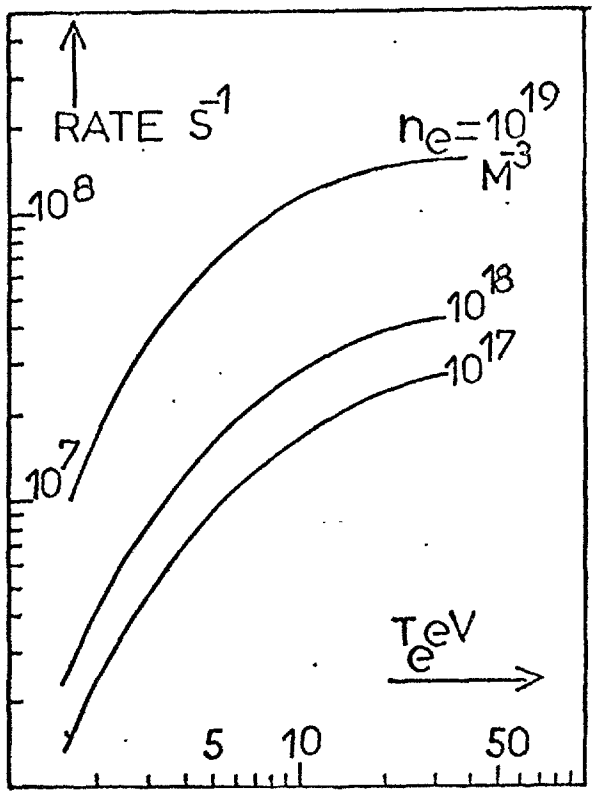

Fig.4.2
Ionization rate per unit excited state ($p=3$) population, i.e. $R = \frac{n N S}{n(3)}\ s^{-1}$

To summarise, if T_e is approximately known, n_e may be determined from relative Balmer intensities, and both neutral density and ionization rate can be obtained from the absolute value of these intensities.

4.2 CALIBRATION OF THE DETECTING SYSTEM

The plasma was viewed through the radial ports using the same detecting system as described in Chapter II for the line profile measurements — namely a reflection grating spectrometer and a photomultiplier. Balmer lines α, β, γ, and δ were observed. Fig.4.1 shows that $n(3)/n(6)$ may be as large as 20, and the ratio of transition probabilities for the two lines is ~ 40, so that an intensity ratio ~ 800 may be expected. This range would stretch from the saturation limit ~ 1 V to the noise limit ~ 1 mV on the photomultiplier, were it not for the fortuitous fall-off in red sensitivity due to the photocathode quantum efficiency. Nevertheless the requirement of linearity is still severe. Relative and absolute

calibrations were performed with the aid of a standard tungsten ribbon filament lamp. However, initial calibration and linearity measurement seemed to suggest that there was considerable deviation from linearity at small signals, and that, moreover, the deviation was wavelength dependent. The linearity of the photomultiplier alone was checked by means of a pulsed LED and the inverse square law and found to be within 5% over $2\frac{1}{2}$ decades. The only serious non-linearity in fact occurred, as expected, at high output near saturation.

The method of calibration was also scrutinised. The brightness temperature of the filament was checked by means of an optical pyrometer and also by comparison with other standard bulbs, but no significant discrepancy was found. Changes in the wavelength dependence of filament emissivity due to ageing is possible, but the discrepancy would have to be $\sim 100\%$ or greater.

Finally, a poor spectrometer/grating rejection was found to be responsible for the erroneous calibration at small signal levels. Rejection, defined as the ratio of observed wing intensity to peak intensity for a narrow band source, was found to be 1 in 5000 for a 10 Å bandwidth instrument. For a 10 Å bandwidth, the ratio of collected violet emission to total emission in the spectrometer range may be as low as 1 in 10^5 at low filament temperatures. In such a case there will be 20 times more unrejected red light than violet collected at the photomultiplier. The rejection of the spectrometer was improved by filtering the filament emission with a broad band blue filter of OB10 glass. The transmission of this filter was measured using line sources where there could be no effects due to rejection. This reduced the red overspill into the violet by a factor 1000, and gave a calibration indicating uniform sensitivity right down to the smallest detectable signals. The accuracy of the calibration

is then limited by measurement of the filament temperature, but a calibration reliable to an estimated 20% could be obtained for various visible wavelengths.

4.3 THE MEASUREMENTS AND RESULTS

A complete axial scan of the four visible Balmer lines and their underlying continua was taken both in the accelerated plasma and the exhaust. A correction was made for wall opacity, though, through use of a shorter bank pulse ($\sim$ 2 ms), this was only small and fairly constant over the number of shots required. The continuum under each line was found by scanning on either side of the line and interpolating. Fortunately there were no close impurity lines to upset this measurement. For the case of the exhaust the collection region was defined by means of a lens and slit, but for the accelerating plasma, where access was poor, a fibre bundle was used. In this latter case, the plasma volume observed was defined by the aperture of the hole through the magnets. These differences were taken account of in the calibration.

Bates et al. (Bates, Kingston and McWhirter, 1962) state criteria for the leading members of the Lyman and Balmer series of hydrogen to be optically thin:

$$\begin{aligned} \text{Path length} \quad L &\ll 1.6\times10^{17}\ T_a^{\frac{1}{2}}/n(1)\ \text{m} \quad \text{for Lyman } \alpha \\ L &\ll 2.0\times10^{16}\ T_a^{\frac{1}{2}}/n(2)\ \text{m} \quad \text{for Balmer } \alpha \end{aligned} \qquad \ldots (4.4)$$

where T_a is the atom temperature in eV. For the Doppler temperatures of Chapter II, and plasma path lengths $L \simeq 2.5$ cm, we require $n(1) \leqslant 6\times10^{18}\ \text{m}^{-3}$ and $n(2) \leqslant 8\times10^{17}$ for both lines to be thin. Thus, for filling densities

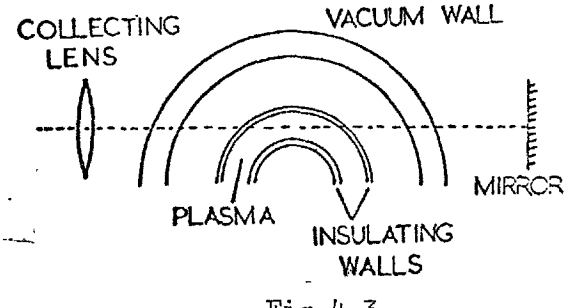

Fig.4.3
Path in plasma to check optical opacity, showing wall reflection-absorbtion problem

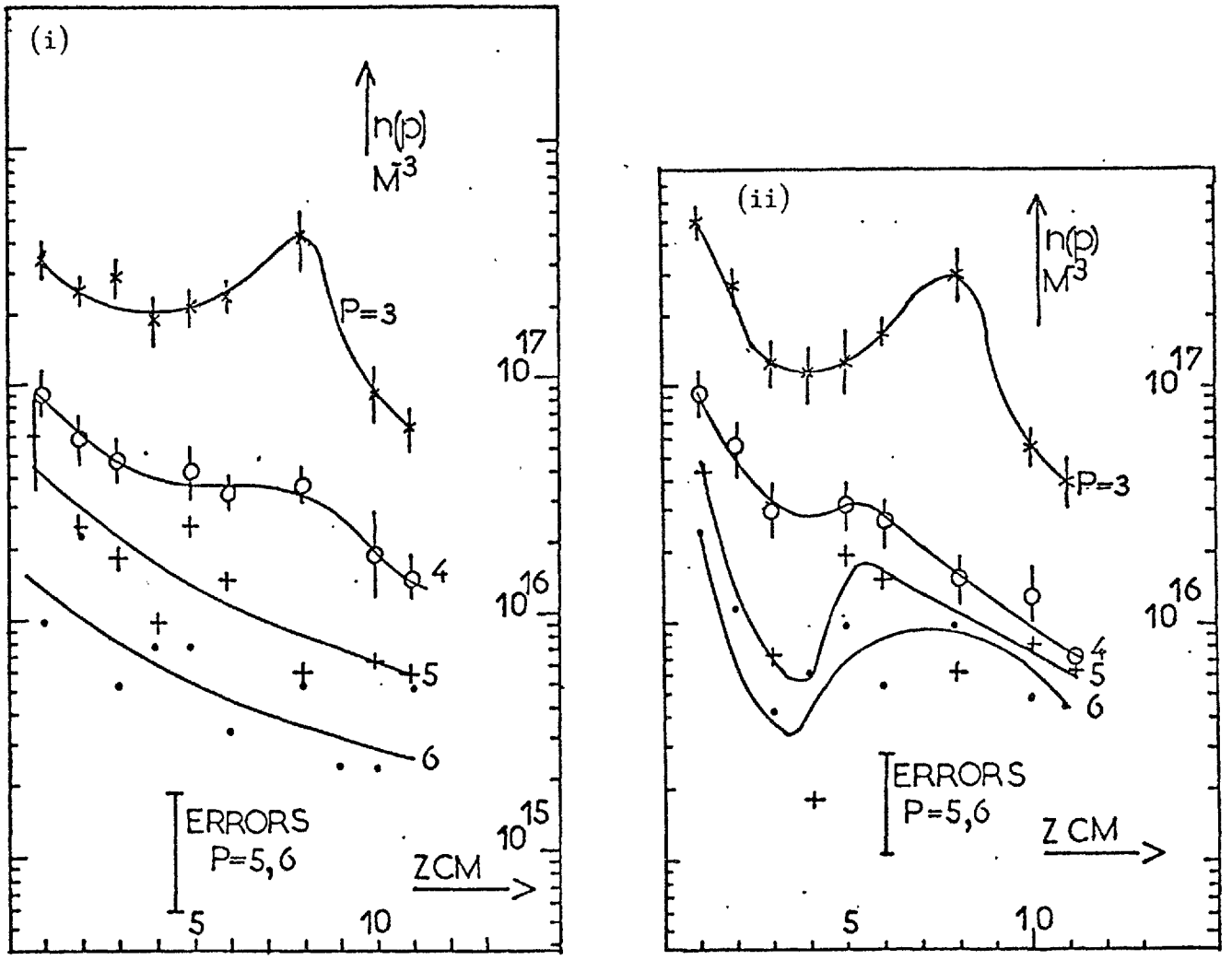

Fig.4.4
H state populations as a function of distance z from anode at (i) 100 μs and (ii) 500 μs. The cathode lies at z = 13 cm

$\sim 3\times10^{21}$ m^{-3}, it is reasonable to expect that the plasma should be thick to Lyman radiation. Balmer α was verified to be thin experimentally, using the optical arrangement of Fig.4.3, comparing single and double plasma paths. When due allowance is made for wall reflection and absorption losses in the glass walls, it was found that the optical depth D $\geqslant$ path length L.

The observed line intensities, measured as a function of axial position, can then be interpreted in terms of the state population densities shown in Fig.4.4 at 100 μs and 500 μs, assuming radial uniformity. Whilst the populations at the earlier time are fairly smooth functions of position, those at the later time are strongly peaked at the beginning of each stage. The larger error bars for the higher lines arise because of the strong continuum at these wavelengths, and because of a poor signal-to-noise ratio consequent upon the small signals.

4.4 INTERPRETATION IN TERMS OF NEUTRAL AND ELECTRON DENSITY

Initially, attempts were made to try and obtain both T_e and n_e by fitting the results to the data of Johnson and Hinnov. However the spread in temperature and density for a reasonable fit were rather too large to be useful. However, after the temperature estimates from Chapter III were obtained, graphs of the relative population as a function of n_e could be drawn out for particular values of T_e, so that the fit of experiment to data was, at the same time, simpler and more accurate.

Figure 4.5 demonstrates the results obtained by such a process, showing axially resolved electron and neutral densities at the peak of the line emission at 500 μs. The values of neutral density obtained vindicate the assumption of optical thickness to Lyman radiation and justify the use of the appropriate data. Notice the estimates of electron densities are within the upper limit set by earlier null estimates of Stark breadth.

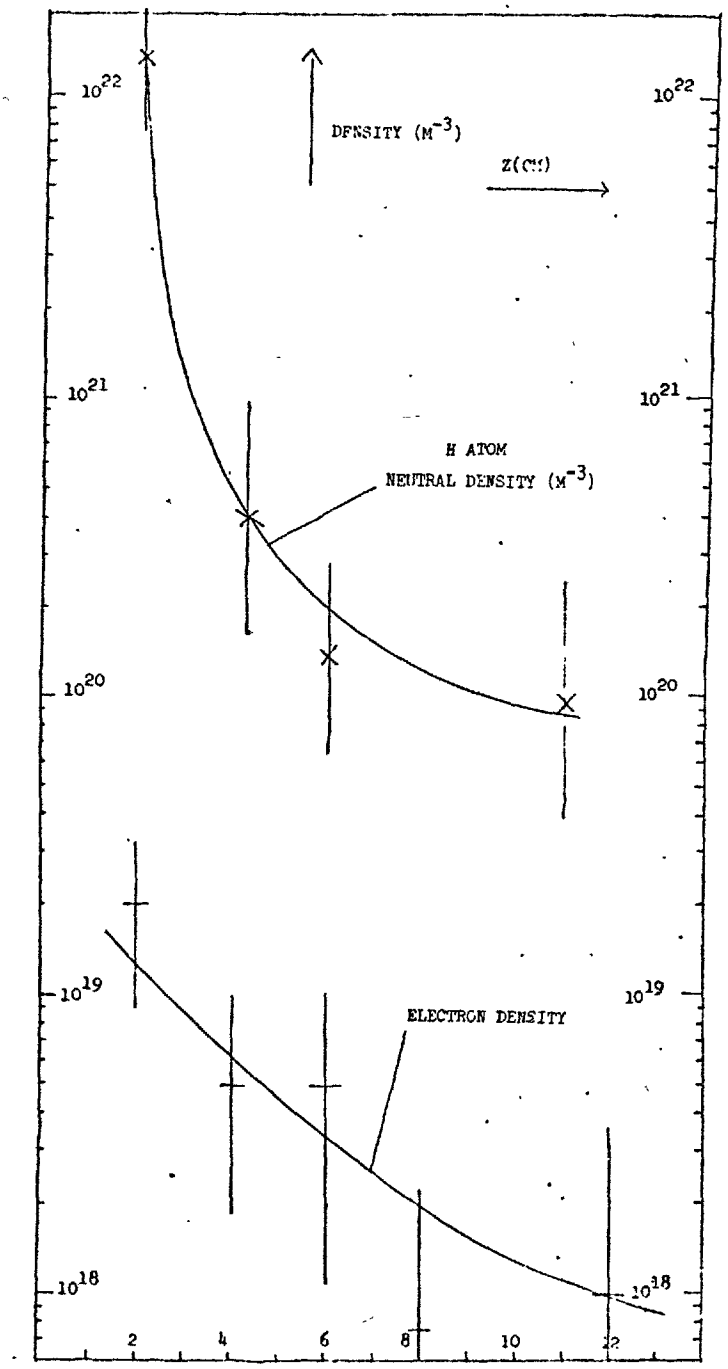

Fig.4.5

Neutral H atom and electron densities as a function of distance from anode (Z), i.e. inside accelerator, at 500 μs

For clarity we shall postpose discussion of these results until a separate section.

During the spoke phase, the peak intensities can be analysed in a similar manner to give a fairly uniform electron density in the range 5×10^{18} to 2×10^{19} m^{-3}. This is a rather insensitive method, since the electron density is high. Close to the anode, where $T_e = 2.5 \pm 5\,eV$, $N \sim 2\times10^{21}$ to within a factor 2, which is comparable to the 100 mT filling pressure. In stage two however, where T_e is lower $\sim 1.5\,eV$ (Fig.3.18) the dependence of $n(1)$ upon T_e is so sensitive that it is only possible to estimate $N \sim 10^{22}$ to within an order of magnitude. Despite the poor accuracy, the result does suggest that there is no substantial depletion of second stage neutrals at this time.

In the exhaust plasma, the plasma is optically thin to the Lyman lines, and analysis gives the densities of Fig.4.6 as a function of distance from the cathode. The values of n_e agree with microwave interferometric measurements made only in the exhaust (Cole - unpublished results). Note that the spectroscopic measurements inside the accelerator indicate an increase in n_e of an order of magnitude, and a fall in N of 2 orders of magnitude across the cathode. Though the fall in n_e further from the cathode is consistent with the beam divergence, this would suggest that the plasma is localised to the cathode aperture diameter close to the cathode, whereas in fact both line emission and T_e are uniform across the tank. The decrease in density must be recombination. The increase in electron density across the cathode is caused by full ionization of the neutral gas in the exhaust tank. Ionization is not balanced by acceleration out of the region, as is the case inside the accelerator. As a result the electron density accumulates, thereby increasing the ionization rate so that full ionization might be reached.

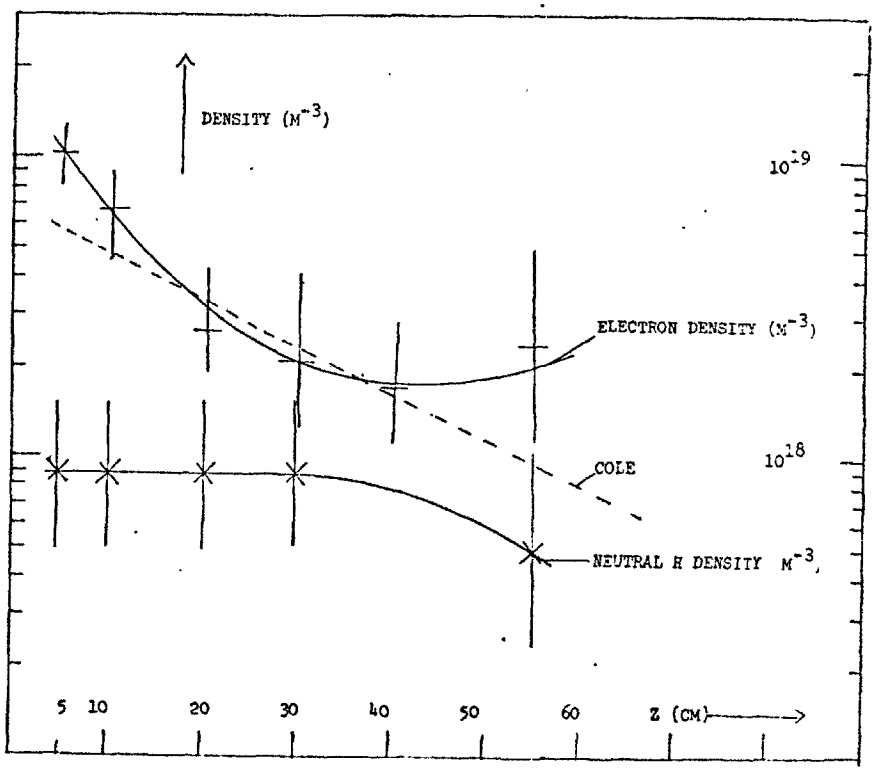

Fig.4.6
Neutral and electron densities (N and n_e m^{-3}) as a function of distance z from cathode, at 500 μs

4.5 THE VALUE OF $\omega\tau$ AT 500 μs

The values of $\omega\tau$, including contributions from both electron-ion and electron-neutral collisions, can be calculated from the experimentally determined n_e, T_e, N, and are shown in Fig.4.7. The accuracy is limited to a factor ~2 by the density determination. In the first stage, $\omega\tau$ lies in the range 20-200, but in the second, where both electron and neutral densities are lower, $\omega\tau$ reaches ~2000. The simple theory of section 1.2 suggests that such a high value of $\omega\tau$ should lead to efficient plasma acceleration. The electron current impedance J_{ze}/E_z allows an estimate to be made of $\omega\tau$ assuming the electron conduction is collisional and given by (1.4), i.e.

$$(\omega\tau) = \left(\frac{\sigma E_z}{J_{ze}} - 1\right)^{\frac{1}{2}}$$

and this is shown also in Fig.4.7 labelled EFFective. The large discrepancy (~ 100) suggests that the dominant mechanism for electron conduction

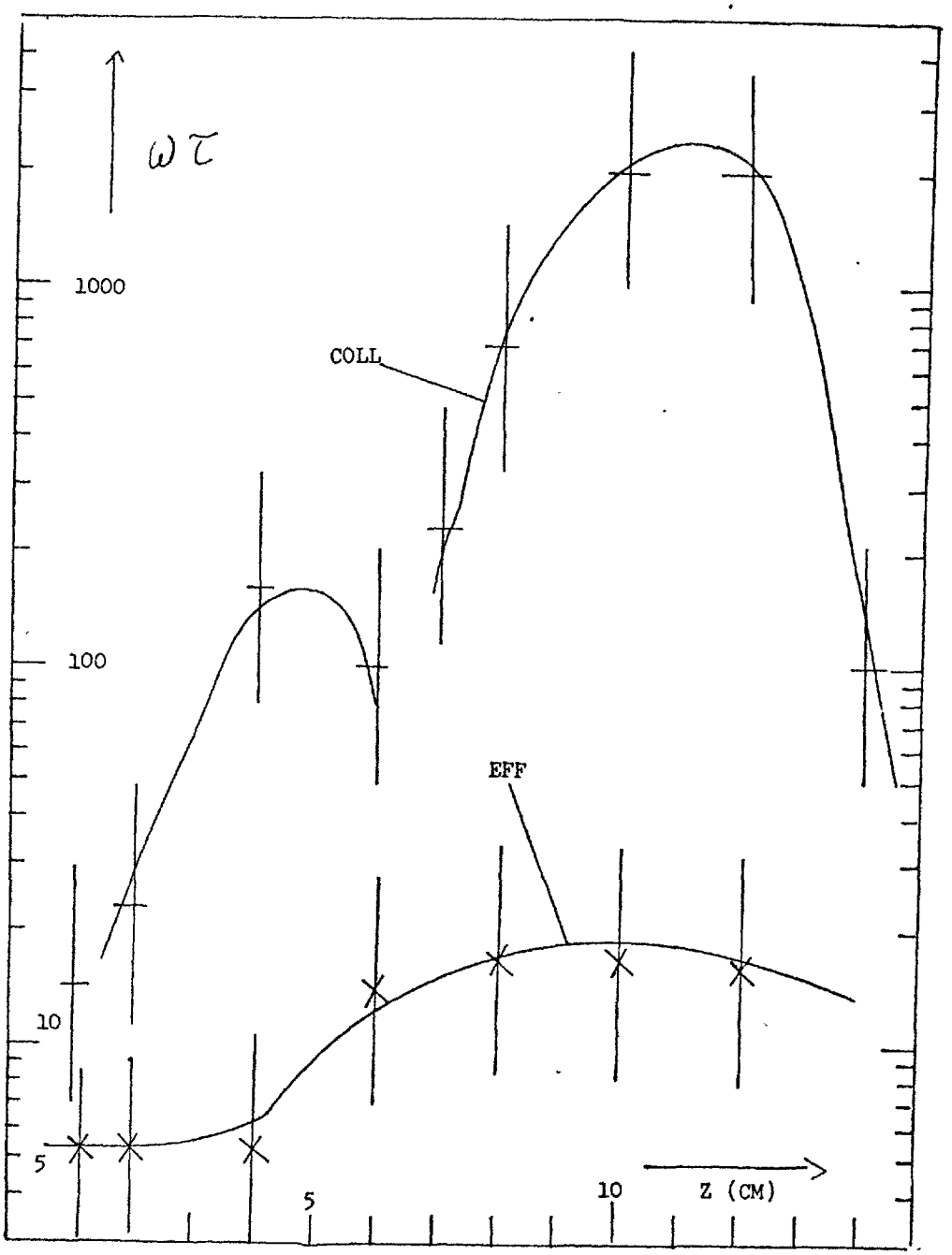

Fig.4.7

The Hall parameter $\omega\tau$, as a function of distance z from anode at time 500μs. The curve labelled COLL is calculated from n_e, T_e, N. EFF is the value obtained from effective electron current conductivity

across B in the direction of the applied $\underline{E}$ is not given by the simple collisional result. The measured electron current j_{ez} and the expected collisional value $\sigma E_z / 1 + (\omega\tau)^2$ are compared in Table 4.1, showing that the latter underestimates the current by a factor between 10 and 1000.

Also shown in Table 4.1 is the electron-ion collisional mean free path $\lambda_{ei} \simeq 10^{16}\ T_e^2 / n_e m$ (where T_e is in eV). Although $\lambda_{ei} \sim$ mm in the first stage, the steep dependence upon T_e leads to the conclusion that in the second stage, where T_e is high (~ 6 eV) and n_e is low ($\sim 10^{18}\ m^{-3}$), λ_{ei} can be larger than the radial distance to the wall. Thus here an electron is more likely to impact the wall sheath region before the long range Coulomb interaction produces a 'collision'. Table 4.1 shows the ratio, ν_w/ν_{ei}, of wall collision frequency to Coulomb collision frequency reaches ~ 20 in the second stage, but that $\omega\tau_w$ (where τ_w is the time for a thermal electron to reach the wall) is still large. Hence this does not alter the conclusion that effects other then electronic collisions dominate the conductivity at these times.

The theory of Rosa (Rosa, 1962) demonstrates that plasma non-uniformities can sharply increase the transverse electron conductivity towards the field-free value. This arises because the inhomogeneity permits the existence of an electric field perpendicular to both the magnetic field and the applied electric field, and this gives rise to an $\underline{E} \wedge \underline{B}$ driven electron current in the direction of the applied electric field. This driven current increases the effective conductivity above the collisional value.

A fluctuating azimuthal electric field of amplitude $\sim 2 \times 10^4$ V/m and period ~ 5 mc/s is observed with the double electric field probe of section 3.8. This would drive an axial $E_\theta \wedge B_r$ current of $\sim 10^5$ A/m^2 if in phase with the density fluctuation, thus dominating the axial current. Such fluctuations would seem to be the key to the non-collisional conduction current.

Z cm	j_{ez} A/m^2	E_z V/m	Conduction current for B = 0 σE_z A/m^2	Cross-field current $\sigma E_z/1+(\omega\tau)^2$ A/m^2	Electron-ion mean free path λ_{ei}	$\omega\tau_{wall}$	Ratio of wall and Coulomb collision frequencies ν_{wall}/ν_{ei}
2	$1.8\pm0.2\times10^5$	$8\pm2\times10^3$	$6\pm2\times10^6$	1.1×10^4	1 mm	900	0.005
4	$1.8\pm0.2\times10^5$	$3\pm1\times10^3$	$6\pm2\times10^6$	2.2×10^2	9 mm	500	0.5
6	$1.8\pm0.2\times10^5$	$6\pm2\times10^3$	$4\pm2\times10^6$	2.6×10^3	7 cm	60	3.0
8	$1.7\pm0.2\times10^5$	$1.4\pm0.2\times10^4$	$6\pm1\times10^6$	1.3×10^2	27 cm	200	13.0
10	$1.6\pm0.2\times10^5$	$1.4\pm0.2\times10^4$	$6\pm1\times10^6$	1.5×10^1	32 cm	400	15.0
12	$1.4\pm0.2\times10^5$	$1.4\pm0.2\times10^4$	$5\pm1\times10^6$	1.2×10^1	40 cm	400	18.0
				Accurate to a factor ~4	Accurate to a factor ~2	To factor 50%	To factor ~2

Table 4.1

Comparison of measured and collisional electron currents at 500 μs at various distances z from anode. Also listed are the electron-ion mean free path, the value of $\omega\tau_{wall}$ and the relative importance of Coulomb and wall collisions

4.6 THE PARTICLE BALANCE AT TIME 500 μs

The experimental measurements on densities, ion fluxes, neutral Doppler profiles etc. allow rough estimates to be made of particle, momentum and energy balance.

The 0.3 cm^3 of the gas valve charged with H_2 at 1 atm. is discharged in ~ 500 μs. Hence the mean inflow of molecules is given by a flux:

$$F_{IN}^{H_2} = 3 \pm 1 \times 10^{24} \text{ molecules/m}^2\text{/s} .$$

The accelerated ion flux at the cathode is, from section 3.5:

$$F_{OUT}^{ION} = 3 \pm 1 \times 10^{23} \text{ ions/m}^2\text{/s} .$$

Since the Balmer emission is given by the second term of equation (4.1), the Doppler profiles of section 2.6 are effectively atomic velocity distributions averaged over the line-of-sight. Numerical integration of such a profile gives the H atom flux at the cathode:

$$F_{OUT}^{H} = 3 \times 10^{24} \text{ atoms/m}^2\text{/s.}$$

accurate to a factor 2 limited by the atomic neutral density estimate. These fluxes balance within this limit, so that the flux of molecular neutrals cannot be significantly greater than F_{OUT}^{H}.

4.7 THE MOMENTUM BALANCE

It is possible, using the probe estimate of ion flux (nQ ev) and the measurement of n_e, to evaluate a spatially resolved mean ion velocity to within a factor 2. Assuming singly charged ions, this gives a velocity $\sim 4 \times 10^5$ m/s at the cathode. This must give an ion energy less than the anode cathode voltage drop, which puts a limit on $\frac{A}{Q^3} \sim 2 \begin{smallmatrix} +2 \\ -1 \end{smallmatrix}$, where A is the mass number and Q the charge number of the ion. For low T_e, $Q \sim 1$ for impurities, so that this is effectively a limit on A, implying no great contribution from impurity ions. Fig.4.8 displays the mean ion energy for H_2^+ or H^+ ions, compared to plasma voltage drops. The

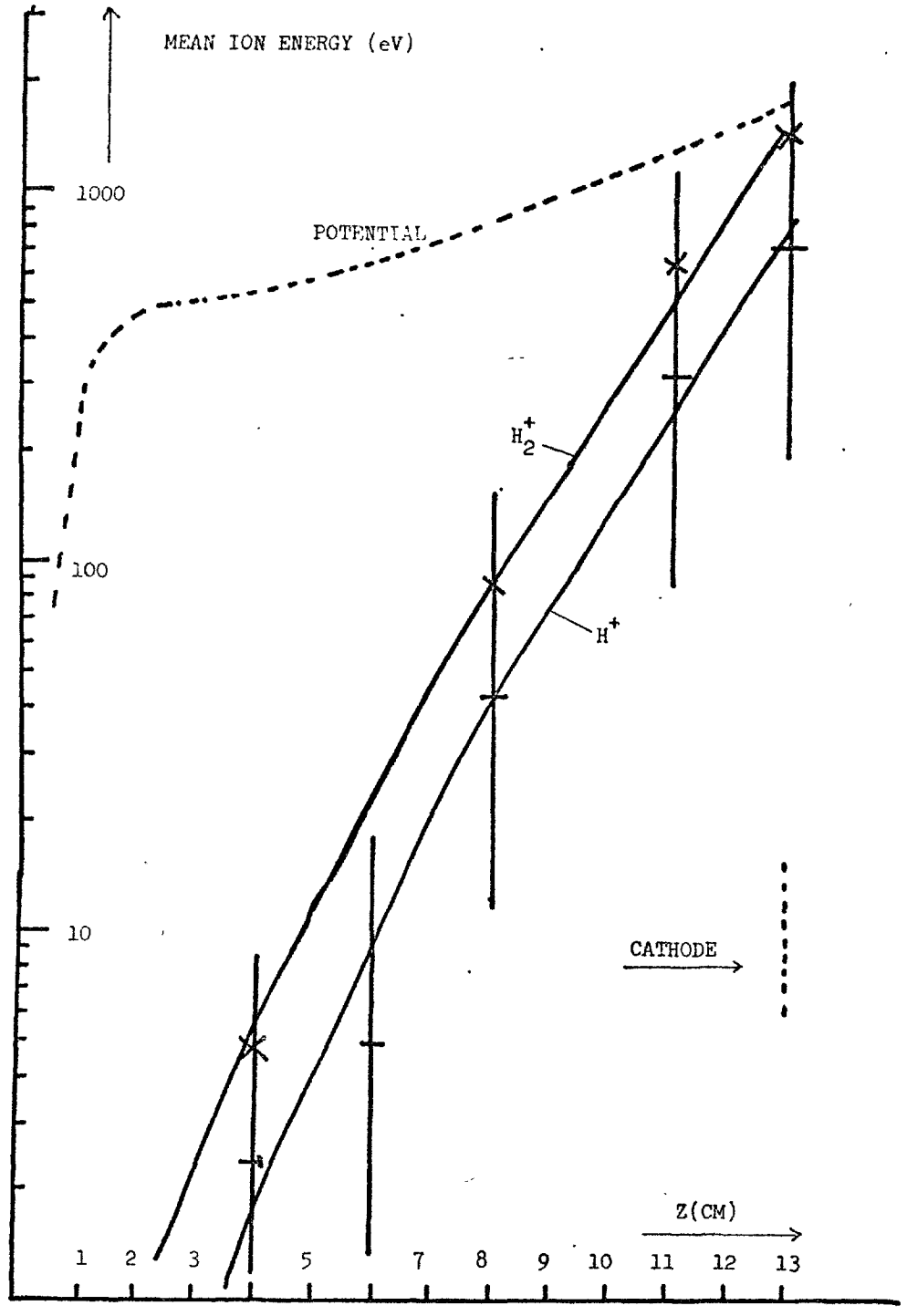

Fig.4.8

The mean ion energy against distance (Z) from anode, and evaluated from ion flux values, assuming H^+ and H_2^+ ions in turn. The plasma potential is also shown for comparison

second stage ions have energies comparable to that acquired by free acceleration in the electric field from the region 6 to 8 cm from the anode — i.e. from between the stages. Close to the anode, where charge exchange mean free paths are ~0.1 to 1 mm, the low ion energies ~few eV are to be expected, but later in the first stage, where mean free paths should be ~1 cm, the expected 50–100 eV energies are not seen.

The momentum balance can be examined using these values of ion velocities, the neutral Doppler profile, and the Hall current measurement of section 3.7. The correction factors ϵ and η have been used to allow for the large uncertainty in n_e and N, i,e. we have taken $n_e = \epsilon * n_e$ (measured) and $N = \eta * N$ (measured), where ϵ and η lie in the range 0.5 to 2. We obtain (at the cathode) at 500 μs:

Neutral atom momentum flux density = 880 η kgm/m/s^2

Ion momentum flux density (assuming H_2^+) = 400/ϵ kgm/m/s^2

Hall current momentum input = $J_\theta B L$ = 2500 ± 500 kgm/m/s^2

where L is the stage length over which the Hall current flows. Good balance can be obtained for $\eta = 2$. The balance is not sufficiently accurate to reveal a contribution from either molecular neutrals or wall impact.

4.8 THE IONIZATION

Both atomic and molecular ionization should be considered here. Electron impact upon incoming molecules will produce both ionization and dissociation:

$$H_2 + e \rightarrow H_2^* + e \rightarrow e + H + H$$

$$H_2 + e \rightarrow H_2^+ + 2e .$$

The thresholds for these processes occur at electron energies 8.8 eV and 15.6 eV. Hence the rate for the former is $e^{6.8/T_e}$ greater for electrons of temperature T_e. The dissociative recombination process (Massey, 1951) can be important:

$$H_2^+ + e \rightarrow H_2^{**} \rightarrow H_2^{***} \rightarrow H + H$$

where the excited molecular state H_2^{**} overlaps with the repulsive state H_2^{***}. Massey gives a large recombination coefficient, $\alpha \simeq 2 \times 10^{-13}/T^{\frac{1}{2}} m^3 s^{-1}$, for this process. The atoms formed by either dissociative process will then be ionized by electron impact.

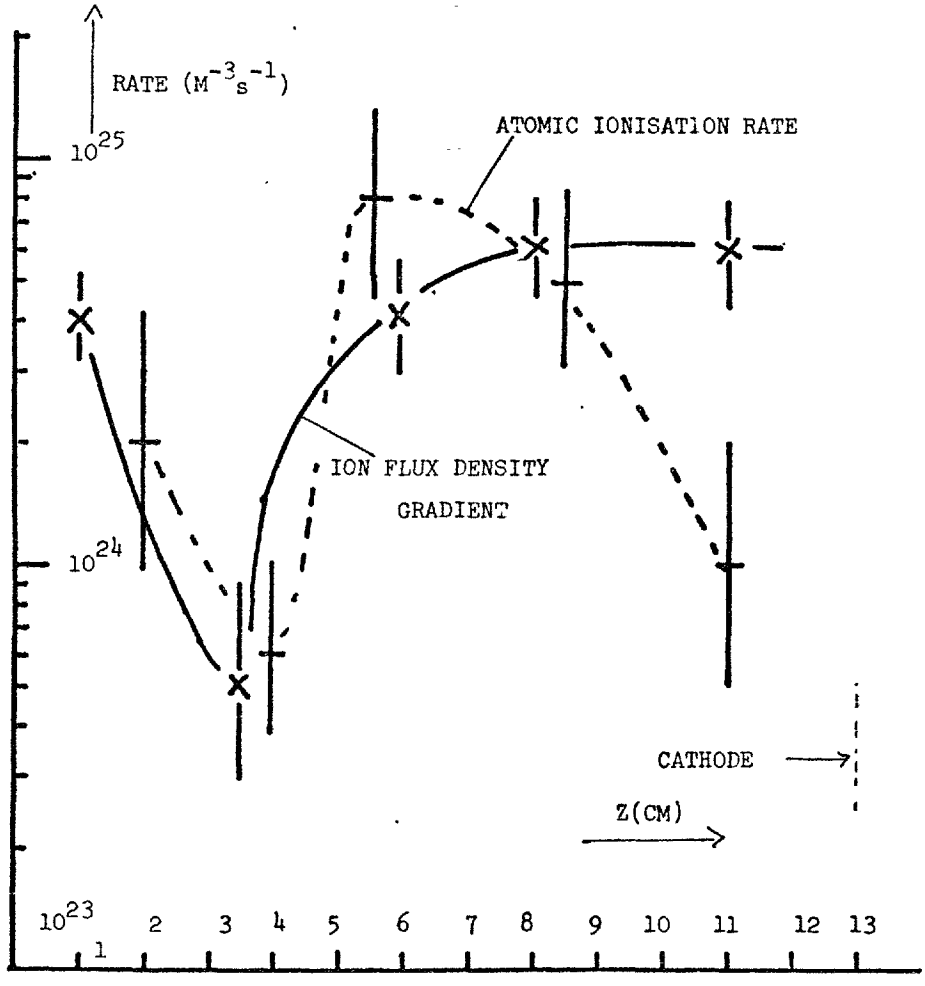

Fig.4.9
A comparison of the spatially resolved H atom ionization rate with the growth of ion flux

Figure 4.9 shows the spectroscopically determined ionization rate $R = n_e N S$ for atoms. For comparable neutral atom and molecule densities, the rate for molecular ionization will be similar because cross-sections and ionization potentials are similar (Oak Ridge Tables). However, whereas for atomic ions the radiative recombination rate

$$R = n_e^2 \frac{2.7\times10^{-19}}{T_e^{\frac{3}{4}}} \; m^{-3}\; s^{-1}$$

(Hinnov-Hirschberg, 1962) is only 10^{20} m^{-3} s^{-1} for $n_e \sim 2\times10^{19}$ $T_e = 1$ eV, the dissociative recombination rate $R \sim 8\times10^{24}$ is large compared to ionization. This would suggest that there will be few molecular ions near the anode.

Also on Fig.4.9 is the axial gradient of ion flux. This is found to balance the atomic ionization rate ($\frac{d}{dz} nV_z \simeq nNS$) suggesting that H_2^+ ions contribute no more than ~half of the ion flux.

The plateau in ion current coincides with the dip in ionization, suggesting that this is due to the low T_e and n_e there. The ionization rate is large between the stages because of the high temperature, and falls in the second stage because of low density. The peak in ionization rate corresponds to the ion creation region suggested in the previous section on the basis of ion energy.

4.9 THE ELECTRON ENERGY BALANCE

Here, we deal first with the electron energy balance of equation (2.3). The electron-heavy particle collision cooling becomes heating if account is taken of the thermal like spread of ion energy (Cole, 1970). A Spitzer equipartition between electrons of temperature T_e and ions of energy spread W gives an electron heating rate $H = (2\times10^{-35})(W - T_e)\, n_e^2$ watts/m^3. The ionization energy loss uses the ionization rate of Fig.4.9. Thermal conduction loss to the walls is taken to be characterised by a radial temperature scale-length $L = 1$ cm, half the channel width. Thus all the terms of the electron energy balance are estimated and tabulated for various distances, z, from the anode, in Table 4.2.

Z (cm)	j_{ez}^2/σ Watt / M^3	$j_{\theta e}^2/\sigma$ Watt / M^3	$j_{ez}\,E_z$ Watt / M^3	Thermal Conduction loss. W/m^3	Ionization Energy W/m^3	Neutral Cooling W/m^3	Ion Heating W/m^3	Flux Limited Conduction Loss. W/m^3	Wall Dominated Ohmic input. W/m^3
2	4.5×10^7	$\leqslant 4\times10^5$	1.4×10^9	3×10^6	4×10^6	2×10^6	$\leqslant 10^3$	-	-
4	1.7×10^7	$\leqslant 4\times10^5$	5.4×10^8	2×10^7	1×10^6	7×10^4	$\leqslant 10^3$	-	-
6	5.1×10^6	$\leqslant 4\times10^5$	1.1×10^9	6×10^8	2×10^7	5×10^4	$\leqslant 10^3$	2×10^8	6×10^7
8	6.4×10^6	2×10^7	2.4×10^9	8×10^8	8×10^6	1×10^4	6×10^3	8×10^7	2×10^8
10	6.1×10^6	2×10^7	2.2×10^9	7×10^8	4×10^6	5×10^3	3×10^4	5×10^7	3×10^8
12	5.6×10^6	2×10^7	2.0×10^9	2×10^8	2×10^6	2×10^3	2×10^4	1×10^7	4×10^8
Accuracy	50%	50%	~ 20%	factor ~ 2	factor ~ 2	factor ~ 4	factor ~ 4	factor ~ 3	factor ~ 2

Table 4.2

The electron energy balance. Columns 2-8 compare energy input and loss estimated on a basis of electron-ion and electron-neutral collisions. Column 9 gives the flux limited thermal conduction loss for the second stage where $\lambda_{ie} \geqslant L$. Column 10 gives the 'worst' estimate of the contribution of wall collisions to the Ohmic heating.

The discrepancy between the Ohmic heating j^2/σ and the value of $j_{ez} \cdot E_z$, which should be equal in the high $\omega\tau$ limit, is to be expected since Table 4.1 has already shown that $j_z = \sigma E_z / 1 + (\omega\tau)^2$ does not hold. This arises since, due to the fast fluctuations $\bar{j}_{ez} \cdot \bar{E}_z$ and $\overline{j_{ez} \cdot E_z}$ are not necessarily equivalent, suggesting that electron current fluctuations are in anti-phase with the electric field fluctuations. The dominant electron energy loss mechanisms are thermal conduction and ionization in the first stage, giving a balance within the uncertainties in estimation. However, in the second stage the balance is not good. If the long electron collisional mean free path in the second stage is taken into account, the electron thermal conduction loss becomes limited to that set by the electron thermal flux to the wall, i.e. a heat flux

$$F = \frac{n\bar{v}_r}{2}\left(\frac{3}{2} eT\right) \text{ watts/m}^2 .$$

The flux limited conduction loss is shown in column 9 of Table 4.2, which balances fairly well the Ohmic heating due to the Hall current. It is difficult to estimate how serious an effect wall impact and reflection of electrons might have on the Ohmic heating, but an upper limit can be taken by replacing the electron-heavy particle collision frequency with the electron-wall collision frequency in the expression $\sigma = ne^2/m\nu$ for conductivity. The Ohmic heating derived in this way is shown in the last column of Table 4.2, with values much larger than the flux limited thermal loss, suggesting that wall collisions do not have a serious effect on the Ohmic heating. Thus electron-heavy particle collision dominated Ohmic heating appears to balance flux limited thermal conduction in the second stage.

4.10 THE TOTAL ENERGY BALANCE

The total energy balance can be considered using the values of heavy particle fluxes already obtained. Again the error factors ϵ and η are used to take account of the uncertainty in n_e and N. The energy partition at 500 μs is illustrated in Table 4.3.

	Mechanism	Value
(i)	Total power input	1500 ± 200 kW
(ii)	Ion power output in exhaust	$200/\epsilon^2$ kW
(iii)	Neutral power output in exhaust (H atoms)	$400\ \eta$kW
(iv)	H atom power to wall from thermal impact	$200\ \eta$ kW
(v)	Flux limited electron thermal loss	$40\ \epsilon$ kW
(vi)	Total power output (to within a factor 2)	900 kW
(vii)	Power input to ions from E_z	270 ± 30 kW
(viii)	Total input to heavy particles from second stage Hall current	300–600 kW
(ix)	Power transfer from ions to neutrals by charge exchange	$100\ \eta/\epsilon^2$

Table 4.3

The Total Energy Balance

The sum of the energy losses (ii) (iii) (iv) and (v) balances the input energy (i) to within the accuracy of the measurements. Thus it is not possible to reveal any energy loss from wall impact of ions, though this could be substantial. The ratio of (ii) to (i), i.e. the ion beam efficiency is 0.18 ± 0.02, agreeing with Cole's calorimetric measurements of output (Cole, 1970). Such agreement is only to be expected if the large neutral directed energy (iii) is not seen by the calorimeter. This is plausible if the neutrals have a large angular spread of velocities.

There is a discrepancy between the energy acquired by ion free-streaming along E, $\int I_{iz} E_z \, dz$ - (vii) and the energy input from the Hall current, $A \int v \cdot (\underline{j}_\theta \wedge \underline{B}_r) \, dz$ - (viii), which should be identical on the simple theory of Chapter I. This arises because the measured Hall current density $j_\theta \sim 3.5 \pm 0.5 \times 10^5$ A/m^2 is greater than the azimuthal $E_z \wedge B_r$ drift current estimated at $7 \pm 2 \times 10^4$ A/m^2, whereas it is the

equality between these (equation (1.4) which leads to the picture of free ion acceleration under $\underline{E}$. Presumably this is resolved if account is taken of the phase relationships between quantities determined by the fast fluctuations.

4.11 SUMMARY OF THIS CHAPTERS WORK

This chapter brings together the experimental results of the previous two chapters, and obtains, spectroscopically, estimates of electron and neutral densities, thereby filling a large gap in the literature on Hall accelerators. It should be pointed out that Russian work on spectroscopic diagnosis of a low current density Hall accelerator has become available (Abramov, 1974) since the work presented in this chapter was completed. However this Russian work has not made absolute estimates of n_e or N.

In this chapter however, one of the original aims of the work has been achieved, namely a direct estimate of the Hall parameter $\omega\tau$ from plasma conditions. This is found to be very large, varying from 20 to 2000. It is shown, however, that this does not produce the expected good plasma acceleration, and that the electron conductivity parallel to E_z is characteristic of a much smaller $\omega\tau$ ($\omega\tau_{EFF}$ from 5 to 20). In addition the Hall current appears to be larger than the high $\omega\tau$ limit of equation (1.4). The fast electric field fluctuations can account for the enhanced conductivity.

The estimates obtained for plasma parameters are used to discuss the particle, momentum and energy balance during the main discharge phase. It is confirmed that free acceleration of ions under $\underline{E}$ is not valid close to the anode since the charge exchange mean free path is too small. However significant acceleration occurs in the second stage and large ion velocities are deduced here.

The electron energy balance is dominated by Ohmic heating, thermal conduction loss and ionization. However, in the second stage, the long electron-heavy particle collision mean free path is important, reducing the conduction loss. In consequence, the electrons appear to contribute only a small fraction to the total energy balance. Here the energy acquired by neutrals is surprisingly large. The previously determined beam efficiencies of $\sim 20\%$, suggest that this neutral energy is dispersed and not seen in the beam exhaust. An accurate energy balance would need account to be taken of the phase relationships dictated by the instabilities.

CHAPTER V

TREATMENT OF ACCELERATION IN ONE SPACE DIMENSION

5.1 INTRODUCTION

There are several approaches to Hall acceleration, (Haines, 1961; Dunnet, 1968, Kilkenny, 1972), in which the simple local treatment of Chapter I has been extended to try and deal with real experiments. These workers have had the Polytron accelerator in mind, where since each cusp stage is identical, the axial variation has been eliminated by some assumption such as incompressibility, and the time dependence then examined. By contrast, in a linear Hall accelerator, incompressibility is invalid because ionization allows an axial variation in ion flux. Moreover, practical long pulse applications focus interest on steady state behaviour, so long as transient times are short ($\sim$ 1-100 μs, say). The aims of the work presented in this chapter are threefold, to account for the experimental observations already presented, to probe those features which seem to require an account to be taken of non-uniformities, and to find the limitations of such an approach.

5.2 THE DEPLETION OF NEUTRAL DENSITY

The neutral density is an important quantity in that at low degrees of ionization, and low electron temperatures it will dominate both electronic and ionic collisions. The former is not important, since typical filling pressures of $\sim$ 100 mT give a large $\omega\tau$ of $\sim$ 250 at $T_e \sim 1$ eV and B $\sim$ 1 kg. However, at energies $\leqslant$ 1 keV, charge exchange dominates heavy particle interactions giving a mean free path of $\sim$ 1 mm in 100 mT of neutrals, which will prevent the free acceleration of ions. However, the existence of an ion current will deplete the neutral density by charge exchange, giving a fast neutral which is then lost from the system. The equation describing the conservation of slow neutrals may be written:

$$\frac{\partial N}{\partial t} + \nabla N V = - F\sigma N - nNS + \alpha n_e^2 \qquad \ldots (5.1)$$

where F is the ion flux and σ the charge exchange cross-section and S and α the ionization and recombination coefficients. Heavy particle collisional ionization has been neglected because of its small cross-section compared to charge exchange, and further interaction of the fast neutrals is ignored because of the small flux compared to F. Hence V is a constant, the unperturbed neutral flow velocity. In the steady state, assuming ionization balance, (5.1) gives a scale length for neutral depletion $L = V/F\sigma$. If $F = 1.3\times10^{23}\ m^{-2}/s$ (i.e. 100 amps ion current) and $V = 10^3\ m/s$ corresponding to neutral inflow velocity, then $L = 2.5\,cm$. Thus only close to the anode would one expect the neutral density to be sufficiently high to prevent free ion acceleration. The time required to set up such a neutral density distribution is $\tau \sim 1/F\sigma = 250\,\mu s$, which is comparable to times of interest, and consistent with the observations of Chapter IV. For low current density accelerators (Morozov, 1972a; Cole, 1972) where the ion current may be as little as ~ 1 amp, the depletion length L is $\sim 3m$ which being much longer than the accelerator dimensions, means that these devices operate with a uniform neutral density. In order to keep the ion-neutral mean free path longer than the anode-cathode separation the filling pressure must be $\leqslant 0.3\ m\tau$ for such low current operation.

This approach breaks down where the ion flux is increasing due to ionization since this contributes to neutral depletion, if $nNS > F\sigma N$ or $n_e > 2.8 \times 10^{17}\ e^{13.6/T}\ T^{\frac{1}{2}}$ (i.e. $n_e \geqslant 2 \times 10^{23}$ for $T_e = 1\,eV$ or $n_e \geqslant 2 \times 10^{19}$ for $T_e = 4\,eV$).

5.3 AN IONIZATION LIMIT TO ACCELERATION

The ion conservation equation can be written down:

$$\frac{\partial n_e}{\partial t} + \nabla n \underline{V} = nNS - n_e^2 \alpha + nN\sigma_i \left| (V - V_N) \right| \qquad \ldots (5.2)$$

where the final term represents ionization due to ion-neutral collisions. Notice that, since ionization cross-sections for H_2 and H are similar, it is not necessary to distinguish between the two in this equation. The scale length for increase in ion flux due to heavy particle collisional ionization $\lambda = 1/N\sigma_i$ is $\sim 12\,\text{cm}$ for $N \approx 10^{21}\,\text{m}^{-3}$ close to the anode and $\sim 1\,\text{m}$ for $N \simeq 10^{20}$ in stage two, and so contributes little to the ionization. The scale length for increase in flux due to electron collisional ionization is $\lambda = V/NS$. Writing $V = \rho_{Li}\,\omega_i\ \text{m/s}$ and

$$S = 1.4 \times 10^{-13}\, e^{-13.6/T}/T^{\frac{1}{2}}\ \text{m}^3\text{s}^{-1}$$

(Hinnov and Hirschberg, 1962) gives

$$\frac{\rho_{Li}}{\lambda} = \frac{N}{\omega_{ci}} \cdot \frac{1.4\, e^{-13}}{T^{\frac{1}{2}}}\, e^{-13.6/T} \qquad \ldots (5.3)$$

where ρ_{Li} is the ion Larmor radius and ω_{ci} is the ion cyclotron frequency $\left(\omega_{ci} = \frac{eB}{m_i}\right)$. The maximum value of the RHS occurs at $T = 27.2\,\text{eV}$ giving the limiting Larmor radius $\frac{\rho_{Li}}{\lambda} = 1.5 \times 10^{-22}\,N/B$. Hence for $N \sim 10^{21}\,\text{m}^{-3}$ and $B \simeq 0.1\,\text{T}$, $\rho_{Li}/\lambda \sim 1.5$ and smaller for smaller N. In other words, the Larmor radius will always be small compared to the length of the ionization region. Qualitatively this will explain the poor divergence of the two stage accelerator where ionization is observed to occur throughout the length of the device, and one might expect that other accelerators with large ionization regions will suffer in a similar way. Notice the limit is independent of electric field which enters indirectly via the scale length λ. The limitation can be circumvented by controlling λ — having an ionization region of small axial dimensions in which the axial ion flux is built up at high density and low velocity, followed by a region of low ionization where acceleration increases the mean velocity but preserves the flux. In the latter region, the Larmor radius can be large.

5.4 SOLUTION OF ACCELERATOR EQUATIONS IN ONE DIMENSION

For the E and B configuration of Fig.1.2, the imposition of uniformity in the direction of the Hall current (Y) and the assumption $V_x = 0$ allow simple steady state fluid equations to be written down to describe ion and neutral motion. Pressure gradients are neglected.

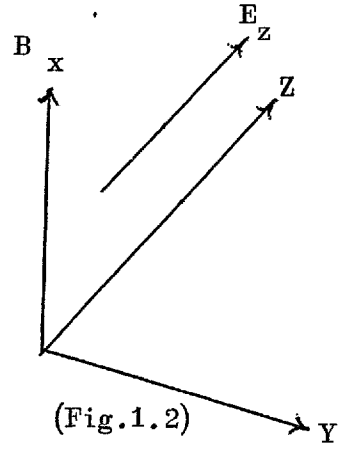

(Fig.1.2)

$$
\left.
\begin{aligned}
&\text{(a)} \quad \frac{d n V_z}{dz} = -\frac{d}{dz}\left(N V_{zN}\right) = ION \\
&\text{(b)} \quad \frac{d}{dz}\left(n m V_z^2\right) = -j_y B - K_z \\
&\text{(c)} \quad \frac{d}{dz}\left(n m V_z V_y\right) = j_z B - K_y \\
&\text{(d)} \quad \frac{d}{dz}\left(N m V_{zN}^2\right) = +K_z \\
&\text{(e)} \quad \frac{d}{dz}\left(N m V_{zN} V_{yN}\right) = +K_y \\
&\text{(f)} \quad \frac{j_y}{\sigma} = V_z B - \frac{j_z B}{ne}
\end{aligned}
\right\} \quad \ldots (5.4)
$$

where $ION = nNS + nN\sigma_i \left|V - V_N\right|$ represents the total ionization rate, K represents ion-neutral momentum exchange due to charge exchange collisions. j_z is assumed to be specified by the external circuit. If the equations (5.4) are manipulated into the form $\frac{dn}{dz} = \ldots$ etc. then the set of equations can be solved on the computer assuming boundary values at one electrode, using one of the many difference schemes (Potter, 1972). The electron temperature enters the equation via the conductivity σ and the electron collisional ionization, and is either solved for using a steady state equation of the form (2.3), or simply set.

Fig.5.1 shows typical solutions for the case of anode values $n_e = 2\times10^{19}\ m^{-3}$, $N = 1\times10^{21}\ m^{-3}$, $V_z = 10^4\ m/s = V_{zN}$ where

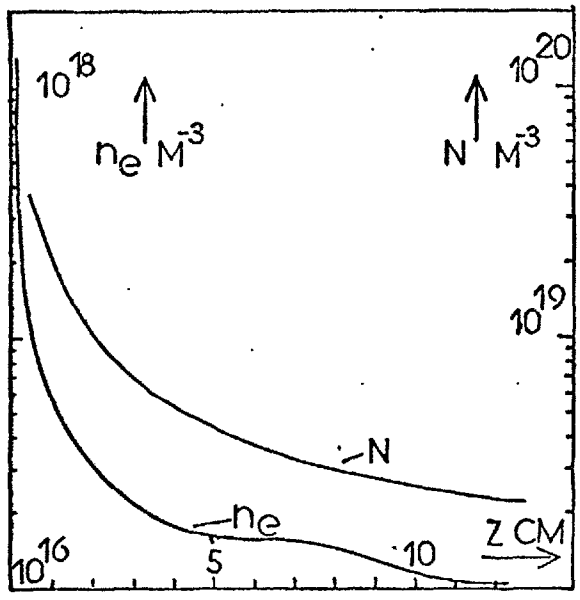

Fig.5.1
1-D solutions for n_e and N (electron and neutral densities) for anode conditions $n_e = 2 \times 10^{19} m^{-3}$, $N = 10^{21}$ m^{-3}, $v_z = v_{zn} = 10^4$ m/s

$B = 0.1 \sin \frac{2\pi z}{0.14}$. A constant $T_e = 3$ eV is used here, and a discharge current $j_z = 2.5 \times 10^5$ A/m^2 supplied. The main characteristics of such solutions is the decline in electron density, much steeper than observed experimentally, to a plateau $n_e = 10^{16} m^{-3}$ of very tenuous plasma. The neutral density falls, as predicted in section 5.2, at a similar rate to the experiment. The low density means that ionization is low, so the ion flux remains constant, the acceleration of ions resulting in a falling density. The large values of $\omega\tau$ arising from the low densities ensures that the Hall current is large, $j_y \sim -\omega\tau j_z$. This large current depletes the plasma by acceleration and, indirectly, the neutrals via charge exchange, giving rise to a larger $\omega\tau$ and an increased acceleration. Equation (1.5) gives $E_z = \frac{1 + (\omega\tau)^2}{\sigma} j_{ze}$, where j_{ze} is the electron current. The low ionization prevents the ion flux from increasing to carry more than a small fraction of the discharge current, so that $j_{ze} \sim j_z$. The large value of $\omega\tau$ then gives a large E_z, typically $\sim 10^5$ to 10^7 V/m and total discharge voltages ~ 100 kV. This illustrates the major fault in such a one-dimensional approach, since for typical discharge currents ~ 1 kA and the usual capacitor bank external circuit, it would not be possible to sustain such a large anode-cathode voltage. Since the solutions obtained are largely independent of the anode values assumed, there is no way in which the external circuit equation can be included to ensure reasonable values of voltage and current.

It is shown in a later chapter how, at some considerable cost in complexity, a physically realisable circuit may be included, by generalizing the problem to include two space dimensions and time.

5.5 CONCLUSIONS

The work presented in this chapter demonstrates the inapplicability of a single dimension approach to Hall acceleration in an open ended device. The low ionization rate gives rise to low plasma density and in consequence an unphysically large collisional electron resistivity in the direction of the applied E . The unsuitability of this model does not detract from the earlier conclusions based on one dimensional arguments, in which neutral depletion is accounted for by charge exchange, and small ion Larmor radius divergence shown to be inevitable in the presence of an extended ionization region.

CHAPTER VI

THE SIGNIFICANCE OF ION TRAJECTORIES

This chapter shows that useful information concerning the accelerated plasma can be obtained by considering the form of ion motion in typical field configurations. Quantitative comparison is made with experiment.

6.1 THE APPLICABILITY OF THE MODEL

The simple theory of section 1.4 shows that fluid acceleration by the interaction of Hall current and magnetic field is equivalent to free acceleration of single ions in the electric and magnetic fields, providing the Hall parameter, $\omega\tau$, is large. It is self-evident that no additional information will be obtained from ion orbits in three dimensions unless the ion collisional mean free path, λ_i is sufficiently large that:

$$\lambda_i \geqslant L \quad \text{where } L \text{ is the stage length.}$$

For hydrogen, the dominant ion-neutral cross-section is charge exchange ($\sigma_{cE} \simeq 2\times10^{-19}$ m^2 for a 2 keV ion - Oak Ridge tables) so that

$$\lambda_{icE} \sim 1/(7p) \text{ m}$$

where p is the filling pressure in mτ. Typically $p \sim 100$ mτ and $\lambda_{icE} = 1.4$ mm, so that initially the free acceleration picture is not valid. However the charge exchange reactions sweep out the neutrals to give the observed neutral density of Chapter IV. Thus λ_{icE} becomes $\geqslant 5$ cm beyond 2 cm from the anode, increasing rapidly with distance. Near the anode, ion trajectories are not useful, but ions diffuse to the boundary where λ_i becomes large, where subsequent orbits are free from collisions. Calculations performed for this region are useful.

6.2 THE EQUATIONS AND THE METHOD OF SOLUTION

For the cylindrically symmetric fields of most Hall accelerators, the coordinate system of Fig.6.1 is appropriate, $\underline{B}$ and $\underline{E}$ lie only in the $\underline{R}-\underline{Z}$ plane.

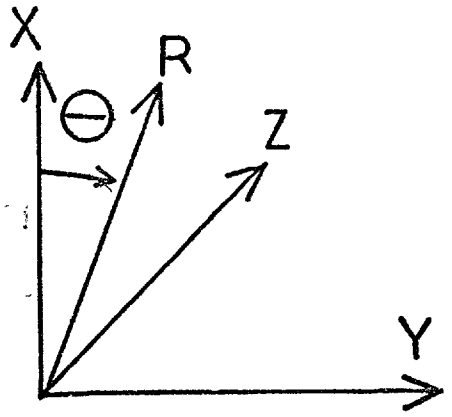

Fig.6.1
The coordinate system

The equations of motion are:

$$\left.\begin{aligned} m\frac{d^2r}{dt^2} &= eE_r + eB_zV_\theta + \frac{mV_\theta^2}{r} \\ m\frac{d^2z}{dt^2} &= eE_z - eV_\theta B_r \\ \frac{m}{r}\frac{d}{dt}r^2\frac{d}{dt}\theta &= eV_zB_r - eV_rB_z \end{aligned}\right\} \quad \ldots (6.1)$$

Kilkenny has considered a similar set of equations for ion motion in the Polytron (Kilkenny, 1972) and in certain limited cases has found analytic solutions. Here a numerical approach is more appropriate. The simple leapfrog difference scheme is not suitable for these equations because of the velocity terms on the right hand sides (Potter, 1972). However, using the vector potential A_θ to describe the magnetic field, the equations can be put in a more suitable form.

Using $B_r = -\frac{\partial A_\theta}{\partial z}$ and $B_z = \frac{1}{r}\frac{\partial}{\partial r}(rA_\theta)$ we obtain

$$m\frac{d}{dt}(rV_\theta) = er\left\{-V_z\frac{\partial A_\theta}{\partial z} - \frac{V_r}{r}\frac{\partial}{\partial r}rA_\theta\right\}$$

where the right hand side is a total derivative and can be integrated to give:

$$rV_\theta = -\frac{erA_\theta}{m} + c \qquad \ldots (6.2)$$

V_θ and the right of equations (6.1) are now functions of position only:

$$m\frac{d^2r}{dt^2} = eE_r + \left\{\frac{e}{r}\frac{\partial}{\partial r}(rA_\theta)\right\}\left\{-\frac{eA_\theta}{m} + \frac{c}{r}\right\} + \left\{\frac{c}{r} - \frac{eA_\theta}{m}\right\}^2\frac{m}{r} \quad \ldots (6.3)$$

$$m\frac{d^2z}{dt^2} = eE_z + \frac{e\partial A_\theta}{\partial z}\left\{\frac{c}{r} - \frac{eA_\theta}{m}\right\} \quad \ldots (6.4)$$

which are of the form $\frac{d\underline{x}}{dt} = \underline{v}$ and $\frac{d\underline{v}}{dt} = \underline{P}(x)$ so that the leapfrog scheme can be applied. The algorithm for the solution is (Potter, 1972) :

$$\underline{x}^n = \underline{x}^{n-2} + 2\Delta t\ \underline{v}^{n-1}$$
$$\underline{v}^{n+1} = \underline{v}^{n-1} + 2\Delta t\ \underline{P}^n \quad \ldots (6.5)$$

where n is the time level and Δt the timestep. Position $\underline{x}$ and velocity $\underline{v}$ are defined at alternate time levels, and the time centred approach gives second order accuracy.

6.3 PROCEDURE FOR THE INTEGRATION

The coding of equations (6.2), (6.3) and (6.4) is straightforward. The timestep is chosen $\Delta t \ll \frac{eB}{m_i}$, and stability and accuracy checked using energy conservation. The uncertainty in initial position, which is some fraction of the first step, is reduced by performing the first 100 steps with timestep 1/100 of that used in the main calculation. The numerical procedure was checked by performing calculations which could be readily checked analytically.

6.4 TRAJECTORIES IN IDEALISED FIELDS

Let us first consider a very simple field configuration appropriate to an iron magnet design.

$0 \le z \le D$	$B_r = B_0R_1/r$	$B_z = B_{zo}R_1/r$	$E = E_{zo}$
$D < z < S\text{-}D$	$B_r = 0$	$B_z = B_{zo}R_1/r$	$E = 0$
$S\text{-}D \le z \le S$	$B_r = -B_oR_1/r$	$B_z = B_{zo}R_1/r$	$E = E_{zo}$

i.e. two stages, length D, of radial B field with a constant E_{zo}, separated by a region of purely axial B, giving a total length S. For

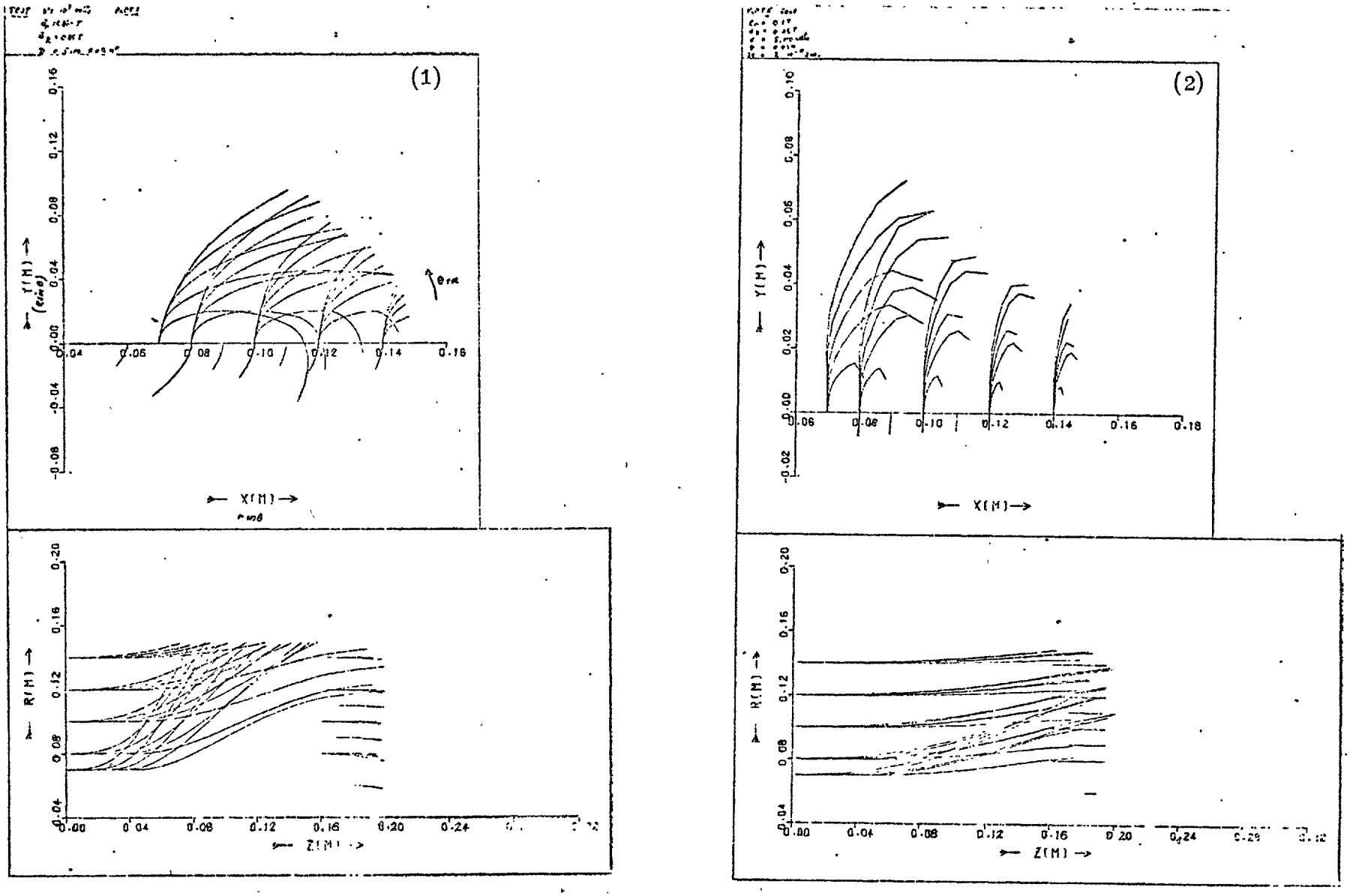

Fig.6.2

H^+ ion trajectories in the r-z and azimuthal planes for the idealised fields of the text, for voltages (1) 1kV and (2) 5kV. Distances are in m.

the first calculations we choose $R_1 = 5\,cm$, $S = 20\,cm$ and $D = 5\,cm$ with $B_o = 0.1\,T$, $B_{zo} = 0.05\,T$. This is somewhat larger than the device considered in this thesis, but similar to some Russian devices (Morozov, 1968). Some typical H^+ trajectories are shown in Fig.6.2 for voltages 1 kV and 5 kV. The initial ion velocities are taken zero. The early motion is non-divergent despite appreciable azimuthal motion. Radial motion is most pronounced near the inner wall at R_o, where B is strongest and centrifugal effects are most important. v_θ changes sign for all ions started in the anode stage. The final velocities for an H^+ ion with $v = 1\,kV$ and started at $z = 0$ are: $v_z = 1.4\times10^5$ m/s, $v_r = 2.6\times10^5$ m/s and $v_\theta = 4.4\times10^4$ m/s. v_θ is low since from (6.2)

$$v_\theta = \frac{e}{m}\left(\frac{(rA_\theta)_c}{r} - A_\theta\right)$$

where the subscript c indicates evaluation at the point of creation. Although v_θ undergoes a large excursion, up to $v_\theta = 1.5\times10^5$ m/s given by the peak on $|A_\theta|$, the ion migrates to a region of smaller $|A_\theta|$ so that v_θ is small at the cathode at $z = S$. Fig.6.3 shows A_θ as a function of z. The trajectory of a similar ion in $z - A_\theta$ space is also shown in Fig.6.3, though this ion created at $r = R_o$ does not escape. The divergence arises because of the contribution to $ev_\theta \wedge B_z$ and mv_θ^2/r terms from the large v_θ excursion.

If B_z is taken in the opposite direction, these two terms are in opposition, and divergence should be reduced. For the trajectories in Fig.6.4(1) a field of the form $B_z = \frac{r - 0.07}{0.07}\,T$ (where r is in metres) is chosen, so that B_z reverses sign at $r = 0.07\,m$ but is of similar magnitude to the case just considered. This field, sketched in Fig.6.4(2) produces strong ion focusing, though any improvement over the trajectories in Fig.6.2(2) is masked because of the large spread in initial position.

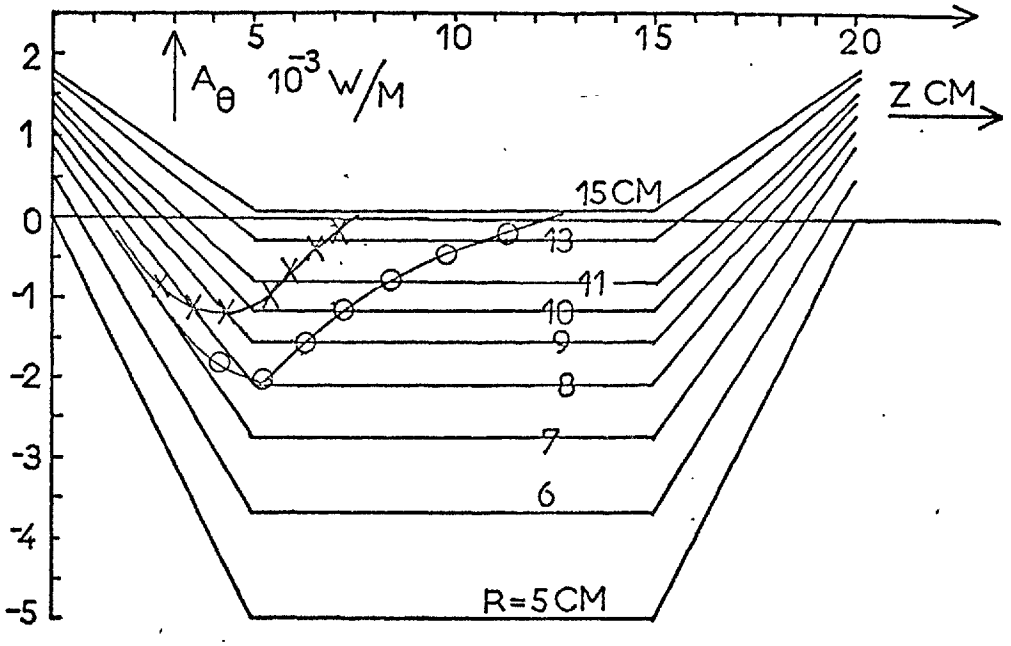

Fig.6.3

The vector potential A_θ as a function of axial position Z (cm). Also shown are H^+ ion trajectories in this Z - A plane; x V = 1kV , o V = 5kV

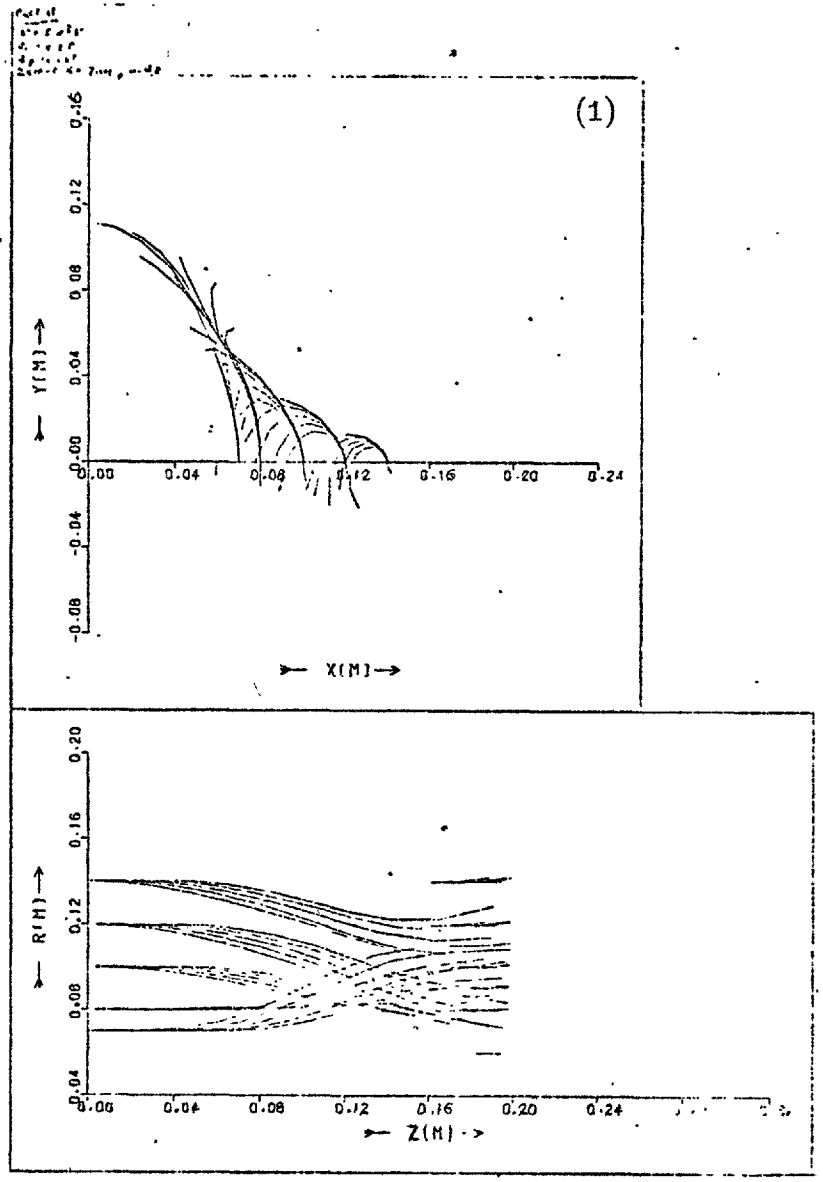

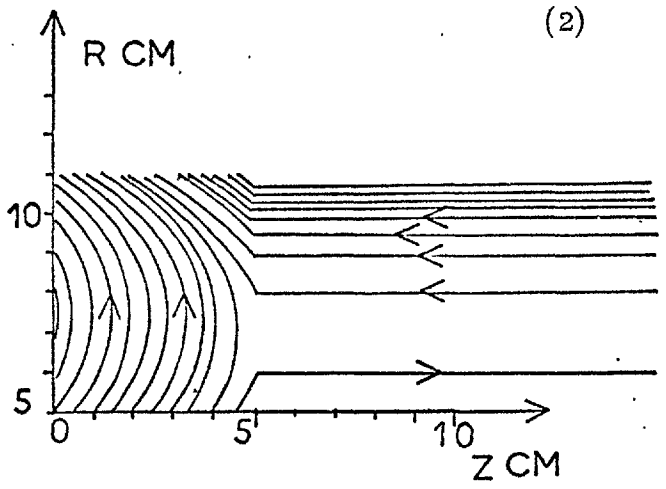

Fig.6.4

(1) H^+ ion trajectories with an axial field to assist focusing. $B = 0.1\,T$, $B_Z = 0.05\,T$ at $r = 0.05\,m$, $B_Z = 0$ at $r = 0.07\,m$. $V = 5\,kV$.

(2) Shows the field lines for the first stage of this configuration

The ions start at 1cm intervals in the axial direction

6.5 MOTION IN A PURELY RADIAL FIELD

Let us take a magnetic field of the form:

$0 < z < D$	$B_r = \frac{B_0 R_0}{r}$	$B_z = 0$	$E = E_{zo}$
$D \leq z < S-D$	$B_r = 0$	$B_z = 0$	$E = 0$
$S-D \leq z \leq S$	$B_r = -\frac{B_0 R_0}{r}$	$B_z = 0$	$E = E_{zo}$

The equations of motion (6.2), (6.3), (6.4) are as follows for ions in the first stage created at $z = 0$, $r = R_1$:

$$V_\theta = \omega \frac{R_1 z}{r}$$

$$\frac{d^2 r}{dt^2} = -\omega^2 R_1^2 z^2 / r^3 \qquad \ldots (6.6)$$

$$\frac{d^2 z}{dt^2} = \frac{eE_z}{m} - \omega^2 \frac{R_1^2}{r^2} z$$

where $\omega = eB/m$ is the ion gyro frequency. To a first approximation, $r = R_1$ if ωz is small. The solution for z motion is then

$$z = \frac{eE_z}{m\omega^2}(1 - \cos \omega t) = \rho(1 - \cos \omega t)$$

where ρ is the ion Larmor radius. At $z = D$, $v_\theta \simeq \omega D$ and

$$v_z = \left[\frac{2eED}{m} - v_\theta^2 \right]^{\frac{1}{2}} = \omega (D\rho)^{\frac{1}{2}} (1 - D/\rho) .$$

The motion between the stages is the straight line in Fig.6.5, and the ion will strike the wall before entering the second stage if

$$\frac{v_z}{v_\theta} < \frac{S-2D}{w}$$

or

$$\left(\frac{\rho}{D}\right)^{\frac{1}{2}} \leq \frac{S-2D}{w} \qquad \ldots (6.7)$$

where w is the channel width. Typically, $\frac{S-2D}{w} \sim 2$, so $\rho \geq 4D$ for the ion to reach the second stage. For long narrow regions

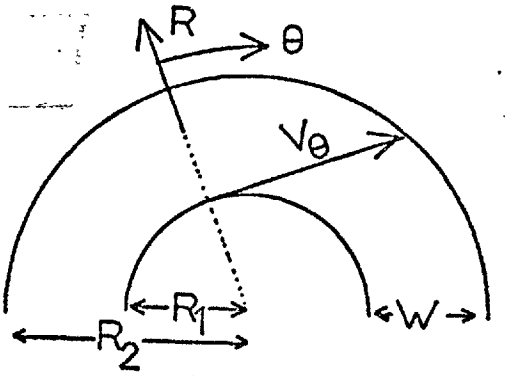

Fig.6.5
Ion motion between stages in the azimuthal plane. The walls are w apart radially

between the poles, this criterion can be somewhat severe. It is not easy to treat the second stage, since $r \neq R_1$, but condition (6.7) must be well satisfied for an ion to escape stage two.

6.6 MOTION IN A FIELD GIVEN BY $A_\theta(z)$

Let us choose a magnetic field specifid by A_θ as in Fig. 6.6, where A_θ is independent of r. For $0 < z < D$ we have

$$A_\theta = - A_o z/D \ , \quad B_r = A_o/D = B_{ro}$$

and $$B_z = - \frac{1}{r} \frac{A_o z}{D} = - \frac{B_{ro} z}{r}$$

where B_{ro} and A_o are constant. The exact equations of motion in this region for an ion created at $z = 0$, $r = R_o$ are:

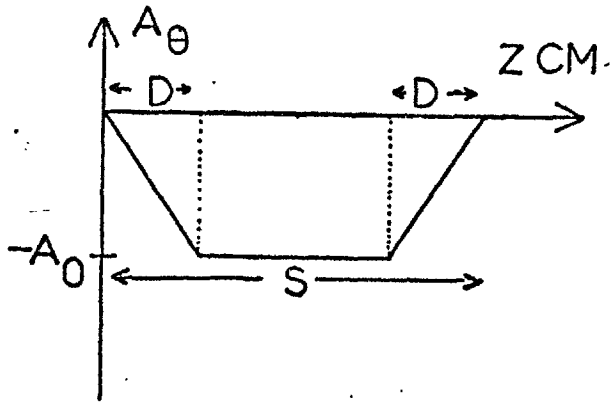

Fig.6.6
Vector potential as a function of position z . The two regions of length D are the two stages

$$v_\theta = - \frac{eA_\theta}{m} = \frac{e}{m} B_{ro} z = \omega z$$

where $\omega = \frac{eB_{ro}}{m}$,

$$\frac{d^2z}{dt^2} = \frac{eE_z}{m} - \omega^2 z \quad , \quad \text{i.e.} \quad z = \frac{eE_z}{m\omega^2} (1 - \cos\omega t)$$

and

$$\frac{d^2r}{dt^2} = - \frac{\omega z}{r} \cdot \omega z + \frac{\omega^2 z^2}{r} = 0 .$$

There is no radial motion whatever since $v_\theta \wedge B$ cancels v_θ^2/r. Between the stages, $D < z < S-D$, $B_r = 0$, $A_\theta = - A_o$, $B_z = - A_o/r$, and again $\frac{d^2r}{dt^2} = 0$, i.e. the ion undergoes a Larmor orbit in B_z of radius R_o. In the second stage $B_z = - B_{ro}(s-z)/r$ so that centrifugal and $v_\theta \wedge B$ terms still balance. $v_r = v_\theta = 0$ at $z = S$, so that an ion beam would be well collimated.

It is easy to see that the same holds for any field such that $v_\theta = - \frac{e}{m} r B_z$, i.e. $A_\theta = \frac{\partial}{\partial r} r A_\theta$. Any vector potential independent of r will satisfy this requirement. Note that no restriction is placed on

$\underline{E}$ except that $E_r = 0$. Thus a requirement for a practical system might be that radial variations in A_θ be much less than axial variations.

$$\frac{\partial A_\theta}{\partial r} \ll \frac{\partial A_\theta}{\partial z} \quad . \qquad \ldots (6.8)$$

6.7 FIELD CALCULATIONS FOR A MAGNET SYSTEM

In order to use the computational procedures described in sections 6.2 and 6.3 to model the accelerator described earlier in this thesis, a method was developed for calculating the field in a cylindrical magnet system. For a static problem, we have the differential form of Amperes Law:

$$\nabla \wedge H = \underline{J} \qquad \ldots (6.9)$$

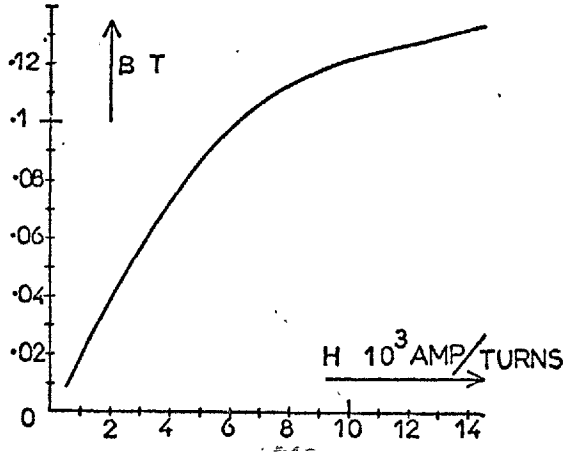

Fig.6.7
Pole field dependence on coil current for 2-stage magnet

where $\underline{J}$ is the conduction current flowing through the medium. For small fields in soft magnetic materials, $B = \mu H$ where μ the permeability is a constant. Fig.6.7 shows this holds good for $B \leqslant 0.1$T for the soft iron of the two stage magnet. Thus (6.9) becomes

$$\nabla \wedge (\frac{1}{\mu} \nabla \wedge A) = J \qquad \ldots (6.10)$$

or $$\nabla^2 \underline{A} = - \mu . \underline{J} \qquad \ldots (6.11)$$

except at the boundaries of the magnetic material, where the usual boundary conditions are imposed on $\underline{B}$ and $\underline{H}$, i.e.

$$H_{\parallel}^{in} = H_{\parallel}^{out} \quad , \quad B_{\perp}^{in} = B_{\perp}^{out} \qquad \ldots (6.12)$$

which are equivalent to conditions on the vector potential :

$$\frac{\partial A^{in}}{\partial S} = \frac{\partial A^{out}}{\partial S} \quad \text{and} \quad \frac{1}{\mu} \frac{\partial A^{in}}{\partial n} = \frac{1}{\mu_o} \frac{\partial A^{out}}{\partial n} \qquad \ldots (6.13)$$

where the superscript 'in' and 'out' refer to magnetic material and vacuum, and S and n refer to gradients taken tangentially and normally to a surface. (6.11) and (6.13) are solved numerically.

6.8 NUMERICAL SOLUTION OF $\nabla^2 A = -\mu J$ IN A CYLINDRICAL SYSTEM WITH ARBITRARY BOUNDARIES

In an $r-\theta-z$ coordinate system with θ symmetry, (6.11) can be written

$$\frac{1}{r}\frac{\partial A}{\partial r} + \frac{\partial^2 A}{\partial r^2} + \frac{\partial^2 A}{\partial z^2} - \frac{A}{r^2} + \mu J = 0 \qquad \ldots (6.14)$$

For the mesh, Fig.6.8, labelled by i and j and compass point notation, the difference representation of the LHS of (6.14) is:

$$(A_N + A_E + A_S + A_W - 4A_c) + \frac{A_N - A_S}{2(J-1)} - \frac{A_c}{(J-1)^2} + \mu\Delta^2 J_c = P_c \qquad \ldots (6.15)$$

It is possible to iterate to such a solution using successive over relaxation (Potter, 1972), using the algorithm

$$A_c^{n+1} = A_c^n + \omega P_c^n \qquad \ldots (6.16)$$

where n indicates the iteration level, P_c is defined by equation (6.15), and ω is the relaxation parameter. When $(A_c^{n+1} - A_c^n)/A_c^n \ll 1$, $P_c \ll 1$ so that the convergence of (6.16) gives a solution to (6.14). ω is chosen to give the most rapid convergence.

The mesh points lying on boundaries of the magnetic material are treated separately. The use of A_θ in the solution for points adjacent to the boundary implicitly conserves $B_\perp$ across a boundary. The condition

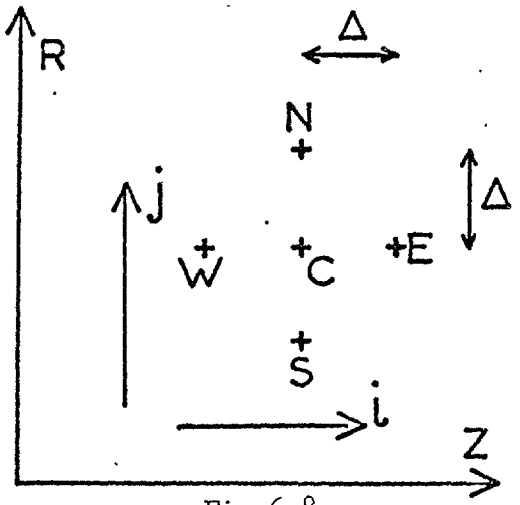

Fig.6.8
Mesh notation for vector potential solution. Points are labelled by indices i,j. The mesh spacing is Δ

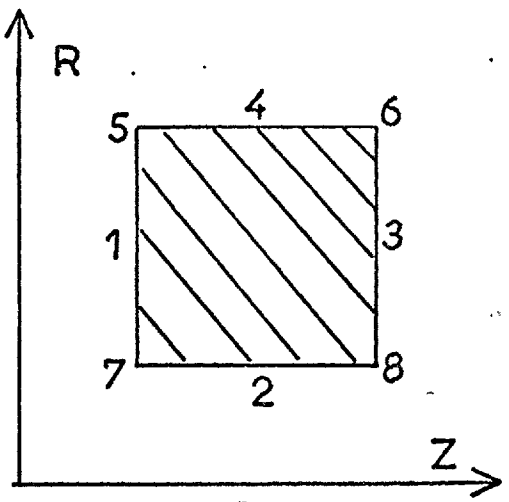

Fig.6.9
Types of boundary point. Surfaces 1.4, corners 5.8

on $H_{\|}$ determines A_θ on the boundary. The types of boundary point are classifed by Fig.6.9, there being 8 algorithms in all required to describe the boundary points. For a type 4 surface for example, the condition on $H_{\|}$ is to first order:

$$\frac{A_c + A_N}{2(J-1)\Delta} + \frac{A_N - A_c}{\Delta} = \frac{\mu_o}{\mu}\left\{\frac{A_S + A_c}{2(J-1)\Delta} + \frac{A_c - A_S}{\Delta}\right\}$$

which for high μ simplifies to:

$$A_c = A_N\left(\frac{2J-1}{2J-3}\right) \qquad \ldots (6.17)$$

6.9 RESULTS FROM THE NUMERICAL METHOD

In order to deal with the 2-stage magnet, a mesh of 120 × 70 points and mesh spacing 1.66 mm was used. However the iteration was slow, as shown in Fig.6.10, requiring ~1000 iterations to converge. Figs.6.11(1) and (2) compare the calculated field-line geometry with that suggested by an iron filings plot, whereas (3) and (4) compare computed and measured B_r and B_z. The agreement is satisfying.

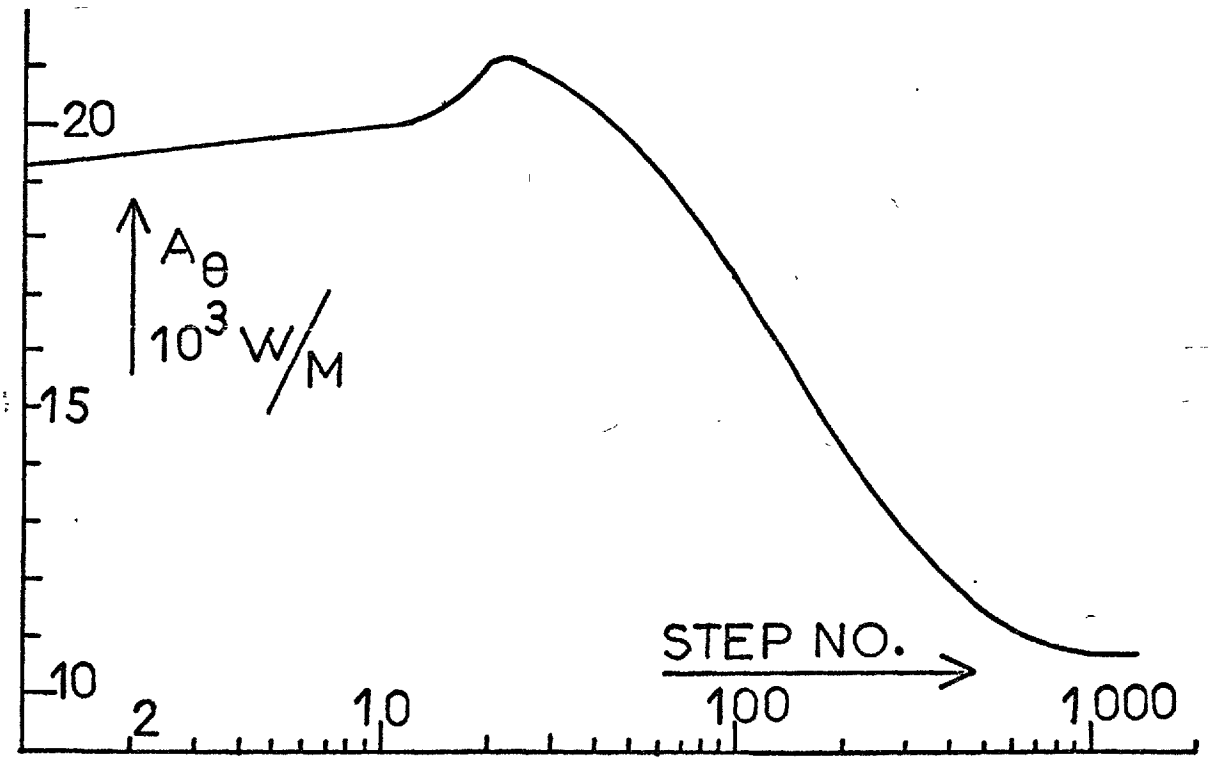

Fig.6.10
The convergence of a solution for a typical iteration. The evolution of A_θ at a particular point is shown

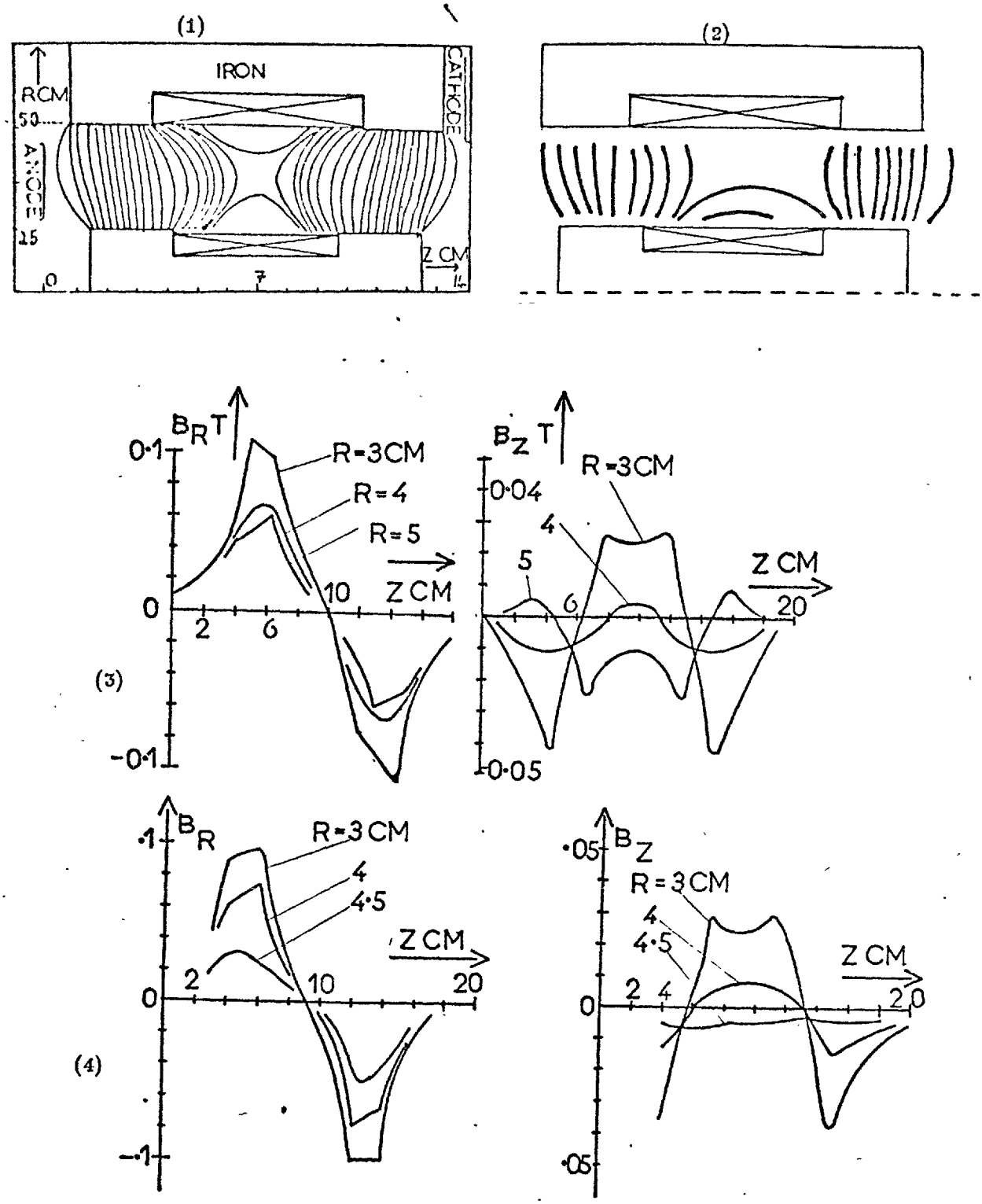

Fig.6.11

Comparison of experimental and computed 2-stage magnetic fields. (1) computed field lines; (2) ion filings plot; (3) computed B_z and B_r; (4) measured B_z and B_r

6.10 TRAJECTORIES IN COMPUTED 2-STAGE FIELDS

The magnetic field calculated in this way is used in the trajectory calculations. In order that comparison with experiment should be possible, the axial electric field distribution used was that determined experimentally in Chapter III. A typical set of trajectories are displayed graphically in Fig.6.12, for H_2^+ ions in a peak radial field of 1.1 kG and voltage 1 kV. Ions created in the first stage strike the wall because the axial field between the stages is insufficient to counterbalance the centrifugal motion, whereas ions created in the second stage have a maximum azimuthal velocity upon reaching the anode, and so diverge in the exhaust. The large $\sim 30^{\circ}$ radial divergence of these ions is comparable to the large experimentally observed divergence.

6.11 THE SIGNIFICANCE OF E_r FIELDS

The experiments in Chapter III have demonstrated the existence of a radial electric field E_r, consistent with the field-line/equipotential equivalence expected on the basis of high plasma conductivity. This value of E_r has been used in the calculations, and found only to affect significantly those ions created just before entering a region of strong E_r. Those ions created at the beginning of either stage where the B field is strongly bowed are initially accelerated in the direction of E, i.e. normal to B. Examples of such trajectories are shown in Fig.6.13. These H_2^+ ions, created near the anode enter a field region which by Fig.6.11 is lens shaped, but overfocusing of trajectories only assists rapid loss of ions to the wall. This wall impact could well be the cause of the severe wall blistering and erosion observed in the first stage. Those ions which are created in the regions where the B field is almost purely radial have an appreciable axial velocity before entering E_r regions, and are virtually unaffected. However these results serve as a reminder of the naivety of criterion (6.8).

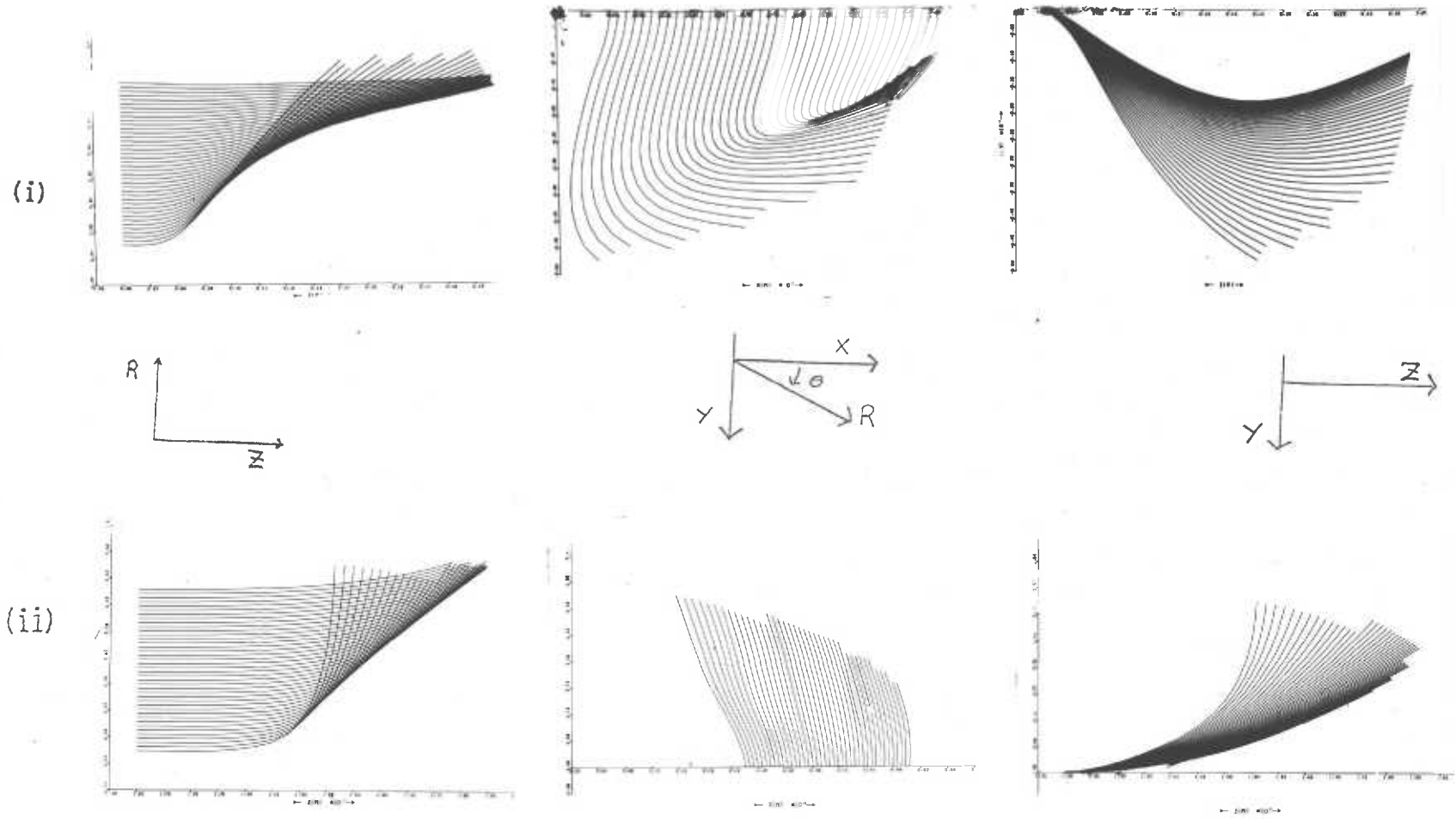

Fig.6.12

Trajectories of H_2^+ ions for a peak radial field of 1.1 kg and voltage 1 kV. The r-z, x-y and y-z planes of Fig.6.1 are shown. (i) shows ions created in the first stage, and (ii) shows ions created in the second stage

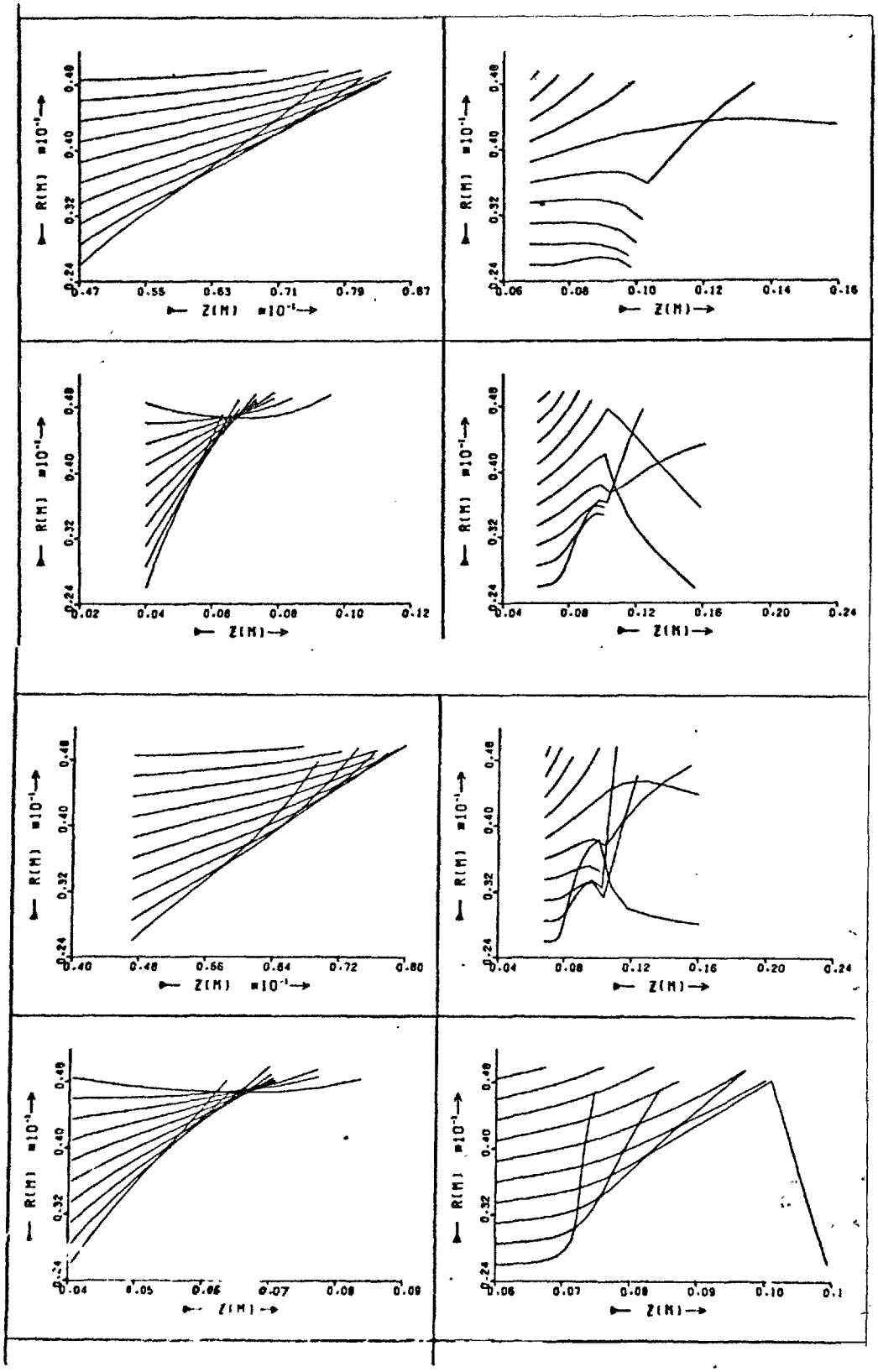

Fig.6.13

H_2^+ ion trajectories in experimental E_r, E_z. Voltage = 1 kV, $B_r \simeq 1.1$ kg. The anode is located at z = 0.04 m.

6.12 MODELLING OF THE PLASMA EXHAUST IN THE 2-STAGE DEVICE

Although these trajectories are useful in making qualitative comparison with experiment, a more intimate comparison is desirable. The ion exhaust flux measurements presented in Chapter III provide suitable data since they can be simulated by a particle accounting technique. The computed magnetic field was given the same strength as the experiment, i.e. B_r = 1.1 kg peak on the inner insulator. E_z was taken from Fig. 3.1, and E_r calculated from $E_r = -B_z E_z / B_r$. Sufficient numbers of H^+ and H_2^+ ions were integrated in turn from a uniform grid of creation points to obtain smooth radial exhaust profiles. Weight factors were assigned to each ion to account for the cylindrical nature of the problem, and the axial dependence of ionization determined in the experiment (Fig. 4.9). Figs.6.14(1) and (2) compare the experimental and computational profiles of relative ion flux density, for H^+ and H_2^+ ion calculations, both at the cathode aperture, and 15 cm away in the exhaust. The form of the computed profiles are virtually independent of first stage ionization, since most ions created there are lost to the wall. The divergence as expressed by the peak of the ion flux density is somewhat greater for H^+ than H_2^+, but not as large as expected because the most divergent ions are lost to the accelerator wall. The rough agreement between experiment and computation at the cathode indicates that the assumption of uniform radial dependence of ionization holds good. At 15 cm outside the cathode however, there is some disagreement because no combination of the H^+ and H_2^+ fluxes will give the broad distribution observed experimentally. In fact the experiment detects an ion flux at $r = 25$ cm, whereas the calculation produces no such strongly divergent ions whatever. Chapter IV shows there is an appreciable charge exchange neutral flux in the second stage of the accelerator which is ionized beyond the cathode. It is conceivable that this flux will fill in the discrepancies at large and small

(1)

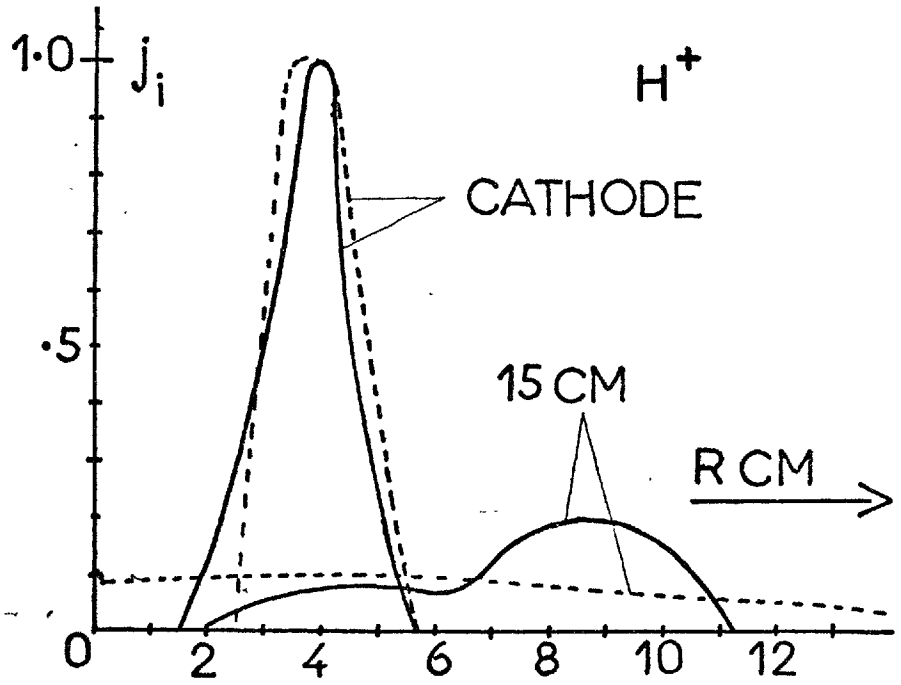

(2)

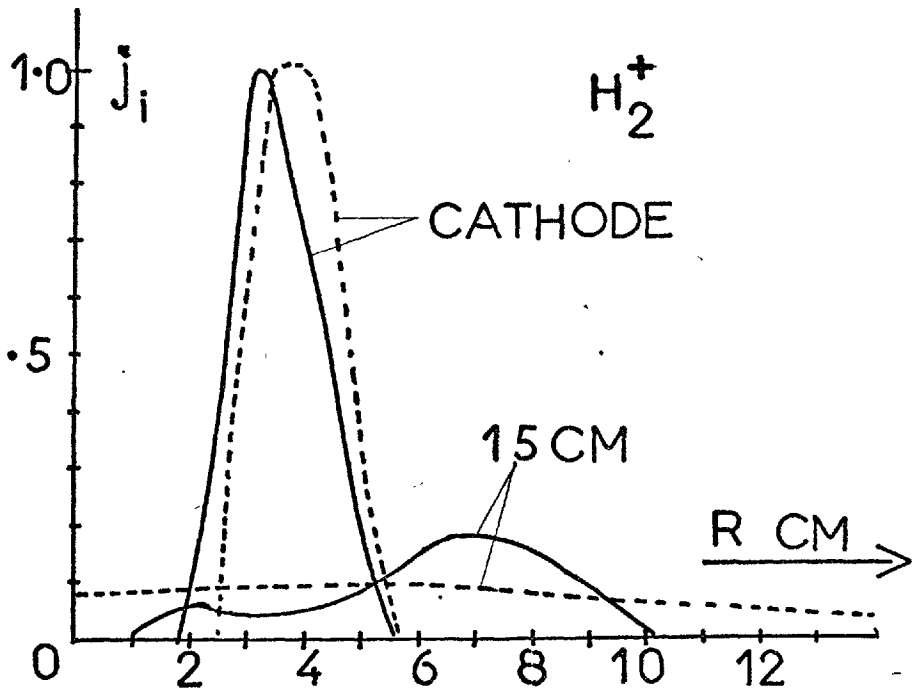

Fig.6.14

A comparison of experimental (----) and computed (——) relative exhaust ion fluxes at cathode and 15 cm into exhaust. In (1) the computation is for H^+ ions and in (2) for H_2^+ ions.

radius. The observed fluctuating electric fields will also contribute towards broadening of the computed profiles.

6.13 TRAJECTORIES IN THE CULHAM 6-STAGE DEVICE

The Culham 6-stage device (Cole, 1974) has three two-stage magnet elements as illustrated in Fig.6.15(1) which displays the computed field configuration. The calculations of B_r (Fig.6.15(2)) agrees well with Cole's measurements, but of particular interest is the axial field (Fig. 6.15(3)). In the calculations this is strong between the poles near the inner and outer walls, giving the field configuration of Fig.6.15(1). Unfortunately there are no measurements of B_z there for comparison.

Cole has operated this accelerator over a wide range of conditions from 10 A at 20 kV to ~70 A at 4 kV (Cole, 1974), and observed a notable increase in efficiency from 10% at 4 kV to 30% and higher at 20 kV. Unfortunately no ion creation or electric field measurements have been performed on this device, and so for the purpose of trajectory calculations, E_z is taken αB_r. For typical peak values of $B_r \sim 500$ g, few ions impact the wall if E_r is taken zero, and high efficiencies ~90% and low divergence $\sim 10^\circ$ seen for voltages as low as ~few kV. These disagree with Cole's observations.

If, however, E_r is assumed to follow the field line/equipotential approximation, the strong B_z becomes important. Fig.6.16 shows H^+ ions from the cathode for a voltage drop of 5 kV. The E_r field gives appreciable wall loss and predicts efficiencies of ~few percent. Since E_z is somewhat conjectural more detailed comparison with experiment is not possible, but these results qualitatively account for the disappointing performance of this device.

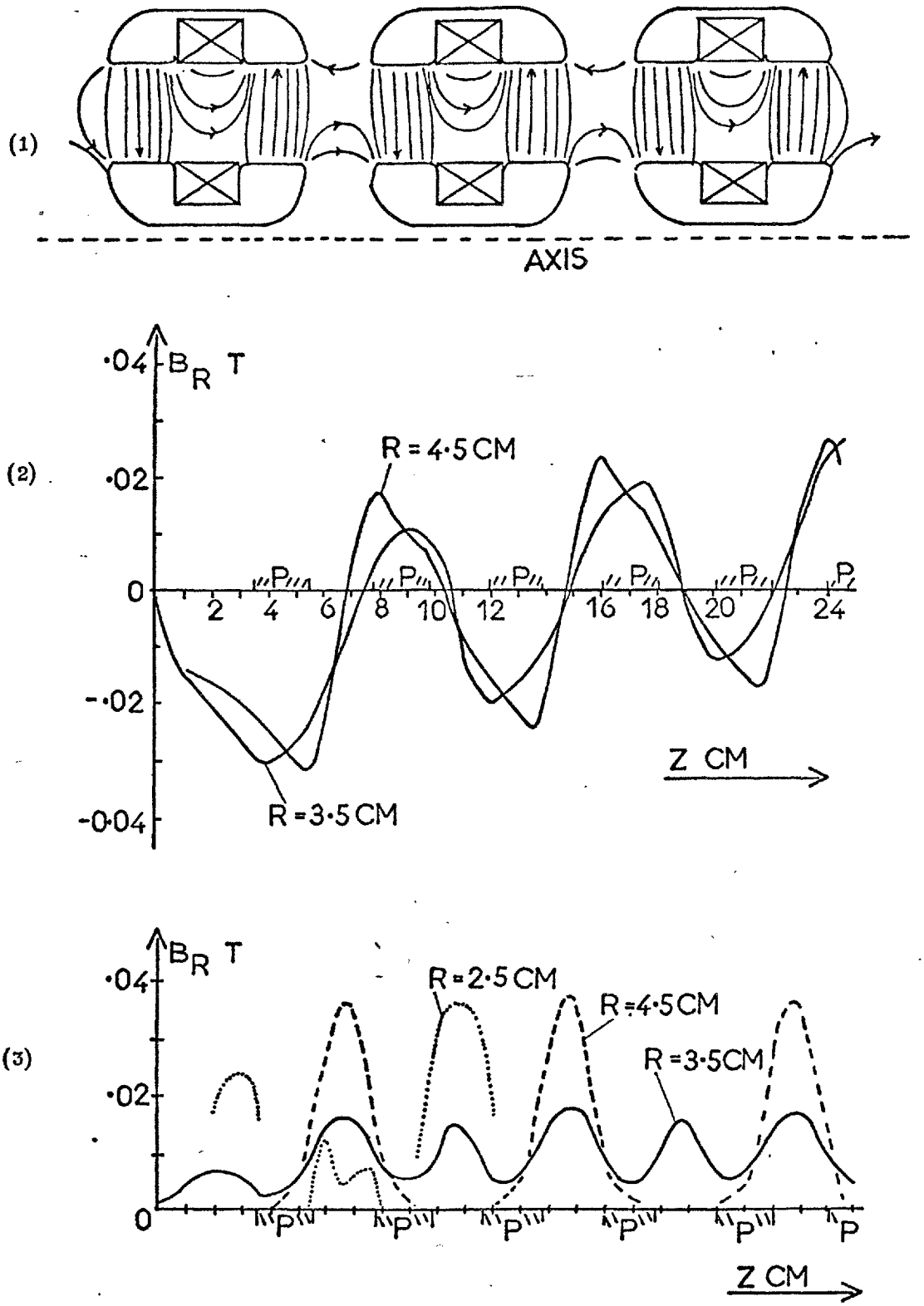

Fig.6.15

(1) Computed magnetic field lines for the 6-stage magnet system. Length of system is 25 cm.
(2) Computed radial field for 10^3 amp-turn coil current. P indicates location of magnetic poles.
(3) Computed axial magnetic field for 10^3 amp-turn coil. P indicates location of magnetic poles.

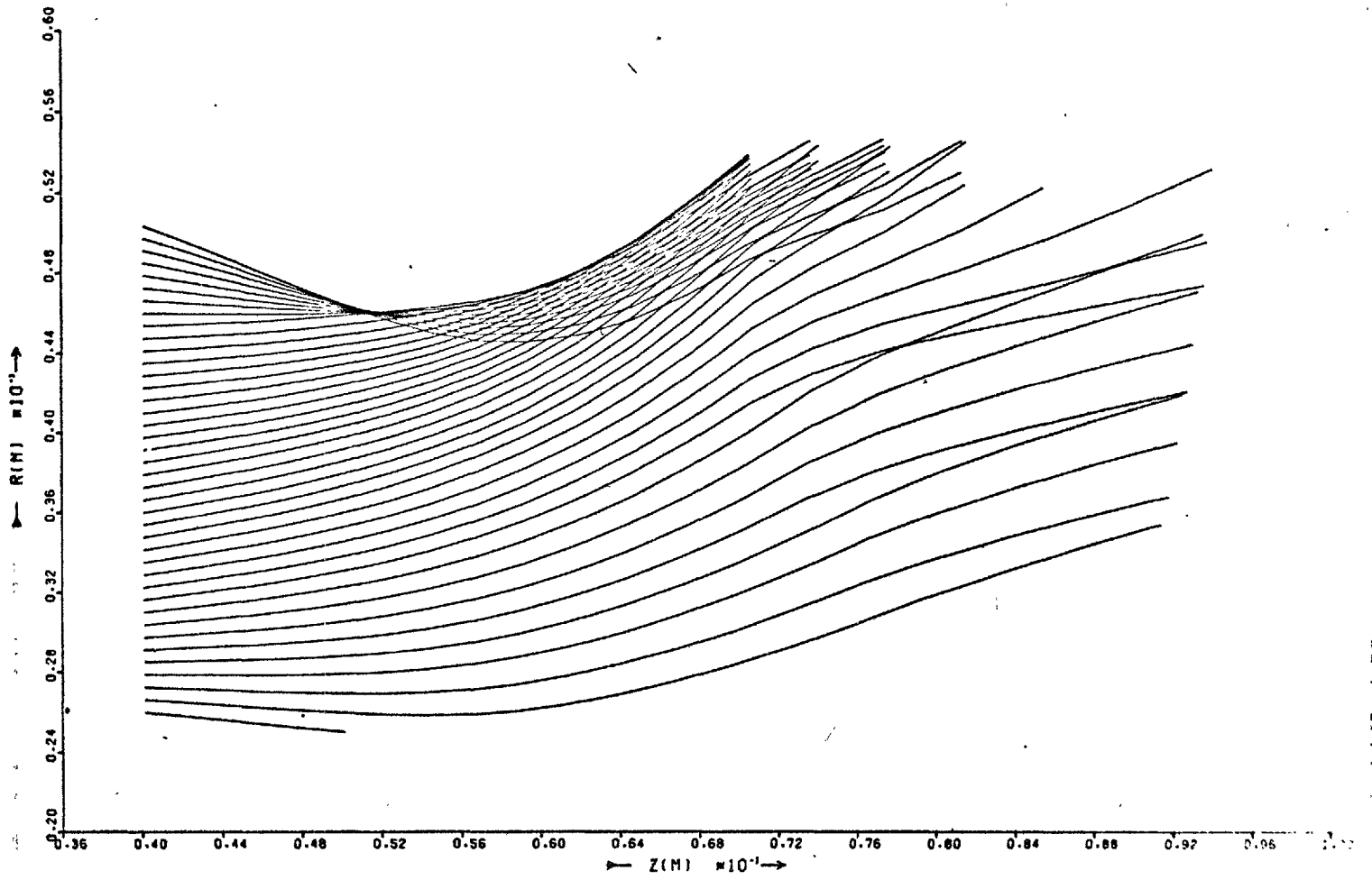

Fig.6.16

H^+ ions for voltage drop of 5 kV in 6-stage device. The ions are created at the anode. E_r fields are included

6.14 RECAPITULATION

The calculations in the earlier part of this chapter show the importance of the axial magnetic field region, the radial electric field and the ionization region. These quantities were either computed or measured directly. In this way comparison of the ion trajectory approach and experiment is possible. There is good qualitative agreement. Wall impact of ions is shown to be important, and this may account for the difference in behaviour of the two stages as already observed. Only second stage ions are able to escape via the cathode aperture. In the first stage, the radial electric field causes the ion current to flow close to the wall.

However more detailed comparison of computed effects with experiment reveals some discrepancies. The broad radial ion flux profile of the experiment is not well described. This is thought to be due to charge exchange neutrals or the fast electric field fluctuations.

Calculations performed for the 6-stage device show that E_r fields associated with the strong B_z between stages may account for the poor efficiency and large beam divergence in this device.

CHAPTER VII

THE RÔLE OF THE NON-UNIFORMITIES

7.1 AZIMUTHAL INHOMOGENEITIES AND ASSOCIATED CURRENT FLOW

The theory of Rosa (Rosa, 1962) shows how inhomogeneities may significantly alter the electron conductivity perpendicular to B in an MHD generator plasma. A brief resumé of this work is here presented for the case of an inhomogeneity in the form of a streamer parallel to the applied electric field, as in Fig.7.1. For simplicity both ion motion and pressure gradients are neglected, so that the simple form of Ohm's law $\underline{j} = \sigma\underline{E} - \underline{j} \wedge \underline{\beta}$ can be used (where $\underline{\beta} = \underline{\omega}\tau = \frac{e\underline{B}}{m\nu}$). Since the model only permits y variation, $\nabla . \underline{J} = 0$ and $\nabla \wedge \underline{E} = 0$ become

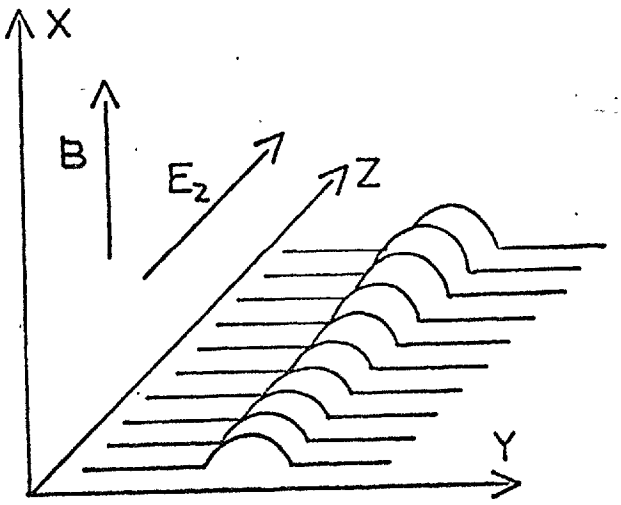

Fig.7.1
A streamer in the direction of E

$$\frac{\partial j_y}{\partial y} = \frac{\partial E_z}{\partial y} = 0$$

so that j_y and E_z are independent of y. The y and z components of Ohm's law then become

$$j_y = \sigma(y)\, E_y(y) - \beta(y)\, j_z(y) \qquad \ldots (7.1)$$

$$j_z(y) = \sigma(y)\, E_z + \beta(y)\, j_y \qquad \ldots (7.2)$$

The object is to obtain the y-averaged quantity $\langle j_z \rangle$, which is done by integrating (7.2) over y :

$$\langle j_z \rangle = \langle \sigma \rangle\, E_z + \langle \beta \rangle\, j_y \,. \qquad \ldots (7.3)$$

Substituting in (7.1) from (7.2) and integrating over y gives

$$j_y = - \frac{\langle \beta \rangle E_z}{\langle (1 + \beta^2)/\sigma \rangle} \qquad \ldots (7.4)$$

and hence

$$\langle j_z \rangle = E_z \left\{ \langle \sigma \rangle - \frac{\langle \beta \rangle^2}{\langle (1+\beta^2)/\sigma \rangle} \right\} . \qquad \ldots (7.5)$$

For electron-neutral collisions dominant, and for a non-uniformity in density, β is constant. In this case (7.5) becomes

$$\langle j_z \rangle = E_z \left\{ \langle \sigma \rangle - \left(\frac{\beta^2}{1+\beta^2} \right) . \frac{1}{\langle 1/\sigma \rangle} \right\} .$$

For a severe density variation, $\langle 1/\sigma \rangle$ can be large, so that $\langle j_z \rangle \sim E_z \langle \sigma \rangle$. Here the cross-field conduction in the density peak is restored to the $B = 0$ value by the $\underline{E}_y \wedge \underline{B}_r$ driven currents. A similar increase above the cross field conductivity, $\sigma/(1+\beta^2)$, can arise for a more general inhomogeneity.

It has already been shown in section 3.4 that $\underline{E}_\theta \wedge \underline{B}$ effects associated with the spoke account for a large fraction of the discharge current at these times. Similar fluctuation driven currents are discussed in section 4.5 for the main discharge phase.

7.2 THE INTERACTION BETWEEN A PLASMA AND NEUTRAL GAS

To summarise the measurements already presented, the spoke consists of a high density ($n_e \sim 10^{19}$ m^{-3}), current carrying region of cool ($T_e \sim 1.5$ eV) plasma moving azimuthally in the direction of $\underline{E}_z \wedge \underline{B}_r$ in the first stage with velocity $v_\theta \sim 30$ km/s through a background of neutrals ($N \sim 10^{21}$ m^{-3}).

There are many experimental devices in which a plasma moves perpendicular to a magnetic field through a dense neutral background (Lehnert Review, 1971). The discharge in a homopolar generator, in which a radial current is passed across an axial magnetic field, will often exhibit one or more azimuthally moving 'wheel spokes' of current. It is by analogy that the axial streamer here observed in a Hall accelerator is called a spoke, though this is a misnomer. All these devices exhibit the critical

velocity phenomenon, postulated by Alfven (1954, 1960) in relation to theories on the evolution of planetary systems. This proposes that at a certain relative velocity between plasma and neutral gas, ionization produces strong coupling which limits the relative velocity to :

$$|v_i - v_N| = \left(\frac{2\,e\,E_I}{M}\right)^{\frac{1}{2}} \qquad \ldots (7.6)$$

where E_I is the ionization energy of the neutral of mass M. This gives 52 and 39 km/s for H^+ and H_2^+. Sherman (1973) reviews many theories concerning this phenomenon and concludes that there is no single approach which will deal with all the evidence from a wide range of experiments.

7.3 FURTHER MEASUREMENTS ON THE SPOKE

The Hall accelerator differs from many of these experiments in that it has a large ion Larmor radius, a changing magnitude and direction of $\underline{E} \wedge \underline{B}$ and a different geometry. Thus it was thought worthwhile to examine the spoke here in more detail.

Firstly the accelerator was operated in different gases, and although hydrogen gives the clearest spoke, they were also observed in helium and argon. The azimuthal spoke terminal velocities were 30 km/s (H), 16 km/s (He), and 7 km/s (Ar), compared to velocities 52 km/s (H), 39 km/s (H_2), 35 km/s (HeI), 52 km/s (HeII), and 8.9 km/s (AI) predicted by equation (7.6). The results for H and A lie within ~30% of the prediction assuming H_2^+ and A^+ ions dominate. The agreement is poor for Helium, possibly due to the small amplitude in this case. However, there is a magnetic field dependence of the observed

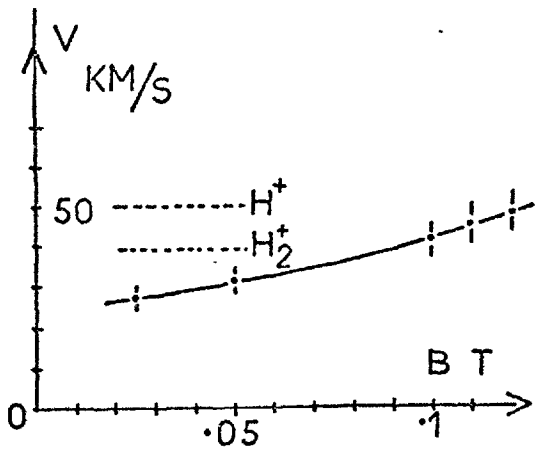

Fig.7.2
The magnetic field dependence of spoke velocity in hydrogen. Also shown dotted are the Alfven limits for H^+ and H_2^+

terminal velocity, as illustrated for hydrogen in Fig.7.2, and this is not predicted by the Alfven postulate.

Azimuthal neutral hydrogen Doppler shift measurements were made by performing a line scan with alternating B field polarity. Typical results, Fig.7.3, put an upper limit $v_{\theta N} \sim 6 \pm 3 \times 10^3$ m/s on neutral motion, considerably less than the spoke velocity. This is surprising in the light of the short exchange mean free path ($\sim$ 5 mm) for ions, since one would expect the $j_z \wedge B$ momentum input to the ions to impart a neutral velocity given by

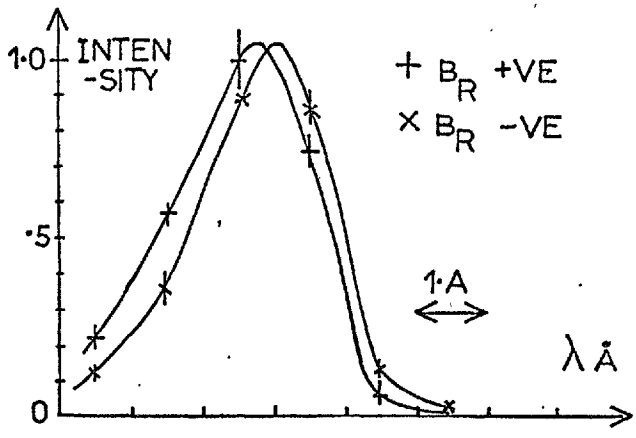

Fig.7.3
The azimuthal line of sight profiles of H_α during the spoke with different field polarities

$$v_{zN} \frac{d}{dz} N m v_{\theta N} = j_z \wedge B$$

where the azimuthal momentum is convected away axially. However for low neutral flow velocities, $\sim 2 \times 10^3$ m/s, this gives $v_{\theta N} \sim 40$ km/s by 1 cm from the anode, much larger than that observed. The difference could be due to wall impact of neutrals, since the neutral-neutral mean free path is long ($\sim$ 5 cm).

Petschek has proposed a spoke model (Lehnert, 1971; Sherman 1973) which predicts a critical velocity effect by balancing energy and momentum by ionization of stationary neutrals:

$$\underline{v}_\theta \cdot (\underline{j} \wedge \underline{B})_\theta = \left(e E_I + \frac{m v_\theta^2}{2} \right) \frac{dn_i}{dt}$$

and

$$j_z B_R = m v_\theta \frac{dn_i}{dt}$$

which together give

$$\tfrac{1}{2} m v_\theta^2 = e E_I .$$

However this is not consistent with two experimental observations. Firstly the plasma density in the spoke peak is roughly constant in time.

Secondly, the spectroscopically determined ionization rate $R = 10^{24}\,m^{-3}\,s^{-1}$ for atoms is insufficient to balance the momentum equation

$$mv_\theta \frac{dn_i}{dt} \sim 4.8\times10^{1}\ kgm/m^2\,s^2$$

and

$$j_z B_r \sim 7.6\times10^{3}\ kgm/m^2 s^2$$

both to within a factor ~ 2. Unless molecular ionization is ~ 100 times larger, which is unlikely since atomic and molecular densities are similar, then this model is inappropriate.

7.4 MECHANISMS FOR INSTABILITY

7.4.1 Streaming Instability

It has been suggested that an instability can arise due to the $\underline{E}\wedge\underline{B}$ drift of electrons (Buneman, 1962) and this has been applied to a slow ~ 50 kc/s mode in argon (Lary, Meyerand and Salz, 1963) and to a fast mode in Argon (Morozov, 1972) for very low current discharges (0.3A and ~ 2 amp respectively).

Buneman predicts an electrostatic mode of frequency ω_{ce} or ω_p if the electron $\underline{E}\wedge\underline{B}$ drift exceeds $\sim\left(\frac{kT_e}{m_e}\right)^{\frac{1}{2}}$, the electron thermal velocity. However in the experiment treated in this thesis, $\frac{\underline{E}\wedge\underline{B}}{B^2}$ velocities are in the range 5×10^4 to 2×10^5 m/s, whereas electron thermal velocities are in excess of $\sim 4\times10^5$ m/s for $T_e \gtrsim 1$ eV, suggesting that this instability should not be excited. Lary et al state that the criterion for instability should be $\frac{E}{B} > \left(\frac{kT_i}{m_e}\right)^{\frac{1}{2}}$ where T_i is the ion temperature. However, in the present experiment, this would require $T_i < 0.3$ eV, whereas measurements show an atom temperature $\sim$ few eV and the short ion-neutral mean free path would suggest $T_i \sim T_a$. Streaming would not explain the rôle of the neutrals, nor the empirical relation (7.6) (the Alfven limit).

7.4.2 The Electrothermal Theory

The electrothermal theory has already been applied successfully to the streamer instability observed in seeded gas MHD generators. (Nelson

and Haines, 1969; Uncles, 1972). In these devices, a low temperature partially ionized plasma flows perpendicular to a magnetic field. If $\omega\tau$ is large, the transverse current flows in channels between the electrodes, rather than uniformly. These channels arise because the enhanced local Ohmic heating in the higher density regions is not balanced by increased energy loss, but produces a temperature rise and, by ionization, a further increase in density. This has a deleterious effect on performance because of the increased internal resistance of the generator.

There are several similarities between Hall accelerator and MHD generator and the observed instabilities in each, which make it worthwhile examining the electrothermal theory as it might be applied in the former case. In both devices a transverse current interacts with a flowing partially ionized plasma in a magnetic field, in one case accelerating and in the other retarding the flow. In the MHD generator it is desirable to have a high electron temperature (relative to the temperature of the heavy particles) in order to increase ionization and hence the conductivity, and this can be achieved by magnetically induced non-equilibrium elevation of electron temperature if the Hall parameter $\omega\tau \geqslant 1$ (Haines and McNab, 1974). The elementary theory of Chapter I and the measurements of Chapter IV show that $\omega\tau \gg 1$ in the Hall accelerator. In both cases the electron temperature, T_e, is much less than the ionization energy E_I, so that ionization balance ensures that the electron density is very sensitive to variations in T_e.

Nelson and Haines (1969) have performed a linear analysis of the waves in a seeded partially ionized gas, and a summary of their conclusions is presented here. Firstly, they find two electrothermal modes, a fast thermal mode which is severely damped, and a lower frequency ionization mode which is unstable under certain conditions. The maximum growth rate of the ionization wave occurs, for wave vector $\underline{k}$, at an angle

$$\alpha = \sin^{-1} \frac{(\underline{j}_o \wedge \underline{k}) \cdot \underline{B}}{j_o k B}$$

to the unperturbed current, j_o, given by $\alpha = \pi/4$, and for wavelengths $\sim$ few cm. There is a critical value of $\omega\tau$ below which both modes are stable, and above this the range of α for unstable modes increases corresponding to a transition from plane waves to random turbulence. The density perturbation does not convect with the electrons because the heavy particles are assumed not to move during the wave motion. However, ionization and recombination on the wings of the density perturbation cause the region to move either parallel or anti-parallel to the electron streaming.

There are differences however between the Hall accelerator and MHD plasmas which prevent these results being applied directly to the Hall accelerator in hydrogen. The ionization and recombination rates are different, two ion species exist (H^+ and H_2^+) and Saha equilibrium is inapplicable. This makes the electron temperatures of interest an order of magnitude higher at $\sim$ few eV. The electron collision cross-sections are different, as are the relative importances of neutral and ionic collisions. The energy balance mechanism, discussed in Chapter IV are also different. Finally, the low heavy particle density and large magnetic forces make the neglect of heavy particle effects difficult to justify. For these reasons the Nelson theory is here completely re-worked and extended to meet these points.

7.5 THE ELECTROTHERMAL THEORY FOR H_2^+/H_2 AND H^+/H PLASMAS

Here the heavy particles are assumed uniform with a common velocity and low temperature. They only enter the problem by the quasi neutral requirement $n_i \simeq n_e$, since it is assumed that heavy particle properties change only slowly compared to times of interest. Plasma generated magnetic fields are neglected in comparison with the imposed $\underline{B}$.

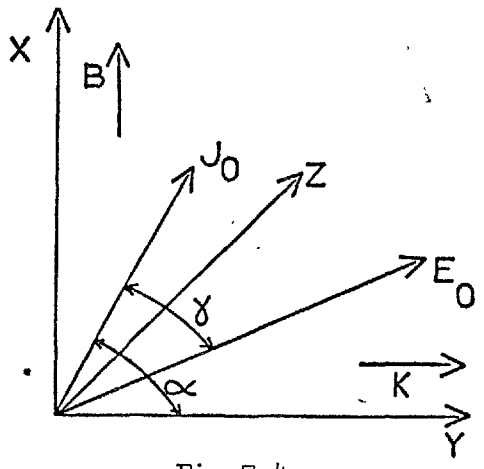

Fig.7.4
The steady state current, j_o, and field, E_o, lie in the z-y plane. The y coordinate is aligned with the wave vector $\underline{k}$. The magnetic field lies along x

The coordinate system chosen (Fig.7.4) is similar to others used in this thesis where the current flows in the y-z plane. This differs from those often chosen for MHD work. Considering the motion of electrons only, the equations which describe the system are:

Electron conservation: $$\frac{dn}{dt} = NnS - n^2\alpha \qquad \ldots (7.8)$$

Electron equations of motion: $j_z = -nev_z$

and $j_y = -nev_y$ $\qquad \ldots (7.9)$

Charge conservation $\nabla \underline{j} = 0$

Electron energy equation:

$$\frac{\partial}{\partial t}(nkT) - \frac{\partial}{\partial z}\left(\frac{3kT}{2}\cdot\frac{i_z}{e}\right) - \frac{\partial}{\partial y}\left(\frac{3kT}{2}\cdot\frac{i_y}{e}\right) - nkT\left\{\frac{\partial}{\partial y}\frac{i_y}{ne} + \frac{\partial}{\partial z}\frac{i_z}{ne}\right\}$$

$$= \frac{j^2}{\sigma} - 3nkT\nu\frac{m_e}{m_i} - \frac{dn}{dt}eE_I - \frac{5}{2}\frac{nk^2T^2}{m\nu L^2} \qquad \ldots (7.10)$$

Ohm's law: $$j_y/\sigma = E_y - j_zB/ne$$
$$j_z/\sigma = E_z + j_yB/ne \qquad \ldots (7.11)$$

and Faraday's law: $\nabla \wedge \underline{E} = 0$. $\qquad \ldots (7.12)$

This treats the frame of the ions, where there is no ion current. The ionization and recombination coefficients are chosen for a particular plasma/neutral mixture. The electron energy equation includes a term with a spatial scale length L to account for electron thermal loss along B_x to the walls, which is found experimentally to be the major electron energy loss.

The spatially uniform steady state solution is chosen:

$$\left.\begin{aligned} NS &= n_o \alpha \\ j_{yo} &= \sigma_o E_{yo} - j_{zo}\, \sigma B/n_o e \\ j_{zo} &= \sigma_o E_{zo} + j_{yo}\, \sigma B/n_o e \\ j_o^2/\sigma &= 3nkT\, \nu m_e/m_1 + \frac{5}{2}\, \frac{nk^2T^2}{m_e \nu L^2} \end{aligned}\right\} \quad \ldots (7.13)$$

Here the ionization balance need not be Saha equilibrium at the electron temperature. The Ohm's law components define the angle between j_o and E_o to be $\gamma = \tan^{-1}\beta$ as is shown in Fig.7.4. For a given orientation α, a single parameter will specify the solution to (7.13).

The steady state is perturbed in the form $n = n_o + n^1 \exp(i\omega t - ky)$, i.e. plane waves of wave-vector $\underline{k}$ in the y direction. Products of the small perturbations n^1 etc. can be neglected. The neutral density is taken large so that $n^1 = -N^1 \ll N_o$. Faraday's law and charge conservation become $\underline{k} \wedge \underline{E}^1 = 0$ and $\underline{k} \cdot \underline{j}^1 = 0$, so that the perturbed electric field is in the wave direction, and the perturbed current flows along z.

The perturbed Ohmic heating can be expressed:

$$\left(\frac{j^2}{\sigma}\right)^1 = \frac{j_o^2}{\sigma}\left\{\frac{n^1}{n_o}\left(2\sin^2\alpha - 1 - 2\,(\sin\alpha\cos\alpha)\,\beta\right) + \frac{\nu^1}{\nu}\,(1 - 2\sin\alpha)\right\}$$

where $\sigma = \frac{ne^2}{m\nu}$ and ν^1 represents the perturbed collision frequency. $\beta = \omega\tau$. Thus for the special case of a density perturbation such that $\frac{n^1}{n} \gg \frac{\nu^1}{\nu}$, there is increased Ohmic heating for large β and a maximum for $\alpha = \frac{3\pi}{4}$, i.e. the same orientation of 45° between current and wave direction predicted by Nelson (Nelson and Haines, 1969). Perturbation of the electron energy equation gives rise to an equation in perturbed density and temperature:

$$\frac{n^1}{n_o}\,(A\omega + B) + \frac{T^1}{T_o}\,(C\omega + D) = 0 \qquad \ldots (7.14a)$$

where A, B, C, D are coefficients dependent only on the steady state conditions and k.

The ionization balance may be perturbed to give an equation:

$$\frac{n^1}{n_o}(E\omega + F) + \frac{T^1}{T_o} G = 0 \qquad \ldots (7.14b)$$

where E, F and G depend upon the plasma composition.

Case (i) Atomic H^+/H Plasma

At the densities and temperatures of interest, $n_e \leqslant 10^{20}\ m^{-3}$ and $T_e \leqslant 13.6$ eV, the electron impact ionization is not balanced by 3-body recombination since the density is too low. Instead recombination is radiative with recombination coefficient $\alpha \simeq 2.7\times10^{-19}/T^{\frac{3}{4}}\ m^3 s^{-1}$ (Hinnov and Hirshberg, 1962). The perturbed density equation can be written:

$$\frac{n^1}{n}(i\omega + NS) - \frac{T^1}{T}\left(\frac{13.6}{T} + \frac{3}{4}\right) NS = 0 ,$$

and so for low frequency fluctuations,

$$\frac{n^1/n}{T^1/T} \sim \left(\frac{13.6}{T} + \frac{3}{4}\right) .$$

Thus for $T \ll 13.6$ eV, a small temperature perturbation will produce a large density perturbation, making the system sensitive to changes in the heating.

Case (ii) Molecular H_2^+/H_2 Plasma

Here, although ionization is very similar to the atomic case, the dominant loss process for ions is dissociative recombination, as mentioned in section 4.8. Though equation (7.8) still applies for the electrons and ions if $\alpha = \alpha_{DR}$ the dissociative recombination coefficient, the neutral conservation equations are:

$$\frac{dN_{H_2}}{dt} = - n_e N_{H_2} S_{H_2} \quad \text{and} \quad \frac{dN_H}{dt} = n_e^2 \alpha_{DR}$$

where the subscripts denote the neutral species, and where molecular recombination and electron collisional atomisation have been neglected. The molecular neutrals will be depleted in a time $t \sim N_{H_2}/(n_e^2 \alpha_{DR})$ if ionization steady state is approximately true. This time is typically 100 μs for $N \sim 10^{21} m^{-3}$ and $n_e \sim 10^{19} m^{-3}$, which is the spoke lifetime.

In this case the perturbed density equation is:

$$\frac{n^1}{n}(i\omega + NS) - \frac{T^1}{T}\left(\frac{13.6}{T} + \frac{1}{2}\right) = 0 .$$

For both cases perturbed energy and ionization equations can be combined to give a quadratic dispersion relation in ω with complex coefficients. This is solved numerically.

7.6 MODES IN AN ATOMIC HYDROGEN PLASMA

The ionization mode here is qualitatively similar to that discussed in Nelson (1969) as is shown by Fig.7.5 for $\omega\tau = \beta = 100$. The most unstable angle for this mode is $\alpha = \frac{3\pi}{4}$ as predicted in the previous section. However growth times ($\sim 10^{-3}$ s) and periods ($\sim 10^{-2}$ s) are longer than times of interest. These long times are a consequence of the steady state assumption, which gives a low T_e ($\leqslant 1$ eV) over a wide range of density. The long ionization time limits the growth of the mode. The temperature $T_e \sim 2$ eV seen experimentally give ionization rates $\sim 10^4$ times faster. Because of this poor steady state assumption, this mode is not considered further. The fast mode is much less temperature sensitive, and so the steady state assumption is still valid.

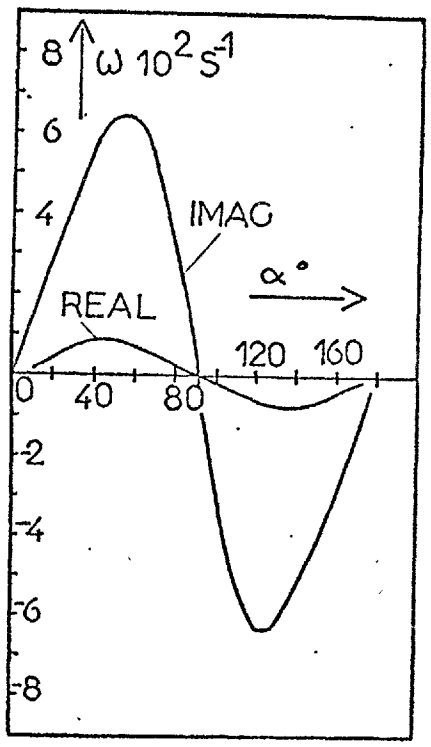

Fig.7.5
Complex frequency of ionization mode for various orientations, α, for $\omega\tau = \beta = 100$. Atomic hydrogen $\lambda = 25$ cm

Interestingly, the fast thermal mode is found to differ from the Nelson and Haines mode. It can be seen in Fig.7.6, which displays the growth of this mode for the two cases $\omega\tau = \beta = 10$ and 100, that it is possible for this fast mode to

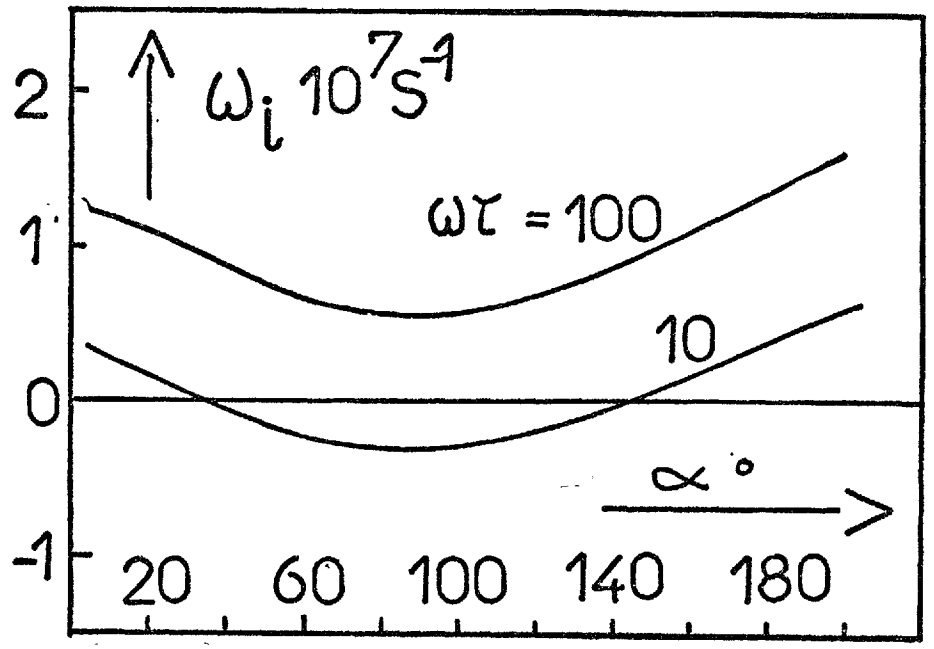

Fig.7.6
Imaginary part of complex frequency of fast mode (i.e. damping rate) against orientation for $\beta = \omega t = 100$ and 10. The latter gives instability over the range $\alpha = 35°$ to $145°$

become unstable at the higher densities. Maximum growth occurs for $\alpha = \pi/2$, i.e. for wave vectors perpendicular to the unperturbed current. The real frequency is $\omega_r \simeq - \frac{k j \cos\theta}{ne}$, where the dominant terms in the electron energy equation are those in perturbed temperature. The mode frequency ($\omega_r \sim 10^7 s^{-1}$) is fast compared to the ionization time ($\sim$1 ms), and so only temperature fluctuations are possible, and these are convected with the electron stream. However the maximum growth occurs when $\omega_r = - \frac{k j \cos\pi/2}{ne} = 0$, and the fluctuation is nearly stationary. Thus the physics can be studied by looking at the real part of the perturbed energy equation

$$- \omega_i \frac{3 n k T^1}{2 T} = - \frac{j_o^2}{\sigma} (1 - 2 \sin\alpha) \frac{3T^1}{2T} + 3 n k T \nu \frac{m_e}{m_i} \frac{T^1}{2T} - \frac{2.5 n k^2 T^2}{m_e \nu L^2} \cdot \frac{7 T^1}{2 T} \quad \ldots (7.15)$$

where $\omega = \omega_r + i\omega_i$ and $\nu^1 = - \nu \frac{3T^1}{2T}$. In the limit where either collisional cooling or thermal conduction losses dominate, the damping rate ω_i becomes either

$$\omega_i = \frac{j_o^2}{\sigma} \left\{1 - 3 \sin \alpha\right\} / \frac{3}{2} nkT \qquad \ldots (7.16)$$

or

$$\omega_i = \frac{j_o^2}{\sigma} \left\{5 - 3 \sin \alpha\right\} / \frac{3}{2} nkT \qquad \ldots (7.17)$$

respectively. As can be seen, for the former case, instability occurs over the range of orientations for which $3 \sin \alpha > 1$, whereas for the latter damping occurs for all orientations. Comparison of the terms show that thermal conduction dominates if $\frac{5 \times 10^{20} n_e}{T^2} \leqslant 1$ and electron-ion collisional cooling dominates if this is greater than 1. Hence for $\beta = 100$ ($T_e = 0.7$ eV , $n_e = 2.5 \times 10^{18}$, $N = 10^{21}$ m^{-3}) thermal conduction dominates so the fast mode is always stable , whereas for $\beta = 10$ ($T_e = 0.8$ eV , $n_e = 3 \times 10^{19}$ m^{-3}. $N = 10^{21}$ m^{-3}) ion collisional cooling dominates, and the fast mode gives rise to stationary streamers along j_o. For high neutral densities such that electron-neutral collisions dominate, both loss mechanisms are always able to compensate for perturbations in the Ohmic heating, so that the fast mode is then always damped - this is the case treated by Nelson for MHD generators. However, the experimental results of Chapter IV show that Coulomb collisions dominate, except close to the anode, during the main discharge phase. Hence it seems eminently possible that the fast fluctuations observed there are a manifestation of these stationary heating modes. The equations (7.17) and (7.16) do not include wavelength effects, though cross field electron thermal conduction might be expected to damp short wavelengths for which $k \geqslant \frac{2\pi(1 + \beta^2)}{L}$ (L = channel width). This broad range of wavelengths and orientations for growth may account for the random appearance of the observed fluctuations.

7.7 MODES IN A MOLECULAR HYDROGEN PLASMA

Comparison of the two perturbed density equations for the cases of atomic and molecular hydrogen in sections 7.5.1 and 7.5.2, show that they are identical in form if $T \ll 13.6$ eV . In other words the temperature

dependence of the recombination coefficient is negligible in comparison with the strong dependence of the ionization rate and the effect of the large dissociative recombination rate appears only through the steady state, where, for a given density, a higher temperature is permitted. For a molecular plasma the ionization balance for $n_e = 10^{19} m^{-3}$ occurs at $\sim 2.5\,eV$ rather than $0.8\,eV$ for an atomic plasma (for $N = 10^{21}$). This causes the exponential to increase the ionization rate by a factor

$$\frac{e^{13.6/0.8}}{e^{15.4/2.5}} \sim e^{10.8} \simeq 5.1 \times 10^4$$

and shorten the ionization time to $\sim \mu s$.

Figure 7.7 illustrates the angular dependence of the two modes for the particular case $n_e = 1.0 \times 10^{19}\ m^{-3}$, $T_e = 2.5\,eV$, $B = 0.1\,T$ and wavelength $\lambda = 10\,cm$. Both modes have complex frequencies of a similar magnitude so that the distinction between the fast thermal mode and the ionization mode is not clear cut. A maximum growth rate of $4 \times 10^7\ s^{-1}$ occurs at $\alpha = 3\pi/4$, corresponding to a frequency ~ 50 kc/s. The wavelength dependence of the growth rate shows a transition from a heating mode to an ionization wave depending on wavelength. Shortening the wavelength below $\sim 5\,cm$ causes a reduction in growth rate and a shift in the orientation of the fastest growing mode towards smaller α, (Figs.7.8 and 7.9) until at $\lambda \sim$ mm the maximum growth time is $\sim$ ionization time, and occurs at $\alpha \simeq \pi/2$.

At the longer wavelengths, the high frequency ensures, from the ionization balance, equation (7.14b), that

$$\frac{n^1}{n_o} \Big/ \frac{T^1}{T_o} = -\frac{G}{E\omega + F}$$

becomes small, so that fluctuations occur in the temperature. In order to satisfy the perturbed energy equation, (7.14a), $C\omega + D \to 0$, the real frequency is given by the convective term $\omega_r \sim \frac{3k}{2} ne T v_{eo}$, and the growth time is the heating time, which can be fast. Now as $\lambda \to 0$, or $K \to \infty$,

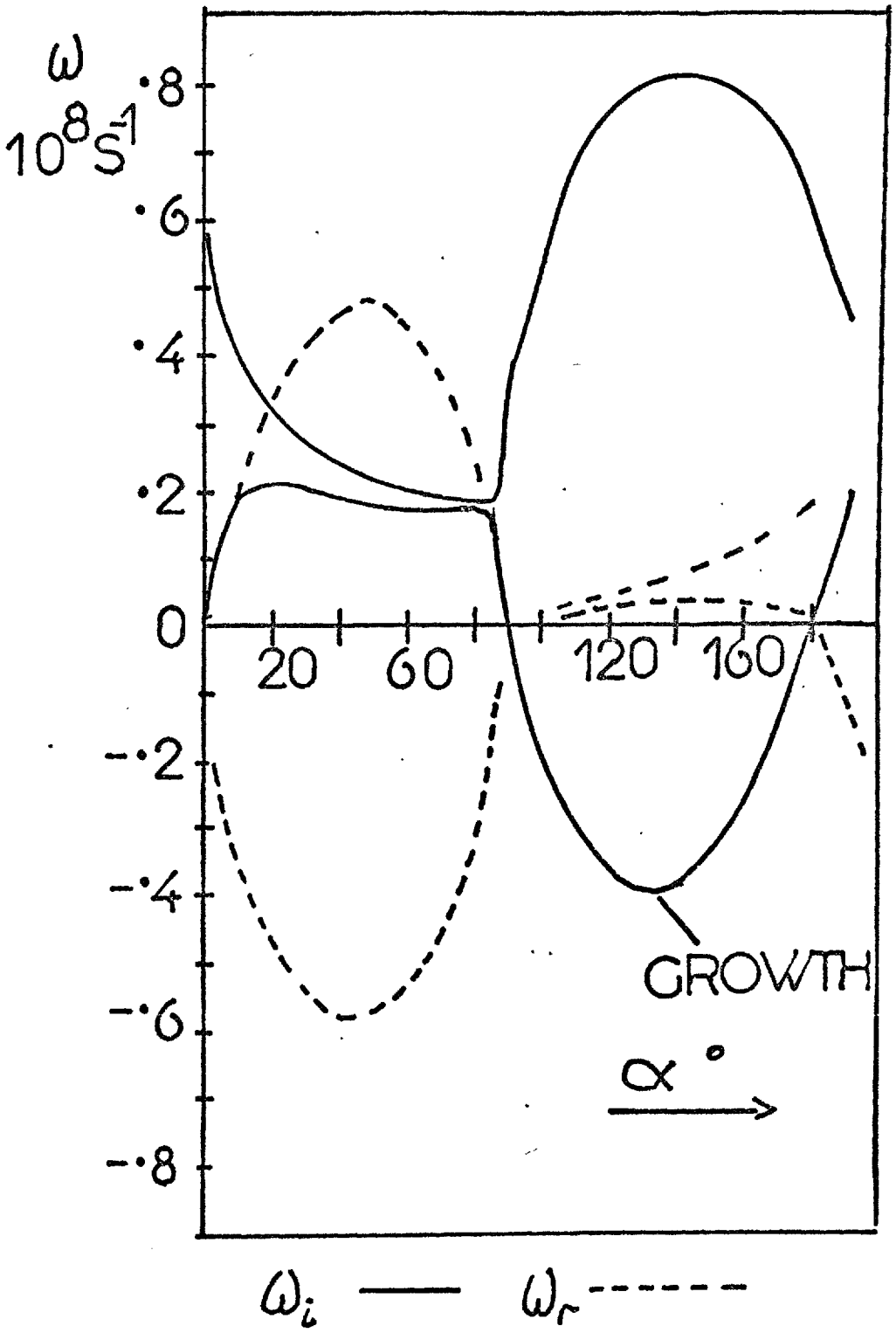

Fig.7.7
Molecular hydrogen plasma. Complex frequency against orientation α. λ = 10 cm, β = 120. Peak growth $\omega_g \sim 4 \times 10^7\ s^{-1}$ at $\alpha \simeq 140^\circ$

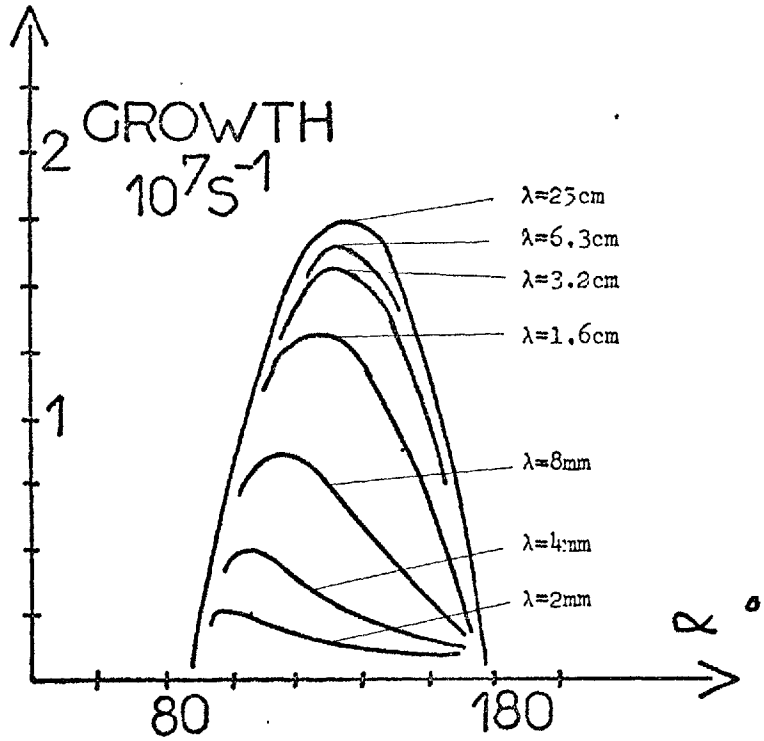

Fig.7.8
Growth rate (ω_g) against orientation showing shift toward $\alpha = 90$

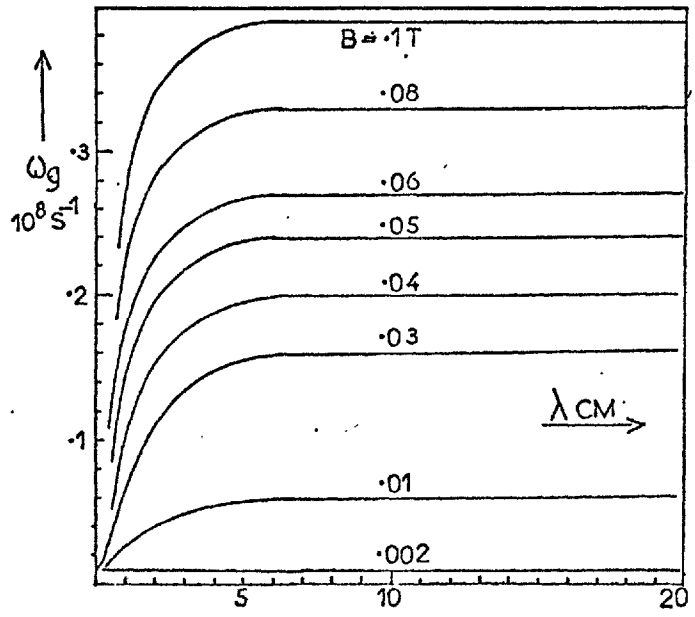

Fig.7.9
Maximum growth of ionization mode as a function of wavelength for various magnetic fields B. Molecular plasma. $T_e = 2.5$ eV, $n_e = 10^{19}$ m^{-3}

the convective and compressive terms dominate the electron energy equation:

$$\frac{n^1}{n_o}\left(i\omega ne E_I - ikTj\cos\alpha\right) + \frac{T^1}{T_o}\left(i\omega\frac{3neT}{2} + \frac{3ikT}{2}j\cos\alpha\right) = 0 \qquad \ldots (7.18)$$

Hence $\frac{n^1}{n_o} \sim \frac{T^1}{T_o}$ so that the ionization balance (7.14b) sets the growth rate to the ionization time. However, as $\alpha \to \frac{\pi}{2}$ these convective terms disappear, and the growth rate again becomes the heating rate as for large λ. For this reason the maximum growth shifts towards $\alpha = \frac{\pi}{2}$ for shorter wavelengths.

Unlike the Nelson and Haines theory, there is no critical value of $\omega\tau$ below which both modes are damped, because the density fluctuation is never sufficiently strong to dominate the perturbed Ohmic heating at low $\omega\tau$. Nevertheless, the growth rate does fall to a low value for $\omega\tau \leqslant 2$ as shown in Fig.7.10.

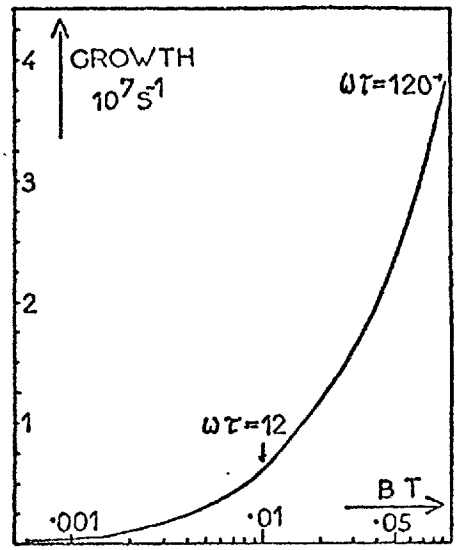

Fig.7.10
Dependence of growth rate of ionization mode for molecular plasma on magnetic field B, and hence upon $\omega\tau$. $n_e = 10^{19}$ m^{-3}, $T_e = 2.5$ eV

Fig.7.11 compares the phase velocity of the wave (for $n = 10^{19}$ m^{-3}, $T_e = 2.5$ eV) with the rotational velocity of the spoke, at various field strengths and in the limit of long and short wavelengths. The agreement within a factor ~ 2 is remarkable in light of the large amplitude of the experimental wave and the neglect of the ion motion effects in sections 7.3 and 7.4. The wave travels in the same direction as the electrons in both theory and experiment, and at an angle between $\pi/2$ and $3\pi/4$ with the current density.

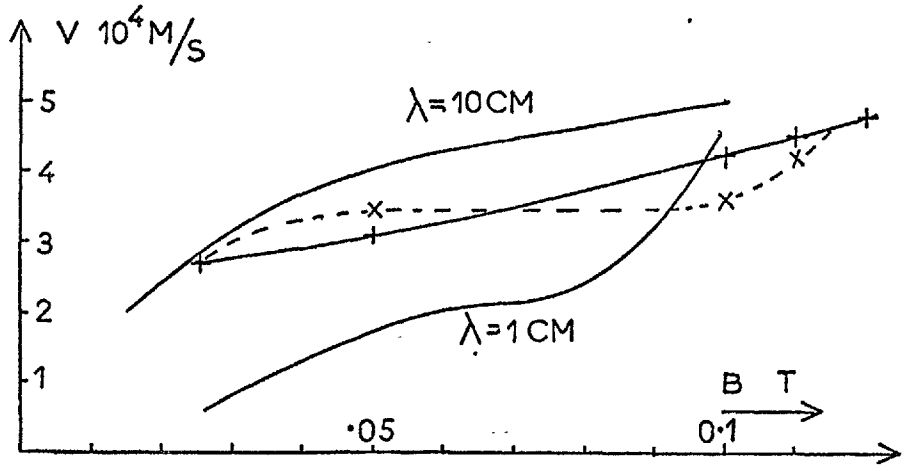

Fig.7.11

Wave phase velocity as a function of B for $\lambda = 1$ and $\lambda = 10$ cm compared to experimental spoke velocity at 100μs (+) and 20μs (x). $n_e = 10^{19}\ m^{-3}$, $T_e = 2.5$ eV

7.8 THE SIGNIFICANCE AND LIMITATIONS OF THE THEORY

The extension to electrothermal theory presented here demonstrates, for a molecular hydrogen plasma, growth at phase velocities (10 - 50 km/s) and wavelengths (1 - 25 cm) similar to those observed experimentally. The fast growth rate (~250ns) suggests that the observed growth in amplitude arises from changes in the non-linear saturation amplitude due to the slowly rising bank current. The observed spoke lifetime is similar to the timescale for molecular dissociation by the fast process of dissociative recombination. It is certainly possible that the observed mode after this time is the fast heating mode for the atomic plasma of frequency 2 mc/s at $\lambda = 1$ cm and 20 mc/s at $\lambda = 1$ mm and growth time 0.3 μs. The predicted broad spread of orientations $\left(\frac{\pi}{6} \leqslant \alpha \leqslant \frac{5\pi}{6}\right)$ is consistent with the random character of these fluctuations.

Thus electrothermal theory seems able to account for both observed fluctuation modes, and the non-uniformities will give rise to the increased cross-field electron current on the large amplitude theory of Rosa (1962). However a nonlinear treatment of these waves is required to predict

effective plasma conductivity. In addition the ion and neutral motions have not been included in this approach, and, since the ion transit time

$$t = \left(\frac{2L}{\frac{eE}{m}}\right)^{\frac{1}{2}} \sim 0.5\ \mu s$$

(where L = accelerator length $\sim 0.15\,M$, and $E = 10^4\,V/m$) is comparable with the wave frequencies, this is not justified. The inclusion of ions and neutrals is also required to treat the Alfven limit which is found, experimentally, to be applicable.

CHAPTER VIII

THE NON-LINEAR BEHAVIOUR OF SPOKES

8.1 INTRODUCTION

Several authors have reported fluid codes for plasmas in which the Hall terms are important (Kilkenny, 1972; Watkins, 1974; Uncles, 1972). The first two treat the r-z plane in cylindrical geometry, dealing with the cusp compression and acceleration phases of the Polytron toroidal Hall accelerator, and solve for the plasma motion in full. The work of Uncles, however, deals with a plane in Cartesian geometry, considering only the electrons in a partially ionized MHD generator plasma.

Chapter VII shows that electrothermal theory may account for the growth of a spoke like instability, but in order to answer the question of how these affect the acceleration, the numerical approach presented in this chapter is required. It is for this reason that the treatment of Uncles is considered inappropriate, since ion and neutral motions are assumed uniform, entering the problem only via $\underline{V} \wedge \underline{B}$ electric fields. However, interest lies in the behaviour in the plane perpendicular to B of a discharge between electrodes, as in the work of Uncles but unlike the work of Kilkenny and Watkins who describe an inductively driven discharge in the plane containing $\underline{B}$. Hence, although the work here presented shares features in common with these three fluid codes, the new code is sufficiently different to justify description in detail.

8.2 THE EQUATIONS FOR SOLUTION

The coordinate system used is the Cartesian system, illustrated in Fig.8.1. Electrodes are positioned on the $z = 0$ and $z = L_z$ boundaries and connected to an external circuit represented by L C R. In order to describe the cylindrical nature of the problem, but without the added

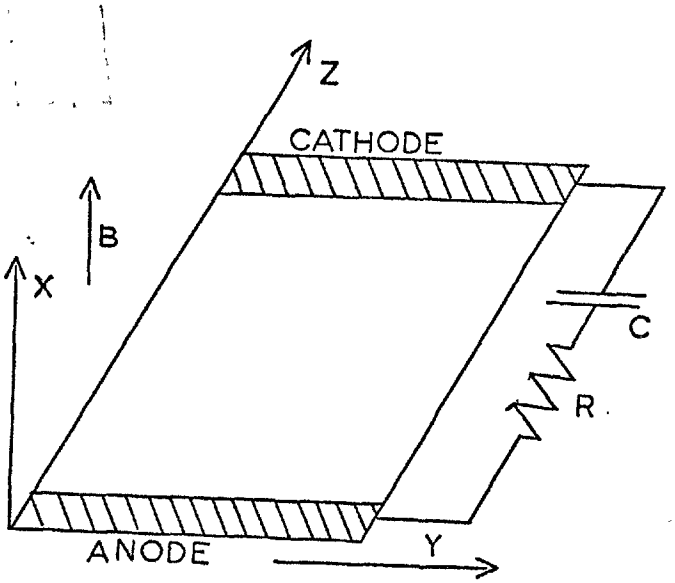

Fig.8.1
Coordinate system showing electrodes and external circuit. B is in the x-direction

complication of centrifugal effects, the boundaries at $y=0$ and $y=L_y$ are considered adjacent. The applied magnetic field is taken along x, and assumed to be much greater than fields due to the plasma currents.

The equations to be solved can be written down; firstly for the plasma continuity:

$$\frac{\partial n}{\partial t} + \nabla n\underline{V} = N n S - n^2 \alpha \qquad \ldots (8.1)$$

where S and α are the ionization and recombination coefficients. The plasma momentum equations are:

$$m_i \frac{\partial n\underline{V}}{\partial t} + m_i \nabla(n\underline{V}\,\underline{V}) = \underline{j} \wedge \underline{B} - \underline{K}^{in} - \nabla p + n N S m_N \underline{V}_N - n^2 \alpha m_i \underline{V} \qquad \ldots (8.2)$$

where m_i and m_N are the ion and neutral masses, and $\underline{K}^{in}$ represents the momentum loss per unit volume from ions to neutrals in collisions. $\underline{V}_N$ is the neutral velocity. The electron energy equation is:

$$\frac{\partial}{\partial t}\left(\frac{3nkT}{2}\right) + \nabla\left(\frac{5nkT\underline{V}}{2}\right) = \frac{j^2}{\sigma} - 3nkT\frac{m_e}{m_i}\left(\nu_{ei} + \nu_{eN}\right) - nNS\,E_I - \frac{5}{2}\frac{nk^2T^2}{m_e \nu L^2} \qquad \ldots (8.3)$$

where the terms on the right represent Ohmic heating, collisional loss to the heavy particles, the ionization energy, and the thermal conduction loss to the walls. ν_{ei} and ν_{eN} are the electron ion and electron-neutral collision frequencies. L is the scale length for thermal conduction along $\underline{B}$ to the wall, and is taken to be the wall distance. This equation is valid so long as the electron thermal velocity $\sqrt{\frac{kT}{m_e}} > \underline{V}$ the plasma velocity.

The equations for the current are the components of the generalized Ohm's law:

$$\frac{\underline{j}}{\sigma} = \underline{E} + \underline{V} \wedge \underline{B} - \frac{\underline{j} \wedge \underline{B}}{ne} + \frac{\nabla p}{ne} \quad . \qquad \ldots (8.4)$$

The neutral equations simply describe coupling to the ions via ionization and collisions, and can be written:

$$\frac{\partial N}{\partial t} + \nabla N \underline{V}_N = - nNS + n^2 \alpha \qquad \ldots (8.5)$$

$$\frac{\partial}{\partial t} N m_N \underline{V}_N + m_N \nabla \left(N \underline{V}_N \underline{V}_N \right) = \underline{K}^{IN} - Nn S m_N \underline{V}_N + n^2 \alpha m_i \underline{V} \quad .$$

To complete the set of equations, charge conservation and Faraday's law are added:

$$\nabla . \underline{j} = 0 \quad \text{and} \quad \nabla \wedge \underline{E} = 0 \qquad \ldots (8.6)$$

The ionization and recombination coefficients used are those discussed in Chapter VII. The heavy particle momentum exchange term $\underline{K}^{IN}$ is simply

$$K^{IN} = m n N (\underline{V} - \underline{V}_N) |\underline{V} - \underline{V}_N| \sigma \qquad \ldots (8.7)$$

for $m_i = m_N = m$.

The dominant cross-section σ is charge exchange for which $\sigma \simeq 3.0 \times 10^{-19}$ m^2 (for 100–500 eV ions – Oak Ridge tables).

8.3 THE EQUATION FOR THE POTENTIAL

The y and z components of Ohm's law can be written in the form of equations for j_y and j_z:

$$j_z = \frac{\sigma}{1+\beta^2} \left\{ E_z - V_y B + \frac{1}{ne} \frac{\partial p}{\partial z} + \beta \left[E_y + V_z B + \frac{1}{ne} \frac{\partial p}{\partial y} \right] \right\}$$

and

$$j_y = \frac{\sigma}{1+\beta^2} \left\{ E_y + V_z B + \frac{1}{ne} \frac{\partial p}{\partial y} - \beta \left[E_z - V_y B + \frac{1}{ne} \frac{\partial p}{\partial z} \right] \right\} \qquad \ldots (8.8)$$

where $\beta = \omega\tau$. Substitution in the equation of charge conservation, the application of Faraday's law and writing $\underline{E} = - \nabla \varphi$ gives an equation for the electrostatic potential φ:

$$\nabla^2\varphi + \frac{\partial\varphi}{\partial z}\left\{ - \frac{\partial\beta}{\partial y} + \frac{1+\beta^2}{\sigma}\left\{ - \beta\frac{\partial}{\partial y}\left(\frac{\sigma}{1+\beta^2}\right) + \frac{\partial}{\partial z}\left(\frac{\sigma}{1+\beta^2}\right)\right\}\right\}$$

$$+ \frac{\partial\varphi}{\partial y}\left\{ \frac{\partial\beta}{\partial z} + \frac{1+\beta^2}{\sigma}\left[\frac{\partial}{\partial y}\left(\frac{\sigma}{1+\beta^2}\right) + \beta\frac{\partial}{\partial z}\left(\frac{\sigma}{1+\beta^2}\right)\right]\right\}$$

$$- \frac{1+\beta^2}{\sigma}\left\{\frac{\partial}{\partial y}\left[\frac{\sigma}{1+\beta^2}\left(V_z B + \beta V_y B + \frac{1}{ne}\frac{\partial p}{\partial y} - \frac{\beta}{ne}\frac{\partial p}{\partial z}\right)\right]\right.$$

$$\left. + \frac{\partial}{\partial z}\left[\frac{\sigma}{1+\beta^2}\left(-V_y B + \beta V_z B + \frac{1}{ne}\frac{\partial p}{\partial z} + \frac{\beta}{ne}\frac{\partial p}{\partial y}\right)\right]\right\} = 0 \qquad \ldots (8.9)$$

which is a second order equation for φ of the form

$$\nabla^2\varphi + A\frac{\partial\varphi}{\partial z} + B\frac{\partial\varphi}{\partial y} + C = 0,$$

where the coefficients ABC are functions of position only. The electrodes may be inserted by solving this equation together with the condition that φ is uniform over the electrode surface, with a magnitude given by the circuit equation:

$$\varphi_{cath} = -\frac{Q}{C} + L\frac{dI}{dt} + IR \qquad \ldots (8.10)$$

where φ_{cath} is the cathode potential, Q is the charge on the condenser bank, and I is the total discharge current. The anode potential is set arbitrarily zero. The total current I is determined by integrating equation (8.8) across the discharge.

Equation (8.9) is solved iteratively using the method of successive over relaxation (Potter, 1972) on a mesh labelled as in Fig.8.2. In difference form, equation (8.9) may be expressed:

$$R_c = \varphi_c - \frac{1}{4}\left\{\varphi_N\left(1 - \frac{B_c\Delta}{2}\right) + \varphi_s\left(1 + \frac{B_c\Delta}{2}\right)\right.$$

$$\left. + \varphi_E\left(1 + \frac{\Delta A_c}{2}\right) + \varphi_w\left(1 - \frac{A_c\Delta}{2}\right) + C_c\Delta^2\right\} = 0 \qquad \ldots (8.11)$$

where the coefficients ABC of the equation (8.9) are evaluated at the centre point. Δ is the mesh spacing. The relaxation scheme employed is represented by

$$\varphi_c^{p+1} = \varphi_c^p + \Omega R_c^{p,p+1} \qquad \ldots (8.12)$$

where p denotes the iteration level, Ω is the relaxation factor, and R, the residue given by (8.11), is evaluated using the most recent values of φ_N, φ_S, φ_E, φ_W. Clearly, $\varphi_c^{p+1} - \varphi_c^p \to 0$ when $R_c = 0$ is satisfied, so that convergence gives rise to a solution of (8.11). The circuit equation, (8.10), is used to adjust the cathode potential every 10 steps, and in this way the final converged solution satisfies both (8.9) and the circuit equation (8.10). The relaxation parameter Ω is chosen to optimise convergence.

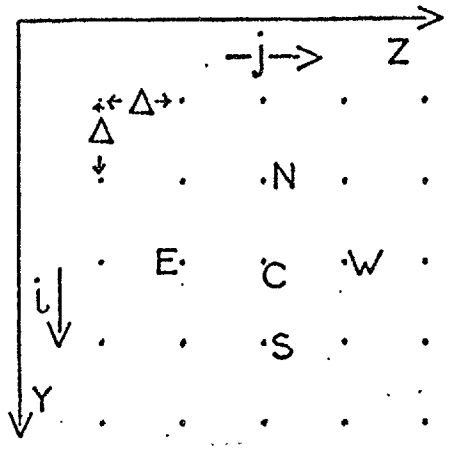

Fig.8.2
The mesh used for the potential solver. C indicates the central point which is surrounded by points N S E W

The numerical method and coding were checked by solving equation (8.9) for simple cases.

8.4 THE TIME DEPENDENT CALCULATION

The time dependent equations (8.1), (8.2), (8.3) and (8.5) are solved using the two interlocking meshes of the conservative Lax-Wendroff scheme (Potter, 1972). The mesh notation for this part of the calculation is illustrated in Fig. 8.3. The equations are expressed in the form:

$$\frac{\partial \epsilon}{\partial t} = C + \frac{\partial F_i}{\partial x_i} \qquad \ldots (8.13)$$

where ϵ is a conserved variable, F_i is a flux and C a source of this quantity. The Lax-Wendroff scheme calculates the value of ϵ at

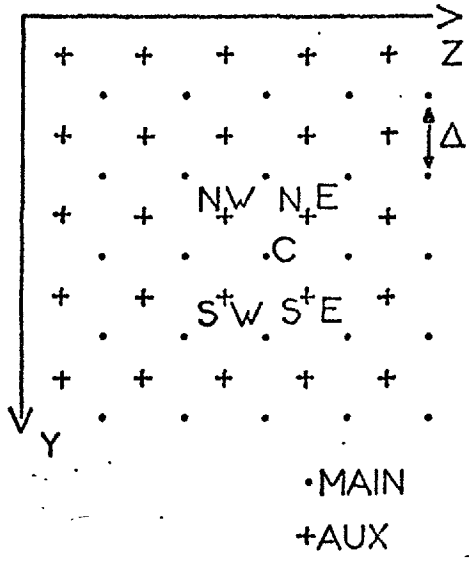

Fig.8.3
The main and auxiliary meshes for the time dependent calculation. The main point C is surrounded by auxiliary points NE, NW, SW, SE

the $\frac{1}{2}$ timestep $\delta t/2$ on the auxiliary mesh:

$$\epsilon^A = \frac{1}{4}\left(\epsilon^n_{NW} + \epsilon^n_{NE} + \epsilon^n_{SE} + \epsilon^n_{SW}\right) + \frac{\delta t}{8}\left(C_{NW} + C_{NE} + C_{SE} + C_{SW}\right)$$
$$+ \frac{\delta t}{4\Delta}\left(F_{Y_{SE}} + F_{Y_{SW}} - F_{Y_{NE}} - F_{Y_{NW}}\right)$$
$$+ \frac{\delta t}{4\Delta}\left(F_{Z_{NE}} + F_{Z_{SE}} - F_{Z_{NW}} - F_{Z_{SW}}\right) \qquad \ldots (8.14)$$

where all the quantities on the right are evaluated on the main mesh at time level n. The main step is then performed using the auxiliary variables to time-centre the method.

$$\epsilon^{n+1} = \epsilon^n + \frac{\delta t}{4}\left(C^A_{NW} + C^A_{NE} + C^A_{SE} + C^A_{SW}\right)$$
$$+ \frac{\delta t}{2\Delta}\left(F^A_{Y_{SE}} + F^A_{Y_{SW}} - F^A_{Y_{NE}} - F^A_{Y_{NW}}\right)$$
$$+ \frac{\delta t}{2\Delta}\left(F^A_{Z_{NE}} + F^A_{Z_{SE}} - F^A_{Z_{NW}} - F^A_{Z_{SW}}\right) \qquad \ldots (8.15)$$

where n denotes the time level, and the source and flux terms are evaluated on the auxiliary mesh. Notice that, as given, the source terms are averaged over the auxiliary mesh, thereby introducing some diffusion of the source. The numerical diffusion is not important unless the sources are strongly localized, and since the main mesh source term is not known at the half time level, this could only be removed by abandonment of the time centred approach.

The potential equation (8.9) is solved at every full time level on the main mesh. In order to save computing time, the auxiliary potential is found by interpolation in space.

As in all explicit schemes, for stability the timestep must be shorter than the shortest physical timescale contained in the equation. To avoid tedious analysis of the equation the timestep is determined by trial.

The boundary at $y = L_y$ is treated by taking the row of points outside to be those at $y = 0$. Thus quantities convected out of one

boundary reappear at the other and vice versa. The anode boundary is treated by considering free flow of plasma and neutrals into the system at thermal velocities. Gradients perpendicular to this boundary are set zero. Similarly at the cathode free convection out of the system is permitted by adding a row of points beyond the boundary, all identical in magnitude to the boundary points except for currents which are set zero. These conditions, and the treatment of the circuit equation, allow gradients in n_e etc. (but not φ) parallel to the electrode surfaces so that the current density is not constrained to be uniform at the surface.

8.5 THE POTENTIAL SOLUTION FOR LARGE $\omega\tau$

The experimental measurements already presented show that $\omega\tau$ is typically ~ 50 during the spoke phase of the discharge. For the case when $\underline{v} = 0 = \nabla p$, equation (8.9) can be written in the limit of large $\omega\tau$:

$$\nabla^2\varphi + \frac{\partial\varphi}{\partial z}\left\{-\frac{\partial\beta}{\partial y} - \left(\frac{1+\beta^2}{\sigma}\right)\beta\frac{\partial}{\partial y}\left(\frac{\sigma}{1+\beta^2}\right)\right\} + \frac{\partial\varphi}{\partial y}\left\{\frac{\partial\beta}{\partial z} + \beta\left(\frac{1+\beta^2}{\sigma}\right)\frac{\partial}{\partial z}\left(\frac{\sigma}{1+\beta^2}\right)\right\} = 0 \quad \ldots (8.16)$$

where $\beta = \omega\tau$ and in which the first derivatives may dominate. In this case the equation to be solved is very nearly first order for which the boundary conditions applied are inappropriate. Watkins (Watkins, 1974) discusses the application of the SOR scheme to second order equations with strong first order terms and shows that in such cases it may not be possible to choose a relaxation parameter Ω which will achieve convergence. It is found in practice that severe convergence problems arise in the solution for the potential for $\omega\tau \geqslant 5$. In order to circumvent this and yet still solve in the regime of plasma density and temperature of the experiment, it was found necessary to increase arbitrarily by a factor 10 the collision frequency in the potential part of the problem. The normal value was preserved in the temperature equation so as not to alter the energy balance. Unfortunately this precludes detailed comparison of the

experiment and code. These effects have not been a problem in the codes of Kilkenny, Watkins and Uncles, where the higher plasma densities give a Hall parameter $\omega\tau \leqslant 4$.

8.6 THE REMOVAL OF FAST HEATING MODES

It was found solving the complete set of equations 8-1 to 8-6 for an initial uniform plasma $n_e \sim 10^{19}\ m^{-3}$ and $T_e \sim 2\,eV$, that a timestep $\sim 0.1\,ns$ was required to avoid instability in the computation. Since each step was found to require ~ 2 seconds of CDC 6400 computer time, in order to simulate the times of interest $\sim 10\text{-}100\,\mu s$, $10^4 - 10^6$ steps would be required. In other words a minimum of 3 hours computing time would be consumed, with a strong possibility of corruption of the solution due to numerical diffusion.

The physical reason for this short timestep lies in the characteristic heating time, $\tau = \frac{nkT}{j^2/\sigma}$ which for $n_e \sim 10^{19}\ m^{-3}$, $T_e = 1\,eV$ and $j = 10^6\ A/m$ gives $\tau \sim 1\,ns$. This short time means that the temperature is in steady state for the $100\,ns - 1\,\mu s$ timescales of interest. Thus it is possible to remove the thermal capacity term $\frac{\partial}{\partial t} nkT$, and thereby use a longer timestep. In addition, the convective term $(\underline{v} \cdot \nabla)nkt$ can be neglected for low velocities and long scale-lengths of interest. Thus the differential equations (8.3) for electron energy reduces to a simple algebraic equation:

$$\frac{j^2}{\sigma} - 3nkT\,\frac{m_e}{m_i}\left(\nu_{ei} + \nu_{eN}\right) - nNSE_I - 2.5\,\frac{nk^2T^2}{m_e \nu L^2} = 0$$

which can be solved for T at each time step by an iterative technique.

In this way the timescale for the computation has only to be short enough to follow the density and velocity.

8.7 RESULTS OF THE CALCULATIONS

The limitation on the value of $\omega\tau$ discussed in section 8.5, together with computing time limitations, prevents solutions being obtained over a wide range of either initial plasma conditions or external circuit parameters. The magnetic field, B_x, for the simulation was chosen to be a ramp of constant slope increasing from zero at the anode to a maximum value at the cathode 13.5 cm away. The external circuit was chosen to be $R = 0.2\Omega$, $L = 0$, $C = 200\,\mu F$. The initial neutral density was always taken to be $1.0\times10^{21}\ m^{-3}$ corresponding to a 30 mτ filling pressure of gas. Other parameters such as bank voltage, peak magnetic field, working gas and initial plasma density were varied and are listed in the first few columns of Table 8.1. In all these, a mesh of 100 points was used, with spacing $\Delta = 1.5$ cm.

Run 1, which approximates most closely to the experimental conditions described earlier in this thesis, will now be described in detail. The plasma parameters displayed graphically in two dimensions in Fig.8.4 for a time 5 μs show that an appreciable non-uniformity has developed. In particular there is an azimuthal modulation of density increasing from 16% at the anode to 39% at the cathode, which has a similar shape to the experimental first stage light emission of Fig.2.8. Most of the axial plasma current flows along the density streamer. The Hall current also is a maximum in the spoke so that the total current flow illustrated in Fig.8.5 follows the shape of the spoke. Very little current (~ 10% of maximum) flows in the troughs where $\underline{E}_\varphi \wedge \underline{B}/B^2$ driven currents oppose the resistive current flow. Consequently the temperature peaks on the edge of the density feature where the density is low, but where there is appreciable current. The axial plasma velocity is a maximum here also and for the same reason. The feature moves in the y direction as shown in Fig.8.6 with a velocity which becomes terminal after 1 μs at 50 km/s. This is close

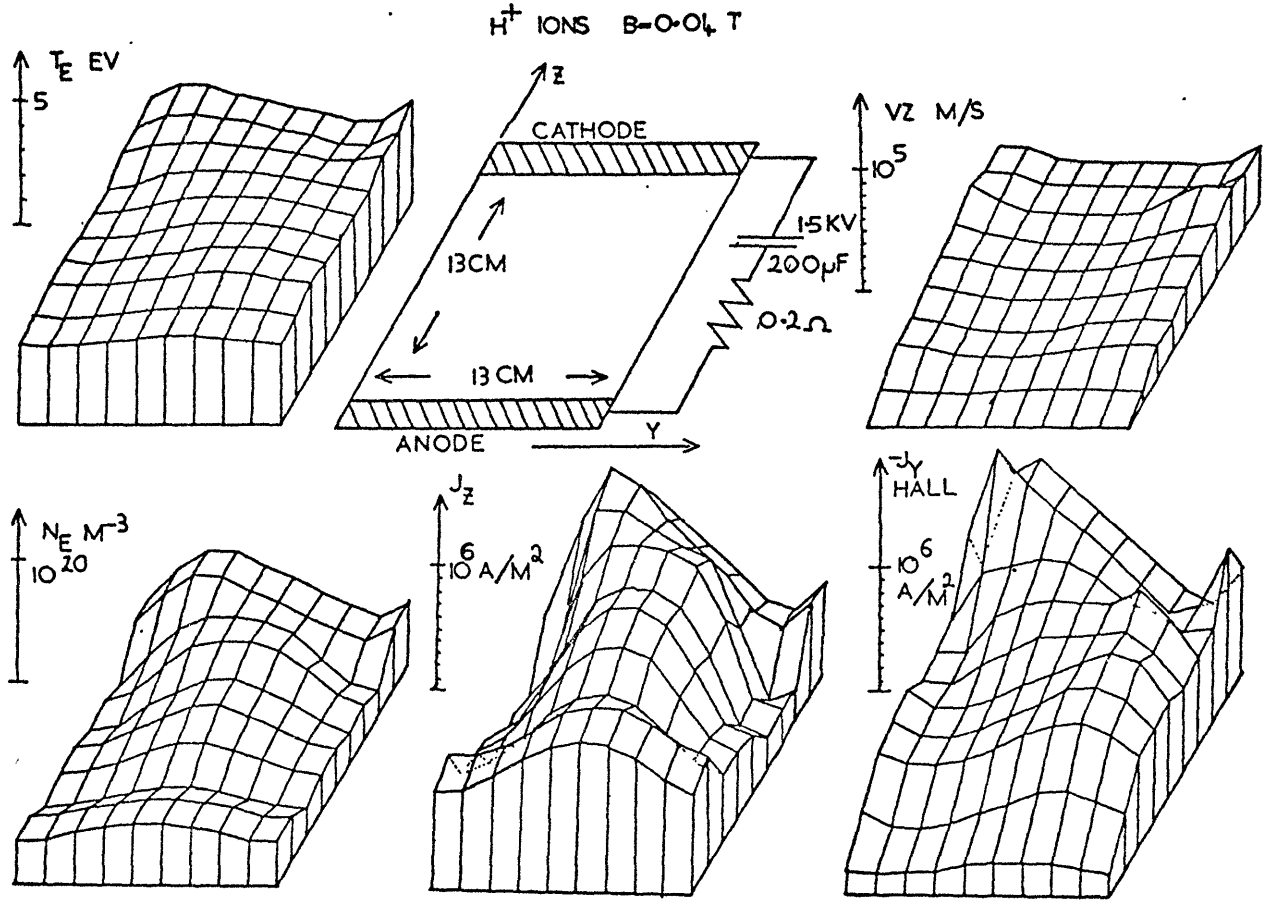

Fig.8.4

Two dimensional display of plasma parameters for run 1 at 5μs showing that a significant non-uniformity has developed. B = 0.04T , H^+ ions. The figures show (clockwise starting top left) T_e, electrode configuration, axial velocity v_z, Hall current j_y, axial current j_z and electron density n_e

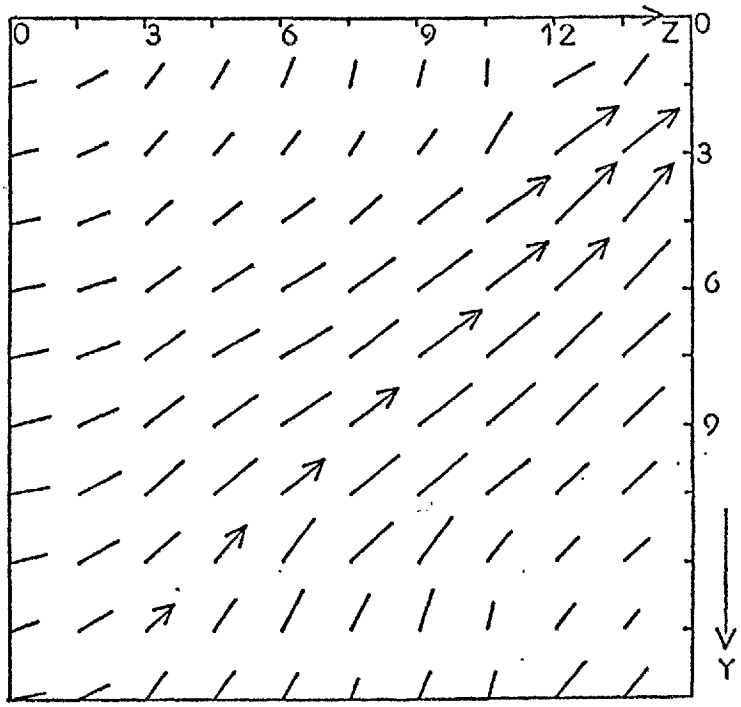

Fig.8.5

Current flow vectors in y-z plane at 5 μs for run 1; showing channelling of current in spoke. The length of lines are proportional to current density

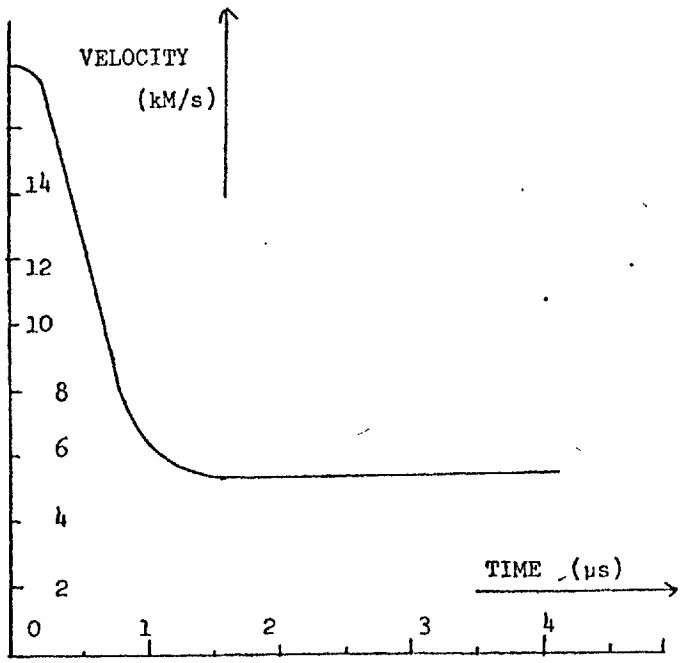

Fig.8.6

The spoke azimuthal velocity as a function of time. Ion mass = 1, B_o = 0.04 T, bank voltage = 1.5 kV

TABLE 8.1

RUNS OF THE 2-D FLUID CODE

Run	Ion Atomic mass No	Ionization Potential	B_o(T)	V_{bank}	R_{scale}	Special Features	Time Simulated	Plateau Voltage	Terminal Spoke Velocity	Maximum Fluctuation Amplitude	Comments
1	1.0	13.6	0.04	1.5 kV	2,5 cm		5.25 μs	740V	5×10^4 m/s	45%	
2	1.0	13.6	0.04	2.0 kV	2.5 cm		2.5 μs	835 V	7.5×10^4 m/s	15.4%	
3	1.5	13.6	0.04	1.5 kV	2.5 cm		2.5 μs	715V	4.5×10^4 m/s	6%	
4	2.0	13.6	0.04	"	"		2.5 μs	702V	3.0×10^4 m/s	2.6%	
5	5.0	13.6	0.04	"	"		2.5 μs		2.3×10^4 m/s	6.6%	Growth → damping
6	2.0	15.4	0.02	1.5 kV	"		2.5 μs	540V	2.5×10^4 m/s	1.3%	Damps after 1 μs
7	2.0	15.4	0.03	1.5 kV	"		2.5 μs	650V	3.6×10^4 m/s	6%	Damps after 1 μs
8	2.0	15.4	0.035	1.5 kV	"		2.5 μs	710V	6.0×10^4 m/s	14%	
9	2.0	15.6	0.04	"	"		1.25 μs	735V	5.0×10^4 m/s	53%	
10	1.0	13.6	0.04	"	"	σ_{CE} = 1/10	250 ns	-	-	4.7%	112 eV ions Convection → high $\omega\tau$
11	"	"	"	"	"	No azimuthal mom^{m} ex.	750 ns	-	-	35%	No terminal effects
12	"	"	"	"	"	No z convection		-	-	3%	Damped
13	"	"	0.04	1.5 kV	0.025 m	No recombination	1.75 μs	555V	2.3×10^4 m/s	5%	Damped
14	"	"	0.04	1.5 kV	0.05 m		3.75 μs	615V	-	2.8%	Damped
15	"	"	0.06	1.5 kV	1 m		2.5 μs	915V	1.2×10^4 m/s	11%	
16	"	"	0.08	1.5 kV	1 m		2.5 μs		-	3%	Damped

H_2^+

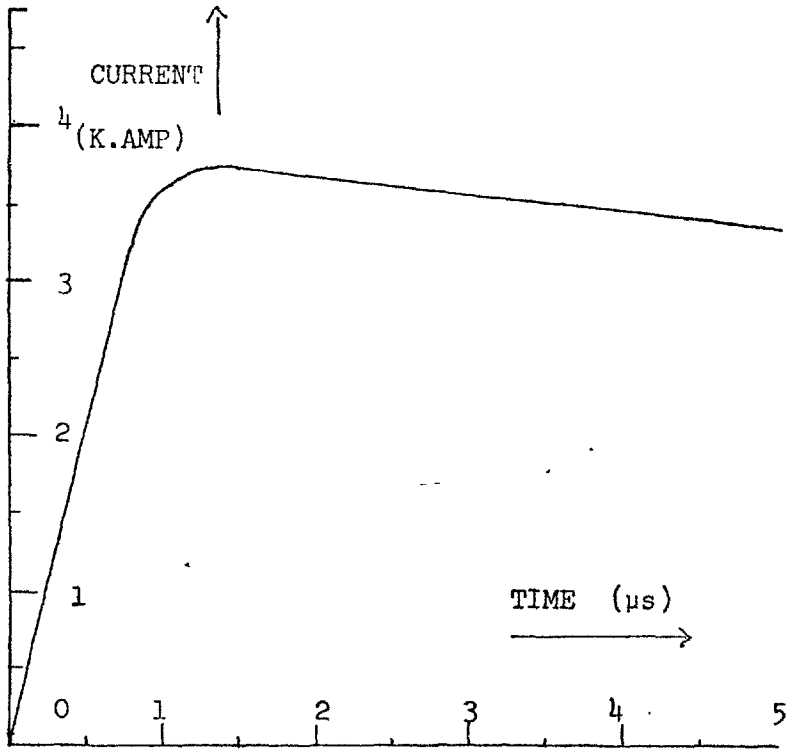

(1)

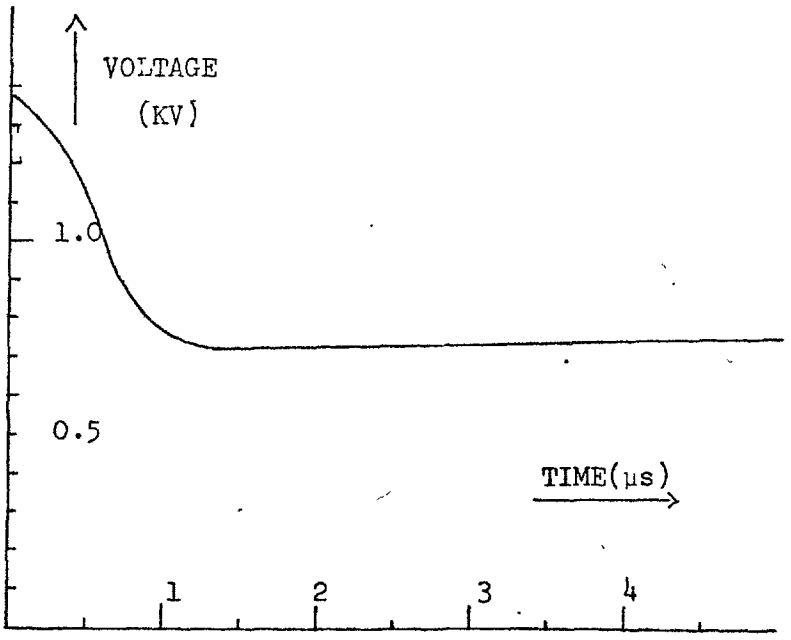

(2)

Fig.8.7

(1) Current and (2) voltage for run 1, showing plateau effect. Ion mass = 1, B_o = 0.04 T, bank voltage = 1.5 kV

to the Alfven critical velocity for ions of mass number 1 and ionization potential 13.6 eV (equation (7.6). This terminal velocity is reached at the same time that current and voltage (Fig.8.7) reach plateau values of 3.7 kA and 740 V. The subsequent time variation in electrode voltage is only ~ few percent despite a large increase in the amplitude of the non-uniformity. This is similar to the experimental observations of Fahelson and Block (Alfven, 1960). However, here the ion Larmor radius in the electric field ~ 7 kV/m is ~ 30 cm, so that acceleration should occur. But, the short charge exchange mean free path keeps ion energies below ~ 20 eV.

The increasing density due to ionization causes $\omega\tau$ to fall, with a corresponding fall in growth rate for the fluctuation. It is not until the amplitude of the fluctuation has become large, giving a high $\omega\tau$ in the troughs, that the growth rate increases again. Figs.8.8(1) and (2) show the time evolution of $\omega\tau$ and the fluctuation amplitude.

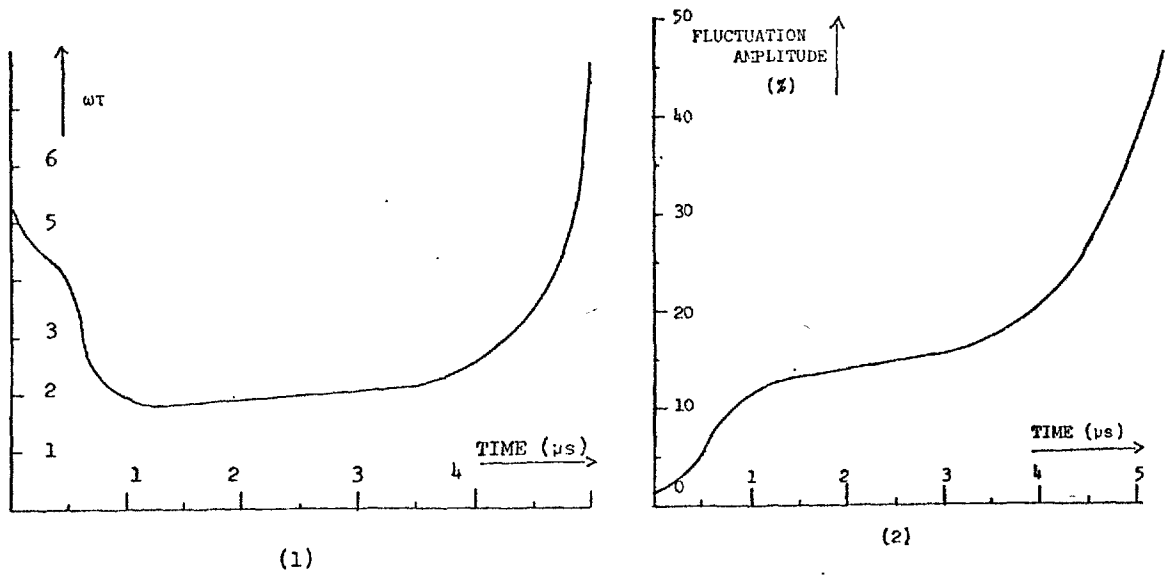

Fig.8.8
The time evolution of (1) $\omega\tau$, and (2) the fluctuation amplitude for run 1. Ion mass = 1, B_o = 0.04 T, bank voltage = 1.5 kV

The other runs summarised in Table 8.1 include various masses and ionization potentials, but the results are qualitatively similar to those already described. The B dependence of the growth in amplitude of fluctuation is illustrated in Fig.8.9, where four types of behaviour are seen. Firstly for low magnetic fields such that initially $\omega\tau \leqslant 2$, an initial perturbation in density is damped within a time $\sim 1\,\mu s$. For slightly higher magnetic fields $\omega\tau \geqslant 2$, there is initially growth in amplitude, but increasing ionization reduces $\omega\tau \leqslant 2$ and the perturbation subsequently decays. For higher magnetic fields there is initial fast growth of non-uniformities with $\omega\tau \geqslant 4$, but ionization reduces $\omega\tau$ to $2 \leqslant \omega\tau \leqslant 4$ and the rate of growth falls dramatically. However if the growth is still sufficiently fast that the density in the troughs continues to fall, when $\omega\tau$ becomes $\geqslant 4$ in these regions the growth becomes rapid once more. For still higher magnetic fields, the growth rate is fast ($\tau_g \sim 1\,\mu s$) without respite until $\omega\tau$ becomes $\geqslant 6$ in the troughs and the potential solver fails to converge. These effects agree with the behaviour of the growth rate (Fig.7.10) predicted by the linear theory described earlier, where a sharp increase in growth is obtained for increasing $\omega\tau$.

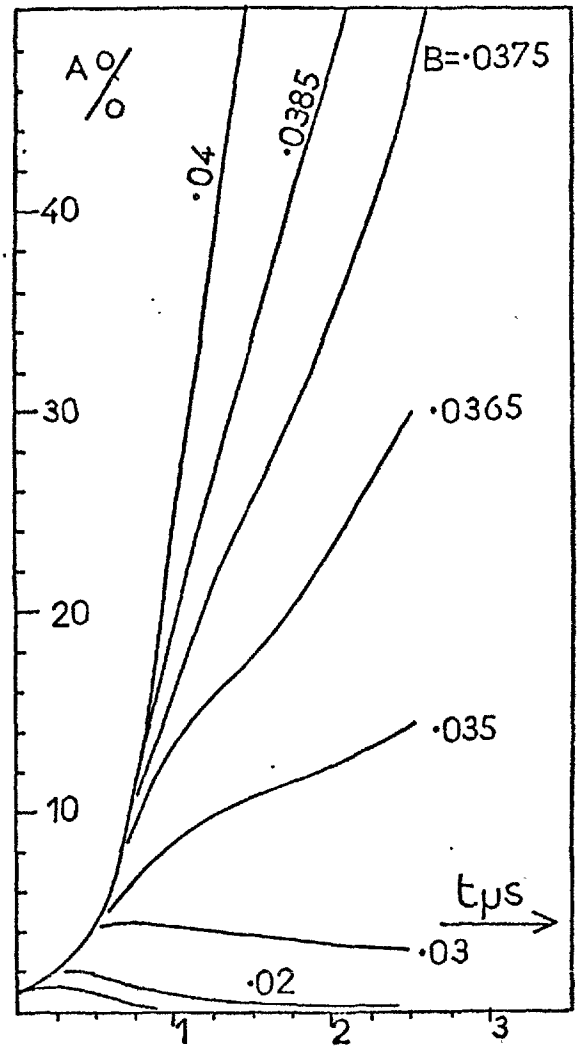

Fig.8.9
Growth of density fluctuation amplitude (A), as a function of time, for various B. H_2^+ ions, $n_e = 10^{19}\ m^{-3}$, $T_e = 2.5\,eV$

8.8 THE LIMITING SPOKE VELOCITY EFFECT

Figure 8.10 shows the dependence of terminal spoke velocity and plateau voltage on magnetic field and ion mass. Although the voltage varies so as to keep the E/B drift velocity constant, the spoke velocity is not independent of B. The mass dependence of velocity is the same as the Alfven limit (7.6), i.e. $\sim 1/\sqrt{m}$.

An examination of the equations solved, show that the Petschek approach (equation (7.7)) is excluded since there is no direct coupling between ion kinetic energy and ionization, and moreover, the ionization term in the electron energy equation is for the conditions of interest, negligible in comparison with the electron thermal conduction loss. The run 11 (Table 8.1) in which azimuthal ion-neutral momentum exchange is removed, shows that ion-neutral friction provides the drag on the spoke. Thus if the energy equation is simply a balance of Ohmic heating and conduction loss, and the momentum equation $j \wedge B$ force balancing friction due to stationary neutrals then we have:

$$j^2/\sigma = 2.5 \frac{ne^2T^2}{m_e \nu L^2}$$

$$m_i n N \sigma_{CE} V^2 = \underline{j} \wedge \underline{B} \qquad \ldots (8.18)$$

where σ_{CE} is the ion-neutral charge exchange cross-section. Substituting $B = \frac{10\,\omega\tau\, ne}{\sigma}$, where the 10 arises for reasons mentioned in section 8.5, and eliminating j gives:

$$V = \left[2.5^{\frac{1}{2}}\ 10\ \omega\tau \frac{\lambda}{L} \frac{eT}{m_i}\right]^{\frac{1}{2}} \qquad \ldots (8.19)$$

where λ/L is the ratio of ion neutral mean free path to thermal conduction scale length. Typically, $\lambda \simeq 3\,mm$, $L = 2.5\,cm$, $\omega\tau$ lies in the region $2 \leqslant \omega\tau \leqslant 4$, and $T_e \sim \frac{1}{3} E_I$. This gives $V \sim \left(\frac{2eE_I}{m_i}\right)^{\frac{1}{2}}$, so that here the Alfven limit (equation (7.6)) arises because of the narrow range of λ, T_e and $\omega\tau$ found in the solutions.

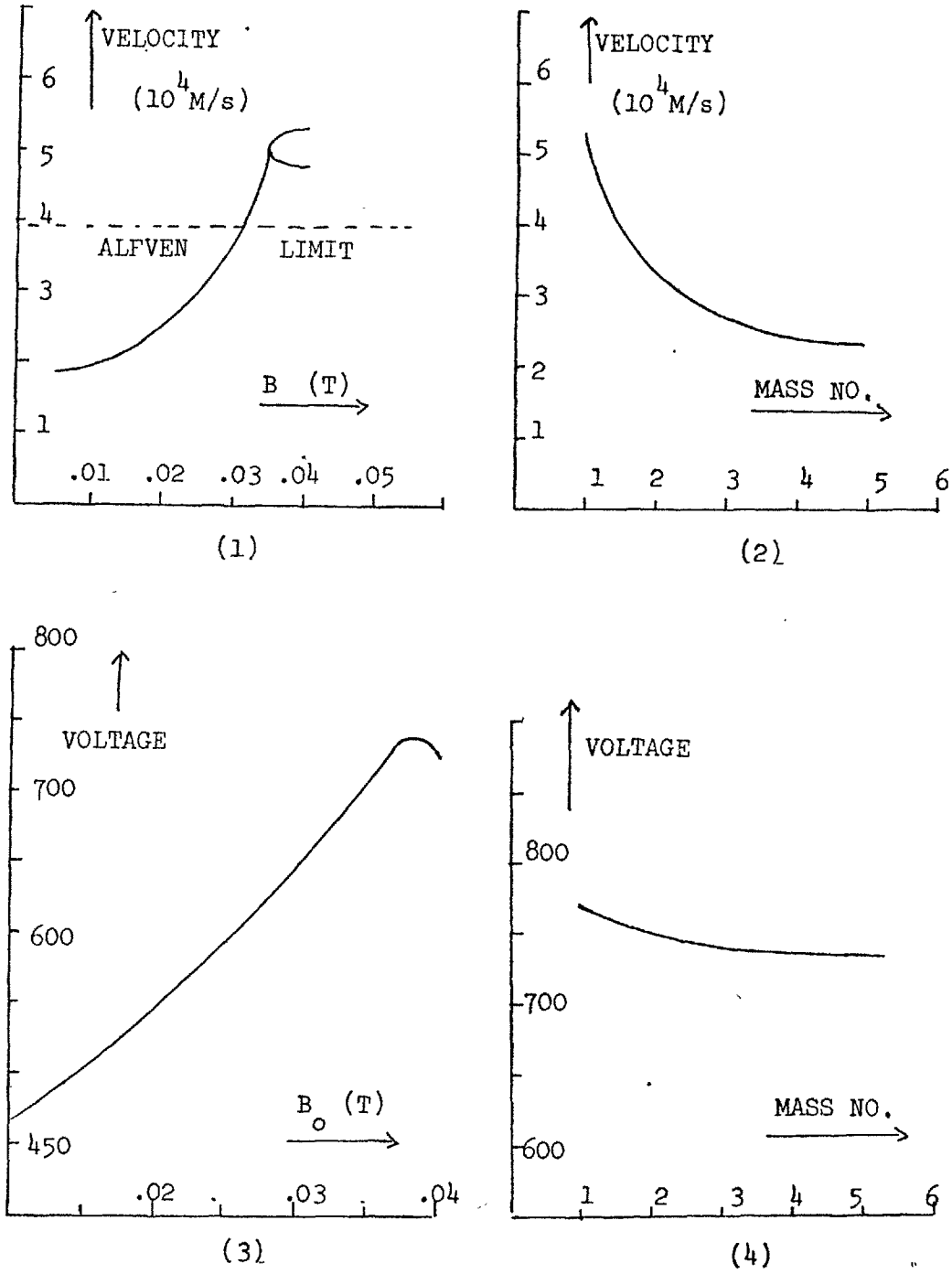

Fig.8.10

(1) Spoke terminal velocity against B_o for mass 2 .
(2) Spoke terminal velocity against mass number for B_o = 0.04 T
(3) Plateau voltage against B_o for mass 2
(4) Plateau voltage against mass number for B_o = 0.04 T

However this is not the whole picture, since Chapter VII predicts an ionization phase velocity relative to the rest frame of the heavy particles. Examination of the results of runs, indeed, shows that the spoke is not purely convected with the heavy particles. This clearly must be the case, since V_y depends upon axial position, whereas the spoke y-velocity is everywhere uniform. Thus equation (8.19) sets the background ion velocity upon which the electron fluid phase velocity effects of Chapter VII are superimposed.

8.9 THE VOLTAGE PLATEAU

It is clear from Fig.8.10(4) that the voltage plateau does not arise, as in the Alfven interpretation, in order that the maximum ion energy, $\frac{2m_i E^2}{B^2}$, should equal the ionization energy, thus giving rise to an enhanced heavy particle collisional ionization. This would give a mass dependence of voltage $V \propto 1/\sqrt{m}$, which is not seen in Fig.8.10(4).

Figure 8.10(3) shows the magnetic field dependence of plateau voltage for H_2^+ ions. Above $B = 350\,G$, the plateau is not well defined, showing that it is not an effect due to non-uniformity. Figs.8.11(1) and (2) show that the plateau is associated with the attainment of an almost uniform steady state, which for low $\omega\tau$ is simply the ionization steady state, $n_e \simeq 0.7 N T_e^{-E_I/T_e}$ or $n_e \sim 4\times10^{19}\ m^{-3}$ for $T_e = 4\,eV$ and $N = 10^{21}\ m^{-3}$. The timescale for arrival at this steady state is $\sim 1/NS$ or $0.6\ \mu s$ which is the ionization time. The impedance is given by the collisional relation, $E_z = [1 + (\omega\tau)^2]J_z/\sigma$ so that the total voltage increases with B, but is independent of m_i as seen in Figs.8.10(3) and (4).

At higher magnetic fields, such that a significant non-uniformity develops, the axial currents associated with the non-uniformity reduce this impedance. This gives rise to the maximum in Fig.8.10(3).

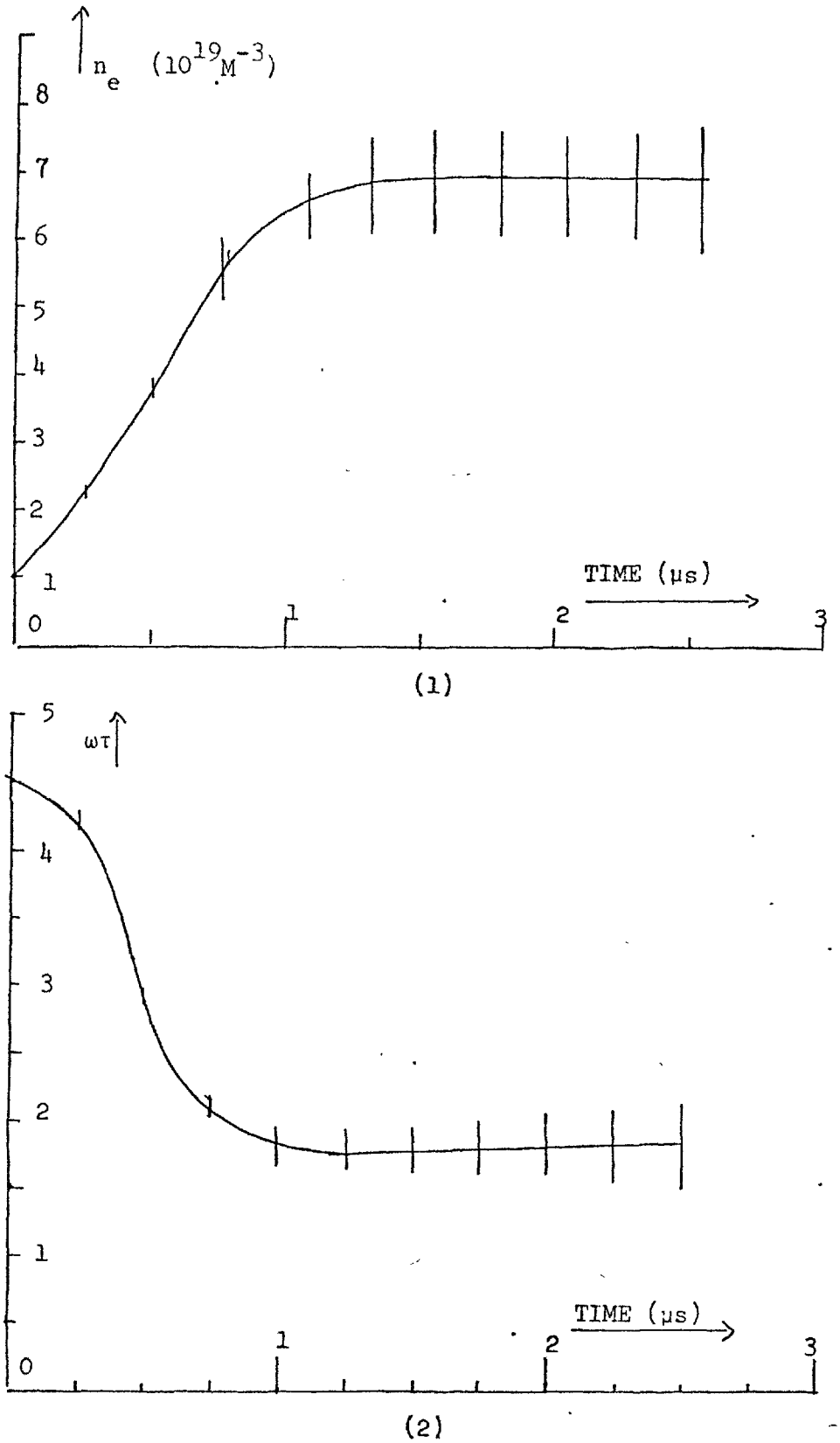

Fig.8.11

(1) The evolution of the density steady state, and
(2) the evolution of $\omega\tau$. The bars show the amplitude of fluctuation. B_o = 0.04 T, ion mass = 2, bank voltage = 1.5 kV

8.10 THE IMPORTANCE OF ION MOTION

The runs considered so far have been appropriate to the early phase of the discharge where the high neutral density gives a short ion mean free path, λ_i. Later in the discharge, after neutral depletion, λ_i increases away from the anode so that significant ion acceleration can occur.

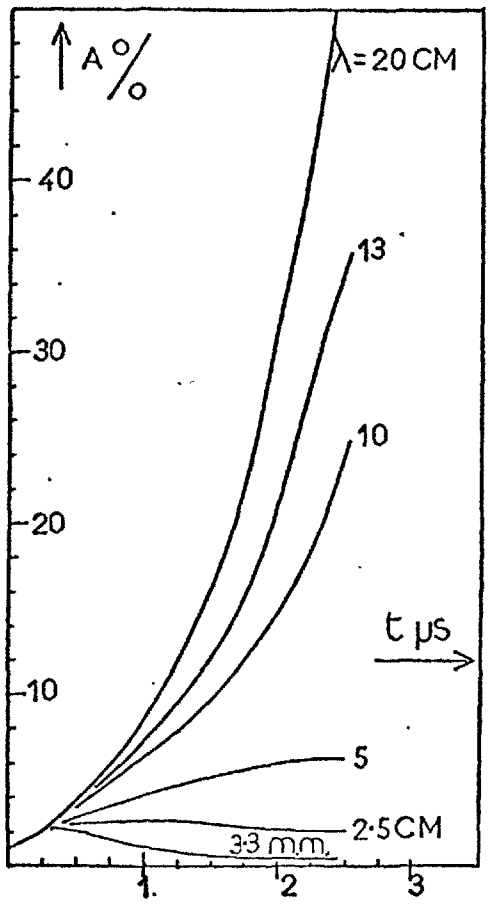

Fig.8.12
The amplitude of density perturbation against time for various ion mean free paths λ. H_2^+ ions, B_o = 0.02 T, bank voltage = 1.5 kV

Figure 8.12 shows that, for the case of B = 200 G in H_2^+, the effect of increasing λ_i is to cause the damped spoke mode to become a growing mode for $\lambda_i \sim$ electrode separation. The ion energies are correspondingly larger for longer λ_i (typically ~ 50 eV for $\lambda_i \sim 10$ cm) so that the ions contribute $\sim \frac{1}{3}$ of the total discharge current. The gradients in ion flux $\nabla n \underline{v}$ ($\sim 2\times10^{25}$ m^{-3} s^{-1} for $n_e = 4\times10^{19}$ m^{-3}, $v_z \simeq 7\times10^4$ m/s and $\nabla \sim 7$ m^{-1}) become comparable to the ionization rate in the low temperature regions ($nNS \sim 2\times10^{25}$ m^{-3} s^{-1} for $n_e \sim 4\times10^{19}$ m^{-3}, $N \simeq 10^{21}$ m^{-3} and $T_e \sim 3$ eV) so that acceleration assists recombination in reducing the electron density in the spoke troughs. The consequent change in $\omega\tau$ causes the plasma to become unstable to spoke formation. Thus, the improved ion acceleration decreases the lower limit on $\underline{B}$ for which spokes may grow.

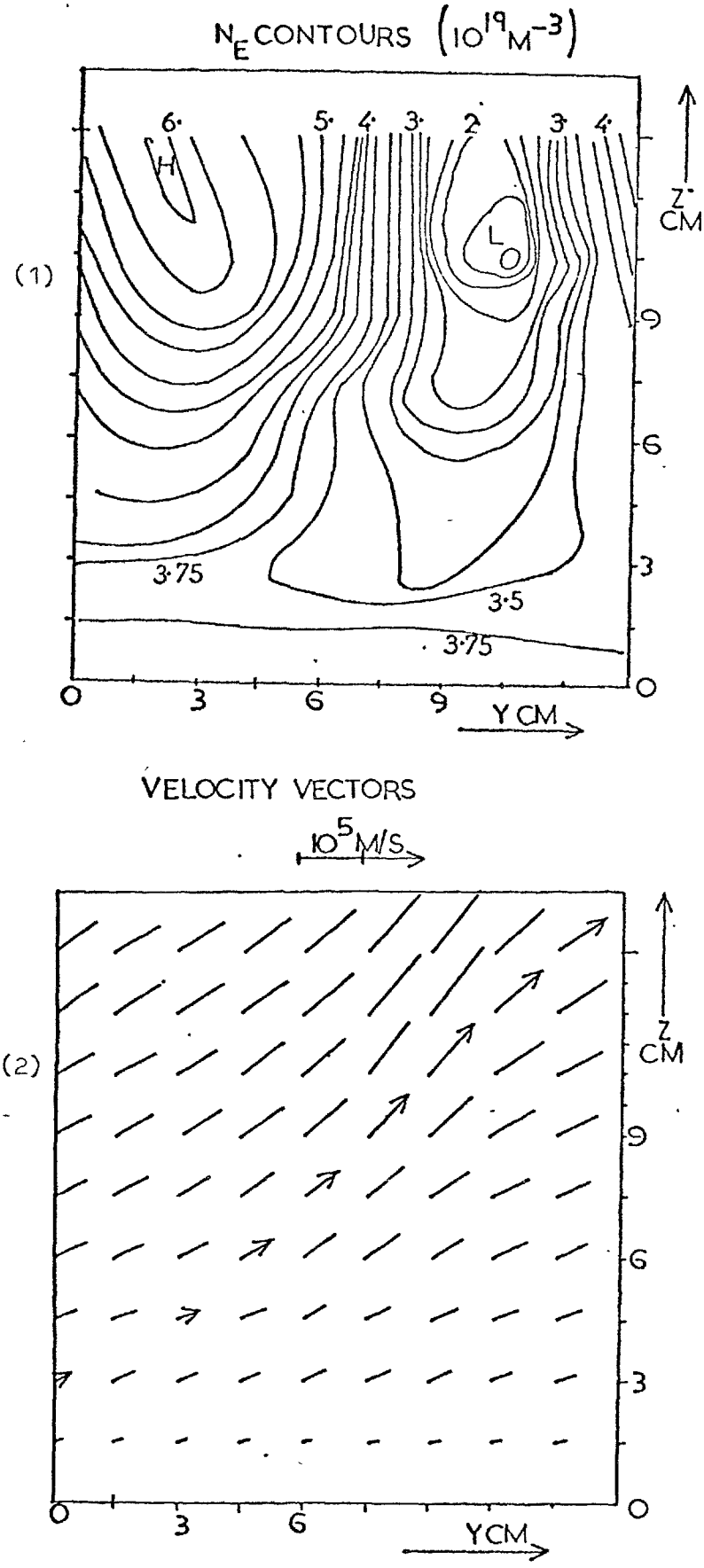

Fig.8.13

(1) Density contours, and (2) ion flow velocity vectors at time 2 μs, for case B = 0.02 T, H_2^+ ions λ_i = 10 cm and bank voltage 1.5 kV

Figures 8.13(1) and (2), which show density contours and ion flow vectors, illustrate this effect of convection out of the troughs. The divergence due to the y motion will be $\sim 26^{\circ}$, which is large considering that the ion Larmor radius ($\rho_{L1} \sim 50\,\text{cm}$ for $E = 10^4\ \text{V/m}$ and $B = 0.02\,\text{T}$) is much longer than the anode-cathode distance (13.5 cm). In fact the large divergence arises because the magnitudes of z and y currents are similar, as a result of the non-uniformity.

Examination of the energy balance reveals, surprisingly, that the low density regions absorb more than a proportionate share of the directed energy input. This is a consequence of the large streaming velocities here. These regions could be important, therefore, when maximising the ion energy output. It is likely, though, that this conclusion will fail in the limit of large fluctuation amplitude where ion energy saturates at the anode cathode voltage. Unfortunately the code will not deal with this regime.

8.11 THE SIGNIFICANCE OF THE 2-D MODEL

The fluid code described in this chapter successfully predicts the formation of axial streamers in the initial phase of the discharge. The physical mechanism is Ohmically driven ionization supported by acceleration effects. The current flow is channelled along the streamer and thus causes significant y-motion of plasma, and so contributes to exhaust divergence. As predicted by the linear theory of Chapter VII, the growth depends strongly upon $\omega\tau$, becoming rapid, $\tau_g \leqslant 1\,\mu\text{s}$, for $\omega\tau \geqslant 3$.

The limiting spoke velocity is predicted by the model and shown to be a combination of heavy particle drag effects and of the ionization wave phase velocity effects of Chapter VII. Though ionization plays the dominant rôle, this is more complex than suggested by the theories of Petschek and others (Sherman, 1973).

CHAPTER IX

CONCLUSIONS

9.1 A REVIEW OF THE NEW RESULTS PRESENTED IN THIS THESIS

This section brings together the new work presented in this thesis to describe the Hall accelerator discharge. The following section treats design considerations for an improved accelerator for fusion applications, in the light of this new work.

The most important advance in the experimental work is the ability to measure spatially resolved plasma and neutral density, essential if the plasma is to be understood. This has not been attempted previously.

The theoretical work extends the linear electrothermal theory, and develops a two-dimensional fluid code which describes the nonlinear large amplitude behaviour of the ionization mode with ion acceleration included.

Together the experimental and theoretical results give the following picture of the discharge.

After breakdown the plasma of molecular ions with a strong neutral background is unstable to ionization waves which grow with wavelength ~ 5 cm in times ~ 250ns . The increased local heating arising from the current flow results in further ionization in the peaks and so the wave rapidly saturates into a streamer in the axial-azimuthal plane. Further growth is limited to that allowed by the slow rise in current from the capacitor bank. The azimuthal electric field associated with this feature drives electrons to the anode by $E_\theta \wedge B_r$ effects in the density peaks. However, no return current flows in the low density regions so this current eventually dominates the collisional electron current. Ion acceleration occurs under the $\underline{j} \wedge \underline{B}_R$ force of the streamer current, but because of the high neutral density and short charge-exchange mean free path for ions, this momentum inputs

the neutrals and begins to sweep them out of the accelerator. However, the oblique nature of the streamer accelerates ions and neutrals azimuthally. The neutrals have a sufficiently long mean path for collisions to impact the wall frequently and so gain little azimuthal velocity, and the resulting drag between ions and neutrals eventually gives a terminal velocity for the ions. However, the streamer moves faster than this in consequence of ionization on the leading edge and recombination on the trailing edge, an effect which is predicted by simple electrothermal theory and the full code. This recombination is dissociative, and the result is a gradual transition from a molecular hydrogen background to an atomic one. However, the electrothermal mode structure in an atomic plasma is shown to be different, in that the ionization wave has a very slow growth rate. In order to carry the still increasing current the spoke sub-divides into ~ 5 smaller streamers, each with associated electric field, probably as a result of the fast heating mode for the atomic system. Simultaneously, the neutral density depletion by charge exchange allows acceleration of ions to higher velocities, and convection of these ions into the second stage produces a feature which moves counter to the azimuthal electron stream there. The reversed $j_z \wedge B_r$ in the second stage is not sufficient to break up the continuity of the spoke through the two stages.

The two effects of charge exchange neutral depletion and dissociative recombination culminate at $100\,\mu s$ in a system which has a dominant atomic composition which drops steeply from anode to cathode and is not able to sustain the spoke feature which disappears.

The switchover to the second discharge phase is abrupt, occurring in ~ 1 spoke azimuthal rotation period, with a corresponding change in character. The impedance rises by a factor ~ 2 to $\sim 1\,\Omega$ over $\sim 50\,\mu s$, and thereafter conditions change only slowly. At these times large ion and neutral velocities appear, indicating ions now traverse a large fraction

of the anode-cathode distance. The electron density and neutral atom densities fall sharply further from the anode: n_e decreases from $\sim 2\times10^{19}$ m^{-3} at the anode, to $\sim10^{18}$ m^{-3} at the cathode, whilst N decreases from $\sim10^{22}$ m^{-3} to $\sim10^{20}$ over this range. The neutral density at the cathode is low because of neutral depletion by charge exchange, and the electron density is low because of Hall acceleration. These low densities give rise to a large collisional value of $\omega\tau$ which should make the acceleration efficient – i.e. give a low fraction of current carried by electrons. In fact the electron conductivity is dominated by a fast ($\sim$5 mc/s), apparently randomly varying, fluctuation characteristic of this phase of the discharge. The E_θ fields associated with this mode give rise to $E_\theta \wedge B_r$ electron drift currents which contribute $\frac{2}{3}$ of the $\sim$1 kA discharge current. The remaining $\frac{1}{3}$ is carried by ions.

Although the electrothermal theory suggests that the atomic plasma is unstable to heating waves, this does not satisfactorily explain the fluctuations. These are large amplitude, and therefore nonlinear, and in addition, the fast period is comparable to ion transit times in the accelerator, and so ion motion should be included in any theory.

Unlike low current density Russian devices, the two stages of the device here are dissimilar. In particular, the ion current lies on a 100 amp plateau in the first stage, so that most of the ion flux build-up occurs in the second stage. Large ion energies are seen only in the second stage where the Hall current is large. There are two reasons for these differences, the location of the ionization regions and ion trajectory effects.

The ionization is strong at the anode because of the high electron and neutral density there, but rapidly decreases with n_e and N further into the first stage. The low electron density in the second stage gives

an increase in temperature, since neutral collisions and flux limited heat loss become more important. This increase in T_e gives a peak in atomic ionization in the first half of the second stage. Thus ions are created predominantly in these regions, so that increase in ion-current with distance is limited to these regions.

The low electric fields permitted by the fluctuation dominated electron conduction give ion Larmor radii ~ few cm which are much smaller than the anode-cathode distance. The consequent azimuthal motion of ions gives rise to centrifugal divergence. E_r fields associated with particular magnetic field configurations produce significant radial motion, particularly for newly created, low energy, ions. These lead to serious wall impact inside the accelerator, and the Hall momentum input is lost to the walls. Only ions created in the second stage can escape through the cathode aperture, but these are strongly divergent because their azimuthal velocity has not been reduced to zero. This divergence will be worsened by the azimuthal electric fields associated with the fluctuations.

At ~600 μs, the pulsed hydrogen gas supply begins to fall off, but the wall impact already mentioned and anode local melting, begin to release impurities into the discharge. The discharge becomes less instability dominated, but more non-reproducible. 400 amps of ion current is carried at these times, but the ion species are unknown.

9.2 AN IMPROVED DESIGN OF HALL ACCELERATOR

In view of the future requirements on ion sources, an improved Hall accelerator is worthy of consideration if the good scaling of the ideal accelerator can be achieved without sacrificing the simplicity of existing devices. The work already presented suggests the following requirements which must be taken into account in any new design :

1. Well collimated ion trajectories
2. Well defined ionization region
3. No wall or electrode damage
4. Good plasma uniformity
5. High T_e to avoid streaming and ionization modes
6. Low N to avoid electrothermal modes
7. Controlled $\omega\tau$
8. Short well defined stages
9. No unwanted defocusing E_r fields.

Fortunately these are not all independent. For example, elimination of the electrothermal non-uniformities would increase the plasma impedance to the collisional value, and the increased electric fields would assist the achievement of requirements 1 and 3. Requirements 2 and 4 on ionization and uniformity are crucial, and without improvement here the behaviour is likely to be similar to the device described in this thesis. It is suggested that a secondary, thermionically emitting cathode type discharge in the first stage might satisfy the former requirement, and if efficient, the neutral density could be lower in the remaining stages, so as to eliminate ionization modes. An increased ion flux would assist in removing the unwanted neutrals by charge exchange. A magnetic field with a confining configuration would permit the higher temperature required to avoid the streaming instability, and blunt the sensitive T_e dependence of ionization which gives ionization instability. The control of $\omega\tau$ is less straightforward, and except for high fluxes of low energy ions, $\omega\tau$ is likely to be large, with the consequent risk of instability. The addition of high z material might be one answer, but, for injection purposes, this is undesirable. The cusp geometry has a region of low $\omega\tau$ close to the axis, which might be useful in controlling the voltage, but it is not clear whether the associated resistive sheath effect (Kilkenny, 1973) is desirable. The multiple cusp geometry has the advantage of a built-in ion focusing mechanism in the axial field, and the possibility of using very many short stages.

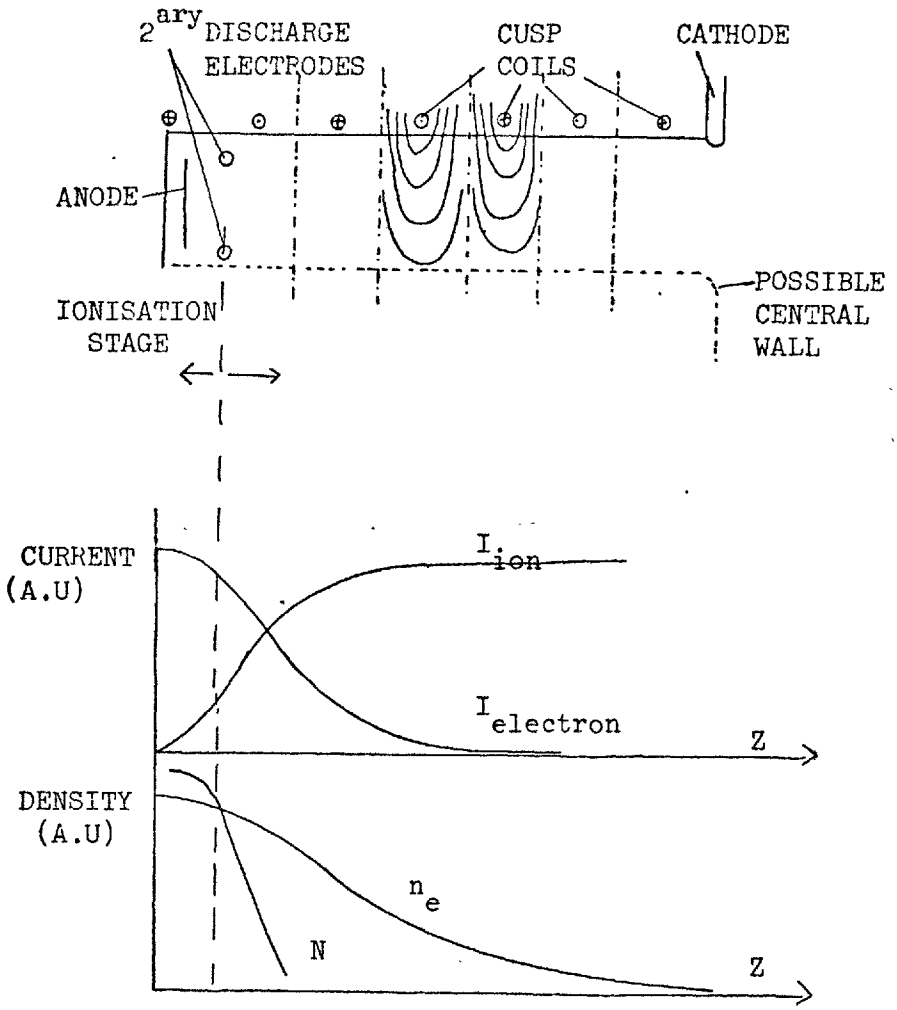

Fig.9.1

A simple scheme for testing the feasibility of localising the ionization close to the anode by means of a thermionically controlled secondary discharge. Also shown are sketches of currents and densities which might be obtained

Although the idea of a pre-ionization stage could be tested on an existing accelerator, the problem of defocusing due to E_r fields is likely to obscure any benefits. It would be an interesting experiment to investigate the effect of pre-ionization on $\omega\tau$ in the system illustrated in Fig.9.1, and to study whether reduction in impedance by non-uniformities is an inevitable consequence of acceleration at high $\omega\tau$. Also shown in Fig.9.1 are profiles of current and plasma and neutral densities that might hopefully be achieved.

The pre-ionization should allow the ion flux to build up rapidly at high ion density and low energy, to give an almost fully ionized plasma in following stages. The electric field required to drive the small electron current in these stages would accelerate the ions to the energies required.

Such is the ideal, but it remains to be seen if this is attainable in practice. The efficient acceleration of high $\omega\tau$ fully ionized plasmas is a whole new field.

REFERENCES

ABRAMOV, V.A., ZUBKOV, I.P., KISLOV, A.Ya., Sov. Phys.-Tech. Phys., 18, 1609 (1974).

ALFVEN, H., Rev. Mod. Phys., 32, 710 (1960) also 'On the Origin of the Solar System', (1954).

ALDCROFT, D. et al., Nuclear Fusion, 13, 393 (1973).

ARTSIMOVICH, L.A., Nuclear Fusion, 12, 215 (1972).

ARTSIMOVICH, L.A., et al., Proc. 3rd Int. Conf., Novosibirsk, 1968 (IAEA vol.I, p.17 (1969)).

BATES, D.R., KINGSTON, A.E., McWHIRTER, R.W.P., Proc. Roy. Soc., A 267, 155 (1962).

BUNEMAN, O., Plasma Physics, 4, 111 (1962).

BURLOCK, J. BROOKS, D.R., App. Phys. Lett., 7, 49 (1965).

CHAQUI, H., Imperial College internal report, (1974).

COLE, H.C., Proc. III European Fusion Conference, Utrecht, (1969).

COLE, H.C., Ph.D. Thesis, London University, (1970a)

COLE, H.C., Nuclear Fusion, 10, 271 (1970b).

COLE, H.C. et al., 7th Symposium Fusion Technology - Grenoble, (1972).

COLE, H.C., Unpublished results and Berkely Conference Report (1974).

CORDEY, J.G.,et al., Nuclear Fusion, 15, 441 (1975).

DANGOR, A. et al., IAEA Vienna, 1969, vol.I, p.255, (1969).

DUNNET, R.M., Ph.D. Thesis, London University, (1968).

ESIPCHUK, Yu.B., MOROZOV, A.I., Sov. Phys. - Tech. Phys., 18, 928 (1974).

ETHERINGTON, R.J., HAINES, M.G., Phys. Rev. Lett., 14, 1019 (1965)

FURTH, H.P., Nuclear Fusion, 15, 487 (1975).

GRIEM, H.R., Plasma Spectroscopy - McGraw-Hill, (1964)

HAINES, M.G., Salzburg Fusion Conference, (1961).

HAINES, M.G., J. Plasma Physics, 12, 1 (1974).

HAINES, M.G., McNAB, I.R., Physics in Technology, 5, 278 (1974).

HESS, R., et al., VI Ionization Phenomena in Gases, Paris, (1963).

HINNOV, E., HIRSCHBERG, J.G., Phys. Rev., 125, 795 (1962).

JANES, G.S., LOWDER, R.S., Phys. Fluids, 9, 115 (1966).

JOHNSON, L.C., HINNOV, E., J. Quant. Spectrosc. Radiat. Transfer, 13, 333 (1973)

KILKENNY, J.D., Ph.D. Thesis, London University, (1972).

KILKENNY, J.D., DANGOR, A.E., HAINES, M.G., Plasma Physics, 15, 1197 (1973).

KUSNETSOV, E.I., Review Proc. 7th European Fusion Conference, (1975).

LAWSON, J.D., Proc. Phys. Soc., B 70, (6) (1957).

LARY, E.C., MEYERAND, R.G., SALZ, F., VI Ionization Phenomena in Gases, Paris (1963).

LEHNERT, B., Nuclear Fusion, 11, 485 (1971).

LOCHTE-HOLTGREVEN (eds.), 'Plasma Diagnostics', North Holland (1968).

LOMAS, P.J., KILKENNY, J.D., Proc. 1st I O P Annual Plasma Conference, Bangor (1974).

LOMAS, P.J., KILKENNY, J.D., Proc. VII European Fusion Conf., Lausanne (1975).

MASSEY, H.S.W., BURHOP, E.H.S., GILBODY, H.B., Electronic and Ionic Impact Phenomena, Oxford (1951).

MOROZOV, A.I., KISLOV, Ya., ZUBKOV, I.P., ZhETF Pis'ma, 7, 224 (1968).

MOROZOV, A.I., et al., Sov. Phys. Tech. Phys., 17, 38 (1972a).

MOROZOV, A.I., et al., Sov. Phys. Tech. Phys., 17, 482 (1972b).

MOROZOV, A.I., NEVROVSKII, V.A., SMIRNOV, V.A. Sov. Phys. Tech. Phys., 18, 339 (1973a).

MOROZOV, A.I., NEVROVSKII, V.A. SMIRNOV, V.A., Sov. Phys. Tech. Phys., 18, 344 (1973b).

MOROZOV, A.I., et al., Sov. Phys. Tech. Phys., 18, 615 (1973c).

McWHIRTER, R.W.P., HEARN, A.G., Proc. Phys. Soc., 82, 641 (1963).

NELSON, A.H., HAINES, M.G., Plasma Phys., 11, 811 (1969).

NELSON, A.H., Ph.D. Thesis London University, (1969).

POTTER, D.E., Computational Physics, John Wiley, (1972).

ROSA, R.J., Phys. Fluids, 5, 1081 (1962).

SHERMAN, J.C., Astrophysics and Space Science, 24, 487 (1973).

SPITZER, L., Physics of Fully Ionized Gases, Wiley, (1955)

STIX, T.H., Plasma Physics, 14, 367 (1972).

SWEETMAN, D.R. et al., IAEA Paper No. CN 28/K-5, Madison, (1971).

TFR Group, Proc. 7th European Fusion Conference, Lausanne, (1975).

UNCLES, R.J., Ph.D. Thesis, London University, (1972).

WATKINS, M.L. et al., IAEA Paper No. CN 28-D-9, Madison, 1972).

ZUBKOV, I.P., KISLOV, A.Ya., MOROZOV, A.I., Sov. Phys.-Tech. Phys., 15, 1796 (1971a).

ZUBKOV, I.P. et al., Sov. Phys. - Tech. Phys., 16, 409 (1971b).

ZUBKOV, I.P. et al., Sov. Phys. - Tech. Phys., 16, 695 (1971c).

ZUBKOV, I.P., KISLOV, A.Ya., Sov. Phys. - Tech. Phys., 17, 712 (1972).